Fizika Nizkikh Temperatur, 2001, v. 27, No. 6, p. 579–626

Magneto-optical spectroscopy of magnetic multilayers: Theory and experiment

(Review Article)

V. N. Antonov*, L. Uba, and S. Uba

Institute of Experimental Physics, University of Bialystok, Lipowa 41, PL-15-424 Bialystok, Poland
E-mail: anton@imp.kiev.ua

A. N. Yaresko and A. Ya. Perlov

Max-Planck-Institut for the Physics of Complex Systems, D-01187 Dresden, Germany

V. V. Nemoshkalenko

Institute of Metal Physics, 36 Vernadskii Str., 252142 Kiev, Ukraine

Received December 8, 2000, revised February 3, 2001

Experimental and theoretical results on the optical and magneto-optical (MO) spectral properties of a series of Co/Cu, Co/Pd, Co/Pt and Fe/Au multilayers (MLS) are reviewed. Diagonal and off-diagonal components of the optical conductivity tensor have been determined in the photon energy range 0.8–5.5 eV from the polar and longitudinal Kerr rotation as well as ellipticity and the ellipsometry measurements. The conductivity tensor has been evaluated on the basis of self-consistent spin-polarized relativistic linear muffin-tin orbital (LMTO) band-structure calculations within the local spin-density approximation. The role of the spin polarization and the spin–orbit interaction in the formation of the magneto-optical Kerr effect (MOKE) spectra as inferred from first-principles calculations is examined and discussed. The high sensitivity of the MO properties to the interface structure is studied by *ab initio* modeling of the effects of the interface alloying, substitutional disorder, and the roughness at the interfaces. It is shown that the MOKE spectra of the MLS calculated using the LMTO method reproduce the experimental spectra only moderately well if ideal multilayer structure with sharp interfaces are assumed. It is shown that the MOKE spectra of the MLS can be adequately reproduced only by taking into account their real interface microstructure. The magneto-optical anisotropy (MOA) is studied both experimentally and theoretically for a series of Fe_n/Au_n superlattices prepared by molecular beam epitaxy with $n = 1, 2, 3$ of Fe and Au atomic planes of (001) orientation. The results of the LMTO calculations show that the microscopic origin of the large MOA is the interplay of the strong spin–orbit coupling on Au sites and the large exchange splitting on Fe sites via Au d–Fe d hybridization of the electronic states at the interfaces. The orientation anisotropy of the d orbital moment is calculated from first principles and analyzed on the basis of d orbital symmetry considerations. The relationship between the orbital moment anisotropy and the MOA is discussed. The reviewed results imply that the magneto-optical properties of multilayers with various compositions and structures can be quantitatively predicted from first-principles band-structure calculations. Such a possibility is important for basic research as well aplications.

PACS: 78.20.Ls, 75.70.Cn, **78.66.–w**, 73.20.Dx

Contents

---

* Permanent address: Institute of Metal Physics, 36 Vernadskii Str., 252142 Kiev, Ukraine

1. Introduction

It was first discovered in 1845 by Faraday [1] that the polarization vector of linearly polarized light is rotated upon transmission through a sample that is exposed to a magnetic field parallel to the propagation direction of the light. About 30 years later, Kerr [2] observed that when linearly polarized light is reflected from a magnetic solid, its plane of polarization also becomes rotated by a small angle with respect to that of the incident light. This discovery has become known as the magneto-optical (MO) Kerr effect. Since then, many other magneto-optical effects, e.g., the Zeeman, Voigt, and Cotton–Mouton effects [3], have been found. These effects all have in common that they are due to a different interaction of left and right circularly polarized light with a magnetic solid. The Kerr effect has now been known for more than a century, but it is only in recent times that it has become the subject of intensive investigations. The reason for this recent development is twofold: first, the Kerr effect gained considerable in interest due to modern data storage technology, because it can be used to «read» suitably stored magnetic information in an optical manner [4], and second, the Kerr effect has rapidly developed into an appealing spectroscopic tool in materials research. The technological research on the Kerr effect was initially motivated by the search for good magneto-optical materials that could be used as information storage media. In the course of this research, the Kerr spectra of many ferromagnetic materials were investigated. Over the years the Kerr spectra of many ferromagnetic materials have been investigated. An overview of the experimental data collected on the Kerr effect can be found in the review articles by Buschow [5], Reim and Schoenes [6], Schoenes [7], Ebert [8], and Antonov et al. [9].

The quantum mechanical understanding of the Kerr effect began as early as 1932 when Hulme [10] proposed that the Kerr effect could be attributed to spin–orbit (SO) coupling (see also Kittel [11]). The symmetry between left and right circularly polarized light is broken due to the SO coupling in a magnetic solid. This leads to different refractive indices for the two kinds of circularly polarized light, so that linearly polarized incident light is reflected with elliptical polarization, and the major elliptical axis is rotated by the so-called Kerr angle from the original axis of linear polarization. The first systematic study of the frequency-dependent Kerr and Faraday effects was developed by Argyres [12], and later Cooper presented a more general theory using some simplifying assumptions [13]. The very powerful linear response techniques of Kubo [14] gave general formulas for the conductivity tensor which are now widely used. A general theory of the frequency-dependent conductivity of ferromagnetic (FM) metals over a wide range of frequencies and temperatures was developed in 1968 by Kondorsky and Vediaev [15].

The first *ab initio* calculation of MO properties was made by Callaway and co-workers in the middle of the 1970s [16]. They calculated the absorption parts of the conductivity tensor elements σ_{xx} and σ_{xy} for pure Fe and Ni in rather good agreement with experiment. After these pioneering studies, there was a lull in MO calculations until MO effects were found to be important for magnetic recording and the computational resources had advanced. Different reliable numerical schemes for the calculation of optical matrix elements and the integration over the Brillouin zone have been implemented, giving essentially identical results [17]. Prototype studies have been performed using modern methods of band theory for Fe, Co, and Ni. Following the calculations for the elemental 3*d* ferromagnets, a number of groups have evaluated the MO spectra for more interesting compounds (see Refs. 8, 9, and references therein).

In recent years, artificial layered structures composed of magnetic transition metals separated by nonmagnetic metals have been studied intensively due to the fundamental research interest in these systems and also because of their potential for applications. Oscillatory interlayer exchange coupling [18], giant magnetoresistance [19], and the induced magnetic polarization effect in nonmagnetic layers (see, e.g. Ref. 20 and references therein) have become the most discussed phenomena in layered magnetic structures.

In particular, Co/Pt and Co/Pd multilayered structures (MLS) have attracted a lot of attention because these systems exhibit simultaneously a large magneto-optical Kerr rotation [21,22] and perpendicular anisotropy [23], which in combination make these materials applicable for a new generation of storage devices [24].

The aim of this paper is a review of recent achievements in both the experimental and theoretical investigations of the electronic structure, optical, and MO properties of transition-metal multilayered structures. We considered the most important from scientific and technological points of views: Co/Pt, Co/Pd, Co/Cu, and Fe/Au MLS. In these MLS, the nonmagnetic sites (Pt, Pd, Cu, and Au) exhibit induced magnetic moment due to the hybridization with the transition-metal spin-polarized 3*d* states. The polarization is strong at Pt and Pd sites and weak at noble-metal sites due to completely occupied *d* bands in the later case. Also of interest is how the spin–orbit interaction of nonmagnetic metal (increasing in the sequence Cu, Pd, Pt, and Au) influences the MO response of the MLS. From the standpoint of applications a very important question is how the imperfection at the interface affects the physical properties of layered structures, including the MO properties.

The paper is organized as follows. In Sec. 2.1 the theoretical background of the *ab initio* calculations of the band structure and the optical conductivity tensor are reviewed. The experimental details are described in Sec. 2.2. Sections 3, 4, and 5 present the experimental and theoretical results for the MO properties of Co/Pd, Co/Pt, and Co/Cu MLS, respectively. Section 6 is devoted to the electronic structure and anisotropy of the MO properties in Fe/Au MLS. Finally, the results are summarized in Sec. 7.

2. Experimental and computational details

2.1. Computational details

Phenomenologically, magneto-optical effects at optical frequencies are treated by means of a dielectric tensor. For the polar Kerr magnetization geometry and a crystal of at least threefold rotational symmetry, where both the symmetry axis and the magnetization direction are perpendicular to the sample surface and the *z* axis is chosen to be parallel to them, the dielectric tensor is composed of the diagonal components ε_{xx} and ε_{zz} and the off-diagonal component ε_{xy} in the form

$$\varepsilon = \begin{pmatrix} \varepsilon_{xx} & \varepsilon_{xy} & 0 \\ -\varepsilon_{xy} & \varepsilon_{xx} & 0 \\ 0 & 0 & \varepsilon_{zz} \end{pmatrix} . \qquad (1)$$

At normal light incidence the relation between the complex polar Kerr angle and the dielectric tensor components is given by [6]

$$\theta^{PK} + i\eta^{PK} = \frac{-\varepsilon_{xy}}{(\varepsilon_{xx} - 1)\sqrt{\varepsilon_{xx}}} , \qquad (2)$$

where θ^{PK} and η^{PK} are the polar Kerr rotation and the ellipticity, respectively.

Here and henceforth, the following definitions have been adopted. We choose the time dependence of the electric field as $e^{-i\omega t}$. Hence, all the complex quantities are expressed by their real and imaginary parts as follows: $\varepsilon_{\alpha\beta} = \varepsilon^{(1)}_{\alpha\beta} + i\varepsilon^{(2)}_{\alpha\beta}$, where α, $\beta \equiv x, y, z$, $\varepsilon_{xx} = (n + ik)^2$, and n and k are refractive index and extinction coefficient, respectively. The optical conductivity tensor $\sigma_{\alpha\beta} = \sigma^{(1)}_{\alpha\beta} + i\sigma^{(2)}_{\alpha\beta}$ is related to the dielectric tensor $\varepsilon_{\alpha\beta}$ through the equation

$$\varepsilon_{\alpha\beta}(\omega) = \delta_{\alpha\beta} + \frac{4\pi i}{\omega} \sigma_{\alpha\beta}(\omega) . \qquad (3)$$

For the longitudinal Kerr magnetization geometry, where the magnetization lies in the sample plane and the *y* axis is chosen to be parallel to both the direction of the magnetization and the plane of incidence, the dielectric tensor takes the form

$$\varepsilon = \begin{pmatrix} \varepsilon_{xx} & 0 & -\varepsilon_{xz} \\ 0 & \varepsilon_{xx} & 0 \\ \varepsilon_{xz} & 0 & \varepsilon_{zz} \end{pmatrix} . \qquad (4)$$

The formula for the complex longitudinal Kerr angle as it has been derived from general formulas for the Kerr effect with arbitrary dielectric tensor [25] is given by

$$\theta^{LK}_{s,p} + i\eta^{LK}_{s,p} = -\frac{2\varepsilon_{xz}\sin\varphi\cos\varphi\sqrt{\varepsilon_{xx}}}{D} \tag{5}$$

with

$$D = \left(\sqrt{\varepsilon_{xx}(\varepsilon_{zz} - \sin^2\varphi)} + \sqrt{\varepsilon_{zz}(\varepsilon_{xx} - \sin^2\varphi)}\right) \times$$
$$\times \left(\sqrt{\varepsilon_{xx} - \sin^2\varphi} \pm \cos\varphi\right) \times$$
$$\times \left(\sqrt{\varepsilon_{xx}\,\varepsilon_{zz}}\cos\varphi \mp \sqrt{\varepsilon_{zz} - \sin^2\varphi}\right),$$

where φ is the angle of incidence of the light, and the upper and lower signs correspond to light of p and s polarizations, parallel and perpendicular to the plane of incidence, respectively.

In the case when the assumption $\varepsilon_{zz} \approx \varepsilon_{xx}$ is justified the formula (5) simplifies to [26]

$$\theta^{LK}_{s,p} + i\eta^{LK}_{s,p} = -\frac{\varepsilon_{xz}\sin\varphi\left(\sqrt{\varepsilon_{xx} - \sin^2\varphi} \pm \sin\varphi\tan\varphi\right)}{(\varepsilon_{xx} - 1)(\varepsilon_{xx} - \tan^2\varphi)\sqrt{\varepsilon_{xx} - \sin^2\varphi}}. \tag{6}$$

Using straightforward symmetry considerations it can be shown that all MO phenomena are caused by the symmetry reduction, in comparison to the paramagnetic state, caused by magnetic ordering [27]. Concerning optical properties this symmetry reduction has consequences only when the SO coupling is also taken into consideration. To calculate MO properties one therefore has to take into account the magnetism and SO coupling at the same time when dealing with the electronic structure of the material considered. In the corresponding band structure calculations it is normally sufficient to treat the SO coupling in a perturbative way. A more rigorous scheme, however, is obtained by starting from the Dirac equation set up in the framework of relativistic spin density functional theory [28]:

$$[c\boldsymbol{\alpha}\cdot\mathbf{p} + \beta mc^2 + \boldsymbol{I}V + V_{sp}\beta\sigma_z]\,\psi_{n\mathbf{k}} = \epsilon_{n\mathbf{k}}\,\psi_{n\mathbf{k}} \tag{7}$$

with $V_{sp}(\mathbf{r})$ being the spin-polarized part of the exchange-correlation potential corresponding to the z quantization axis. All other parts of the potential are contained in $V(\mathbf{r})$. The 4×4 matrices $\boldsymbol{\alpha}$, $\boldsymbol{\beta}$, and $\boldsymbol{I}$ are defined by

$$\boldsymbol{\alpha} = \begin{pmatrix} 0 & \boldsymbol{\sigma} \\ \boldsymbol{\sigma} & 0 \end{pmatrix}, \quad \beta = \begin{pmatrix} \mathbf{1} & 0 \\ 0 & -\mathbf{1} \end{pmatrix}, \quad \boldsymbol{I} = \begin{pmatrix} \mathbf{1} & 0 \\ 0 & \mathbf{1} \end{pmatrix}, \tag{8}$$

where $\boldsymbol{\sigma}$ are the standard Pauli matrices, and $\mathbf{1}$ is the 2×2 unit matrix.

There are quite a few band structure methods available now that are based on the above Dirac equation [29]. In one of the schemes the basis functions are derived from the proper solution of the Dirac equation for the spin-dependent single-site potentials [30,31]. In another approach, the basis functions are obtained initially by solving the Dirac equation without the spin-dependent term [32,33] and then this term is taken into account in the variational step [30,34]. In spite of this approximation, the latter scheme gives results in close agreement with the former [29], while being simpler to implement. We should also mention the widely used technique in which the SO coupling is added variationally [32] after the scalar relativistic magnetic Hamiltonian has been constructed. In this case, the Pauli equation with the SO coupling is solved instead of the Dirac equation. We should emphasize that all three techniques yield similar results.

The optical conductivity tensor or, equivalently, the dielectric tensor is the basic spectral quantity needed for evaluation of the Kerr effect [7]. The optical conductivity can be computed from the energy band structure by means of the Kubo–Greenwood linear-response expression [14,16]:

$$\sigma_{\alpha\beta}(\omega) = \frac{-ie^2}{m^2\hbar V_{uc}} \times$$
$$\times \sum_{\mathbf{k}}\sum_{nn'} \frac{f(\epsilon_{n\mathbf{k}}) - f(\epsilon_{n'\mathbf{k}})}{\omega_{nn'}(\mathbf{k})}\,\frac{\Pi^{\alpha}_{n'n}(\mathbf{k})\,\Pi^{\beta}_{nn'}(\mathbf{k})}{\omega - \omega_{nn'}(\mathbf{k}) + i\gamma}, \tag{9}$$

where $f(\epsilon_{n\mathbf{k}})$ is the Fermi function, $\hbar\omega_{nn'}(\mathbf{k}) \equiv \epsilon_{n\mathbf{k}} - \epsilon_{n'\mathbf{k}}$ is the energy difference of the Kohn–Sham energies $\epsilon_{n\mathbf{k}}$, and γ is the lifetime parameter, which is included to describe the finite lifetime of excited Bloch electron states. The $\Pi^{\alpha}_{nn'}$ are the dipole optical transition matrix elements, which in a fully relativistic description are given by [35]

$$\Pi_{nn'}(\mathbf{k}) = m\,\langle\psi_{n\mathbf{k}}\,|\,c\boldsymbol{\alpha}\,|\,\psi_{n'\mathbf{k}}\rangle \tag{10}$$

with $\psi_{n\mathbf{k}}$ being the four-component Bloch electron wave functions.

Equation (9) for the conductivity contains a double sum over all energy bands, which naturally separates in the so-called interband contribution, i.e., $n \neq n'$, and the intraband contribution, $n = n'$. The intraband contribution to the diagonal components of σ may be rewritten for zero temperature as

$$\sigma_{\alpha\alpha}(\omega) \equiv \frac{\omega_{p,\alpha}^2}{4\pi} \frac{i}{\omega + i\gamma_D}, \qquad (11)$$

where $\omega_{p,\alpha}$ are the components of the plasma frequency, which are given by

$$\omega_{p,\alpha}^2 \equiv \frac{4\pi e^2}{m^2 V_{uc}} \sum_{n\mathbf{k}} \delta(\epsilon_{n\mathbf{k}} - E_F) \, | \Pi_{nn}^{\alpha} |^2, \qquad (12)$$

E_F is the Fermi energy, and $\gamma_D = 1/\tau_D$, where τ_D is the phenomenological Drude electron relaxation time. The intraband relaxation time parameter γ_D may be different from the interband relaxation time parameter γ. The latter can be frequency dependent [36], and, because excited states always have a finite lifetime, will be nonzero, whereas γ_D will approach zero for very pure materials. The contribution of intraband transitions to the off-diagonal conductivity is usually not considered. Also, the influence of local field effects on the MO properties has not been studied. We mention, lastly, that the Kramers–Kronig transformation was used to calculate the dispersive parts of the optical conductivity from the absorptive parts.

The electronic structure of the MLS was calculated self-consistently on the basis of the local spin density approximation [37] to the density functional theory using the fully relativistic spin-polarized LMTO method [32–34] in the atomic-sphere approximation, including the combined correction (ASA+CC) [32,38]. Core-charge densities were recalculated at every iteration of the self-consistency loop. The spin polarization was included in the variational step [30]. The combined correction terms were also taken into account in the optical matrix element calculations [35]. The basis consisted of s, p, d, and f LMTOs. The $\mathbf{k}$-space integrations were performed with the improved tetrahedron method [39].

2.2. Experimental procedure

The polar Kerr rotation (θ_K) and ellipticity (η_K) spectra were measured with a MO spectrometer based on the polarization modulation technique [40] in the photon energy range 0.8–5.5 eV. Light from a super-quiet Xe arc lamp or D_2 lamp used in the UV region is focused by a condenser on the entrance slit of the monochromator (SPEX 500M), equipped with self-interchangeable gratings for measurements of different parts of the spectrum. The outcoming light beam is filtered by an appropriate filter to attenuate higher orders from the monochromator. After passing through the polarizer and photoelastic modulator (Hinds PEM-90 CaF_2) the light beam is focused by a quartz lens on the surface of the sample mounted on a sample holder with the temperature stabilized in the range 290–800 K inside the 1.8 T water-cooled electromagnets. The amplitude of the retardation of the light is periodically modulated at a frequency of 57 kHz by the modulator, oriented with its strain axis at 45° with respect to the polarizer axis. The angle of incidence of the light on the sample surface is set at 2 and 75 deg in the polar and longitudinal Kerr geometry, respectively. After reflection the light beam passes through the analyzer, oriented parallel or perpendicular to the modulator strain axis, and is detected by a low-noise photomultiplier in the energy range $1.4 < \hbar\nu < 5.5$ eV and by a liquid-nitrogen-cooled Ge photodiode for $0.8 < \hbar\nu < 1.4$ eV. The detector output signal from the current preamplifier is measured by lock-in amplifiers. The polar Kerr rotation and ellipticity, after appropriate calibration with the use of a driven Babinet–Soleil compensator, are derived from the ratio of total light intensity, corrected for zero offset with the use of a controlled light beam shutter, and the intensity of the first and second harmonics. The same setup is used to measure θ_K and η_K hysteresis loops at fixed light wavelength. The setup is fully automated and computer controlled via a data acquisition system (Keithley 500 A). The sensitivity of the Kerr spectrometer is of the order of 10^{-4} deg.

The optical properties – refractive index n and extinction coefficient k – have been measured by spectroscopic ellipsometry using the rotating analyzer method [41] in the spectral range 0.8–5.5 eV. The sample is mounted on a five-axis precision goniometer in a subset of the above described MO system. The ellipsometric angles Ψ and Δ were derived from the real-time digital harmonic analysis of the detected signal modulated by a rotating analyzer. The MgF_2 Rochon analyzer rotates with an angular frequency of 12 s^{-1} inside a rotary encoder with 4096 lines per revolution. The signal from the detectors is synchronously digitized at 20 μs intervals by the Keithley 500 A system and evaluated in real-time using the Hadamard transform. The angle of incidence was set at 67°, optimized as the averaged principal angle of incidence for the measured samples and the spectral range used. The accuracy of setting the angle of incidence is 0.005° and the average error in the determination of n and k values is of the order of 0.003.

3. Magneto-optical properties of Co–Pd systems

3.1. Co/Pd *multilayers*

A detailed experimental and theoretical study of the electronic structure and MO properties of Co/Pd MLS using MOKE spectroscopy and first-principles band-structure calculations has been done in Ref. 42. The Co/Pd multilayers under consideration were prepared on water-cooled glass substrates using the dc magnetically enhanced face-to-face sputtering system described in Ref. 83. The chemical compositions of the films were determined by x-ray fluorescence analysis from the peak intensities of the characteristic fluorescence radiation. Structural studies were performed by conventional x-ray diffractometry. Formation of multilayer structures was confirmed by low angle x-ray diffraction, and the modulation period was deduced from the position of the Bragg peaks. The periods determined from the x-ray measurements agree with those evaluated from the fluorescence analysis. The films were found to be of fcc (111)-textured structure. The parameters of the samples studied are given in Table 1.

Table 1

The parameters of the Co/Pd MLS studied. The sample numbers are given, together with N_{layers}, the number of bilayers, and t_{Co} and t_{Pd}, the measured thicknesses of the Co and the Pd sublayers [42].

No	N_{layers}	t_{Co}, Å	t_{Pd}, Å
1	52	3.5	18.3
2	47	5.2	17.6
3	43	6.4	18.2
4	40	8.4	18.5
5	33	13.8	19.8
6	28	17.4	20.6

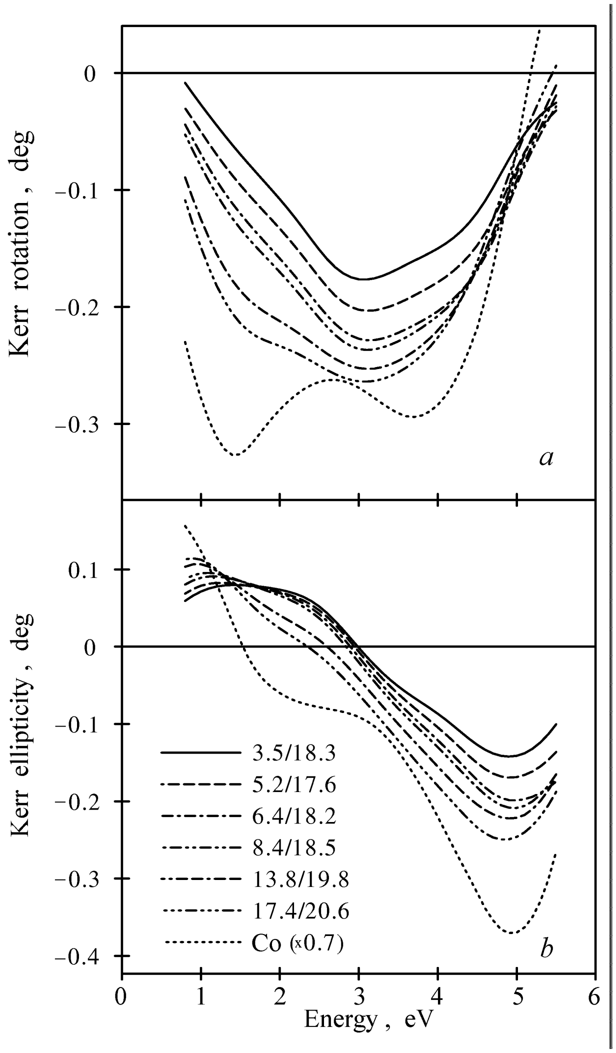

Fig. 1. Experimental polar Kerr rotation (*a*) and ellipticity (*b*) spectra of Co/Pd MLS and fcc Co film. The Co and Pd sublayer thicknesses are given in the keys in units of Å [42].

3.1.1. *Experimental results*

The polar Kerr rotation (θ_K) and ellipticity (η_K) spectra of the Co/Pd MLS measured under saturation conditions are shown in Fig. 1,*a* and *b*. For comparison, spectra of a 2000 Å thick fcc Co film, multiplied by a factor of 0.7, are also plotted in Fig. 1. It can be seen that the MLS Kerr spectra never exceed in magnitude those of the fcc Co over the whole spectral range. The prominent features of the θ_K spectra are a broad negative peak at ~ 3 eV and a shoulder at ~ 4.3 eV, followed by a θ_K slope varying as a function of the Co layer thickness. The θ_K peak, centered at 1.5 eV, characteristic of fcc-Co, is strongly reduced with decreasing MLS Co sublayer thickness, and the prominent minima at ~ 3 eV in θ_K and at ~ 5 eV in η_K diminish in amplitude. The shift of the zero-crossing of η_K up to ~ 3 eV with decrease of the amount of Co present is accompanied by the formation of a positive two-peak structure. Similar spectral features of the Co/Pd MLS, although within smaller spectral ranges and for other sublayer thicknesses, were observed in Refs. [22,43], and [44]. Inspection of the θ_K and η_K spectra of the MLS leads one to the conclusion that there is a MO contribution independent of, or weakly dependent on, the cobalt sublayer thickness. These effects that are independent of the Co content may arise from Pd spin polarization induced by the proximity of Co layers and/or from the polarization caused by roughness and limited alloying at the Co–Pd interface.

To study the mechanism responsible for the MOKE in the Co/Pd MLS and to enable us to discuss the magneto-optical response of the films in terms of separate contributions of the Co and Pd sublattices, the data should, in principle, be analyzed using the off-diagonal optical conductivity tensor components σ_{xy}, which are directly related to the magneto-optical transitions between the spin-polarized electronic states. From the measured θ_K and η_K data, and the diagonal tensor component σ_{xx} the off-diagonal component σ_{xy} can be evaluated according to Eq. (2). The values of σ_{xx} for the fcc Co and Pd films and the Co/Pd MLS under consideration were obtained by an ellipsometric method for the range 0.8–5.5 eV. It was found that the σ_{xx} spectra of the multilayers are close to each other and do not exhibit fine structure, except for a small broad peak at about 4–5 eV.

For all of the Co/Pd MLS studied, it was found that the denominator in Eq. (2) evaluated from the optical data is a monotonic and structureless function over the whole energy range and depends weakly on the film composition. Consequently, all of the peaks in the polar Kerr rotation and ellipticity spectra originate from the corresponding features of the absorptive and dispersive parts of $\sigma_{xy}(\omega)$, respectively. The energy dependence of the denominator in equation (2) only changes the relative amplitudes of the UV and IR peaks of the spectra, without producing any additional spectral features. It can be concluded that in the Co/Pd MLS the MOKE is governed by the off-diagonal part of the optical conductivity tensor.

3.1.2. *Multilayers with perfect interfaces*

In an attempt to reproduce and to explain the experimental MOKE spectra, band-structure calculations of the MO properties of some model MLS were performed. As the influence of the structure of the Co–Pd interface on the MOKE spectra is the subject of this study, in the first step an idealized model with a sharp interface was adopted in the calculations. The numbers n of Co and m of Pd atomic planes in the model nCo/mPd MLS were chosen as close as possible to the experimentally measured ones. For all the MLS, an *abc* stacking sequence of close-packed Co and Pd planes was assumed. In Ref. 45 it was shown that for Co sublayers that are not very thick (less than 30 Å, with the Pd sublayer thickness being 12 Å), the in-plane lattice spacing in Co/Pd MLS is almost independent of the Co sublayer thickness and only ~ 2% less than the lattice spacing in fcc Pd. Therefore the lattice constant $a = 2.694$ Å of the hexagonal lattice was chosen. The interplane spacings in the Co and Pd sublayers and at the interface were chosen to be equal, and correspond to the ideal c/a ratio ($c/a = q\sqrt{2/3}$, where $q = n + m$ is the number of close-packed atomic planes). The sphere radii of Co and Pd were both taken as equal to the average S_{WS} value of 1.49 Å.

The distributions of the spin magnetic moments in the Co and Pd atomic spheres derived from the band-structure calculations are given in Table 2.

Table 2

Calculated Co and Pd spin magnetic moments (μ_B/atom) in the Co/Pd MLS. The number after chemical symbol denotes the number of corresponding atomic planes starting from the Co–Pd interface. For fcc Co with S_{WS} set at the same value as for the MLS, the value of 1.72μ_B/atom was obtained [42].

MLS	Co2	Co1	Pd1	Pd2	Pd3
1Co/8Pd		1.94	0.26	0.12	0.04
2Co/7Pd		1.84	0.23	0.10	0.03
4Co/8Pd	1.72	1.83	0.23	0.11	0.04
6Co/9Pd	1.72	1.83	0.23	0.12	0.04
9Co/9Pd	1.72	1.83	0.23	0.12	0.04

For all the MLS studied, the dependence of the magnetic moments on the distance from the interface is the same. The Co magnetic moment is enhanced at the interface and is already approaching the bulk value of 1.72 μ_B/atom in the second plane. The same value of the Co moment (1.72 μ_B/atom) was obtained from the calculations for fcc Co with the lattice constant expanded so that the value of S_{WS} was equal to that for the MLS. The value of the magnetic moment induced in Pd rapidly decreases with distance from the interface. In the MLS with a Pd sublayer consisting of more than six Pd atomic planes, the magnetic moments induced in the middle of the Pd sublayer are smaller than 0.015 μ_B/atom and are not shown in Table 2. The rapid decrease of the Pd magnetic moment with increase of the distance from the interface can be easily understood if one recalls that the moment is mainly due to Co $3d$ – Pd $4d$ hybridization. A Pd atom even in only the second atomic plane from the interface has no Co atoms among even its second-nearest neighbors, and it interacts with the exchange-split Co $3d$ states only indirectly.

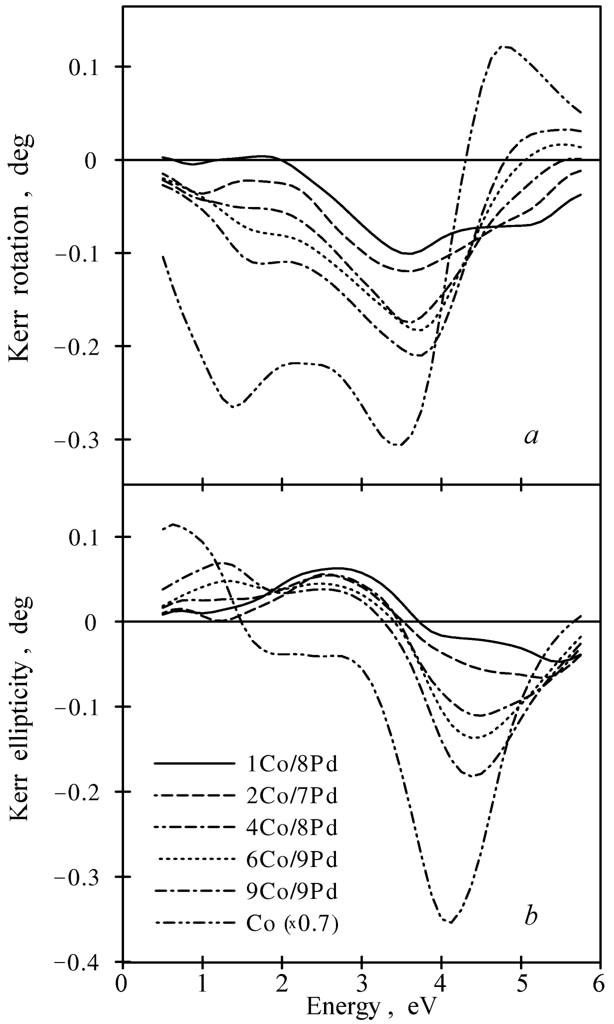

Fig. 2. Calculated polar Kerr rotation (*a*) and ellipticity (*b*) spectra for the model nCo/mPd MLS with sharp interfaces (n and m are the numbers of Co and Pd atomic planes, respectively). For comparison, spectra of fcc Co (calculated with the same value of S_{WS} as the MLS), multiplied by a factor of 0.7, are also shown [42].

The calculated MOKE spectra of the Co/Pd MLS are shown in Fig. 2. For comparison, spectra of fcc Co (calculated with the same value of S_{WS} as the MLS), multiplied by a factor of 0.7, are also shown. From a comparison with the experimental spectra, it is seen that in the UV range the shoulder at ~ 5 eV, which is a characteristic feature of the experimentally measured polar Kerr rotation spectra of the MLS, manifests itself only in the spectra of the 1Co/8Pd MLS and, to a lesser extent, those of the 2Co/7Pd MLS. For the MLS with larger numbers of Co atomic planes, the magnitude of the Kerr rotation spectra in the UV range increases with increase of the Co sublayer thickness, whereas the shape of the spectra changes only slightly. As can be seen in Fig. 2,*b*, the features of the Kerr ellipticity spectra, corresponding to the peaks at 1.0 and 4.3 eV in the fcc Co spectrum, become more pronounced as the number of atomic planes of Co increases.

Such a dependence of the calculated MOKE spectra of the MLS on the Co sublayer thickness is explicable. As the magnetic moment induced in the Pd atoms located far from the interface is very small, one can expect these atoms to give only a small contribution to the off-diagonal optical conductivity. Consequently, if the model with a sharp interface is adopted, the MO properties of the MLS are determined by the Co sublayer and one, or perhaps two, adjacent Pd atomic planes. Also, from the calculated DOS curves and Co magnetic moments it follows that only the electronic states in the two Co atomic planes nearest to the interface are modified strongly by the hybridization with the Pd states. Hence, as the Co sublayer thickness increases, the MOKE spectra of the MLS should become closer to that of pure Co. This is exactly what can be seen in Fig. 2. As the number of Co atomic planes increases, the relative contribution of the interfacial layer to the spectra becomes smaller, and a shoulder appears in the spectra at 1.5 eV which is evidently related to the corresponding peak in the fcc Co spectrum.

A comparison with the experimental spectra of the MLS (Fig. 1) shows that the calculations reproduce only moderately well the main peculiarities of the MOKE spectra of the MLS and the tendencies in the modification of the MLS spectra with the variation of the Co sublayer thickness, and the quantitative agreement is not satisfactory.

The calculated spectra are of smaller magnitude; the decrease of the magnitude for the MLS with a small number of Co atomic planes is larger than in the experiment. The feature at 1.5 eV in the calculated spectra of the MLS with a thin Co sublayer disappears totally, and the magnitude of the spectra goes almost to zero in this energy range. The loss of amplitude at this energy, although observed experimentally, is not so drastic. Also, the calculations predict a rapid decrease of the Kerr rotation amplitude of the shoulder at 5 eV with respect to that of the main minimum as the number of Co atomic planes increases, while the shoulder is observable in the experimental spectra.

It is worth recalling that the spectra of fcc Co shown in Fig. 2 were calculated with the enlarged lattice constant used for the model MLS and, consequently, they should not be compared directly to the experimental Co spectra (see Fig. 1). The position of the UV minimum in the polar Kerr rotation spectrum of Co, calculated using the experimental fcc Co lattice constant (i.e., for $S_{WS} = 1.395$ Å), is shifted to higher energies by ~ 1 eV (see Ref. 74). Thus, the shift of ~ 0.7 eV in the energy position of the UV minimum observed in the experimental MLS spectra with respect to that for the fcc Co film is reproduced — although it is overestimated — by the calculations.

There are several possible sources of these discrepancies. First of all, the peaks in the polar Kerr rotation spectra calculated for either fcc or hcp Co are shifted to higher energies with respect to the measured ones, and the magnitude of the minimum at 1.5 eV is too small. This discrepancy is apparently due to a failure of the LDA-based calculations to predict correctly the MOKE spectra of the ferromagnetic 3*d* metals; this failure has recently been extensively discussed in the literature [74,85,86]. A plausible cause for this lies in the approximate description of the exchange and correlation of rather localized 3*d* electrons. If the calculated magnitude of the IR peak of fcc Co were larger, it would bring the theoretical MOKE spectra of the MLS into closer agreement with the experimental ones for the energy range below 2 eV. In the UV range, however, a shift of the Co Kerr rotation peak to lower energies would hardly improve the agreement between the theory and experiment at all.

The shift of the calculated peak positions may also be caused by the difference between the experimental interatomic distances and those used in the calculations. Determination of the in-plane and interplane distances in an individual sublayer of the MLS or overlayered structures is an onerous task, and the experimental data available for Co/Pd MLS differ significantly [34–36]. To estimate the sizes of the possible effects of the interplane relaxation, test calculations using the unmodified in-plane interatomic distance but a smaller c/a ratio were performed for Co (with a hexagonal supercell) and 4Co/5Pd MLS. It was found that the theoretical MOKE spectra are rather insensitive to the interplane distance. A decrease of the c/a ratio by 5% results in a small increase in amplitude of the polar Kerr rotation spectra, but the peak positions remain unchanged. Thus, although a contraction of interplane distances in the Co sublayer has been derived from structural investigations [46,47], it is unlikely to be responsible for the discrepancies between the theoretical and experimental MOKE spectra of the Co/Pd MLS. An in-plane relaxation in a thick Co sublayer might affect the calculated MOKE spectra strongly, but performing such a calculation is beyond the capability of our facilities. Moreover, there is no experimental evidence that relaxation really occurs in the MLS studied.

The idea of enhanced spin polarization in the Pd planes adjacent to the Co has also been considered. For some of the MLS studied, test calculations were performed in which an additional exchange splitting was introduced for one or two of the Pd atomic layers nearest to the interface. As a result of the additional spin polarization of the Pd atoms, the intensity of the calculated polar Kerr rotation spectra in the UV range increases. However, the strong positive rotation at low photon energies worsens the agreement with the experiment in this energy range.

It can be concluded that the main cause of the differences between the theory and experiment lies in the choice of a model with a sharp interface as a basis for the calculations. An intermixing at the interface, even within just one or two atomic layers, can appreciably change the shape and magnitude of the MOKE spectra of the MLS, especially those with small Co sublayer thicknesses. The next part of this Section is devoted to a quantitative study of this problem.

3.1.3. Multilayers with imperfect interfaces

From the discussion above, it follows that interfacial intermixing should be taken into account if one is to describe the MO properties of real Co/Pd MLS systems. A first improvement that takes us closer to describing «real» systems is that of considering an ordered compound at the interface. To examine the consequences of interfacial intermixing for Co/Pd MLS MOKE spectra and their relation to the chemical nature of the interface, a model of multilayer supercells with alloyed interfaces was considered. The study was performed with the use of the above-described formalism of *ab initio* band-structure calculations. As the LMTO method requires a crystal lattice with specified translational and point symmetry, special model supercells of the multilayered structures with alloyed interfaces and fcc (111) texture were constructed. In the [111] direction, for all model MLS an *abc* stacking sequence of close-packed atomic Co and Pd planes was assumed. As an interface between the neighboring Co and Pd layers, one or two Co–Pd mixed atomic planes were introduced. To satisfy the requirement of overall D^3_{3d} lattice symmetry of the supercells and to minimize their volume, the unit cell was doubled in the basal plane. As a consequence, interfacial planes in these supercells can consist of mixed atomic planes composed of an ordered Co–Pd compound with 1:3 and 3:1 stoichiometry and threefold rotational symmetry. Three

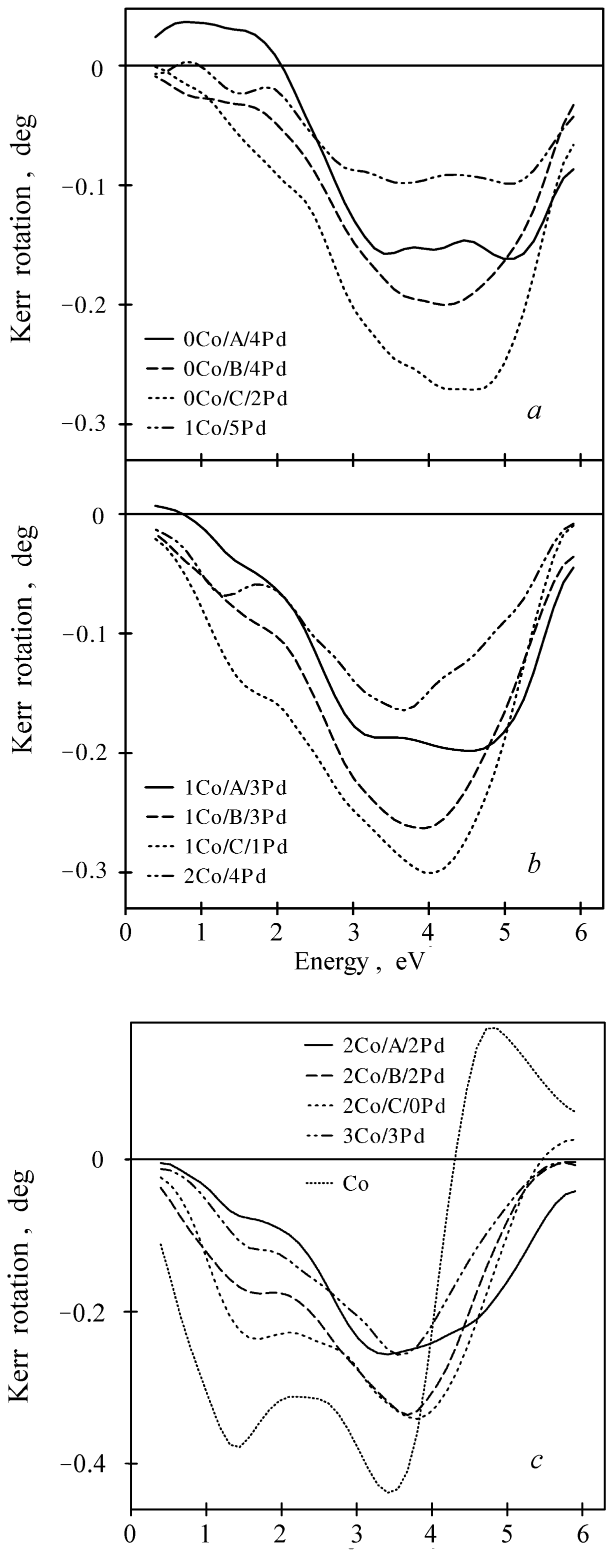

Fig. 3. Calculated polar Kerr rotation spectra for the model nCo/X/mPd multilayered structures with imperfect interfaces, n and m are the numbers of Co and Pd atomic planes, respectively. X = A, B, C denotes the interfacial planar ordered alloys Co_1Pd_3 , Co_3Pd_1, and Co_3Pd_1/Co_1Pd_3 , respectively. For a comparison, the corresponding MLS spectra for the ideal model nCo/mPd and the spectrum of fcc Co with the same value of S_{WS} as for the MLS are also shown [42].

types of multilayered structure with different interfacial atomic planes were considered. The structures of the nCo/A/mPd and nCo/B/mPd types contain Pd-rich Co_1Pd_3 (A) and Co-rich Co_3Pd_1 (B) ordered interfacial planar alloys, respectively. The structure nCo/C/mPd with C = Co_3Pd_1/Co_1Pd_3 has a two-layer interfacial ordered alloy composed of consecutive B- and A-type planes.

To understand the relationship between the interfacial structures and the MOKE spectra, a systematic study was performed for Co/Pd MLS with a period of six atomic layers. Calculations for larger supercells are extremely time consuming and were performed only for some selected cases. It was found that the calculations performed are sufficiently representative and illustrate the main trends in the modification of the MO spectra with interface imperfection. In all of the calculations, the same lattice constant as for the ideal model MLS was assumed.

The calculated polar Kerr rotation spectra for the Co/Pd MLS, where the Co and Pd layers are separated by three types of interfacial alloy layer (A, B, and C), are shown in Figs. 3,a–3,c. For comparison, the spectrum of fcc Co calculated with the same value of S_{WS} and the spectra of ideal 1Co/5Pd, 2Co/4Pd, and 3Co/3Pd MLS are also included. The spectra calculated for the supercell structures in which the Pd layers are separated by alloy layers only are presented in Fig. 3,a. The supercells 0Co/A/4Pd and 0Co/B/4Pd consist of a two-atomic-layer thickness of alloy, of either Co_1Pd_3 or Co_3Pd_1 composition, separated by a four-atomic-layer thickness of Pd spacer. The supercell 0Co/C/2Pd consists of repeated sequences of four alloy atomic planes, $Co_1Pd_3/Co_3Pd_1/Co_3Pd_1/Co_1Pd_3$, separated by two Pd atomic planes. These structures can be regarded as limiting cases, where Co atoms are present in alloy planes only.

As is seen from Fig. 3,a, in the UV range the main features of the 0Co/A/4Pd spectrum are very similar in shape to those of the 1Co/5Pd MLS with the sharp interface. It is interesting that the amplitude of the 0Co/A/4Pd spectrum is about 70% higher than the amplitude of the 1Co/5Pd spectrum, despite the higher Co content in the latter. However, in the energy range below ~ 2 eV positive rotation is observed for the 0Co/A/4Pd MLS. It should be noted that the overall shape of the 0Co/A/4Pd Kerr rotation spectrum is very close to that calculated for homogeneous diluted Co–Pd alloys [48]. Thus, the conclusions are that the Kerr rotation spectrum of the 0Co/A/4Pd structure is determined to a great extent by the MO properties of spin-polarized Pd. The spectrum of 0Co/B/4Pd, in which the interface region is formed by the Co-rich alloy, differs significantly from both the 0Co/A/4Pd and the 1Co/5Pd spectra. The two-peak UV structure transforms into a broad minimum centered at 4.2 eV and in the IR region the rotation becomes negative. The structure with a *C*-type interfacial layer is particularly interesting, as it can be obtained from the ideal 2Co/4Pd multilayer structure simply by interchanging the positions of every fourth Co and Pd atom in the neighboring interfacial Co and Pd layers. As a result, Co-rich Co_3Pd_1 and Pd-rich Co_1Pd_3 planar alloy layers appear around the border. The composition of the 0Co/C/2Pd MLS corresponds to that of 2Co/4Pd; however, it should be pointed out that the change of the interface microstructure leads to very large changes in the shape and magnitude of the MO spectra, as can be seen from the comparison of the 0Co/C/2Pd and 2Co/4Pd Kerr rotation spectra in Figs. 3,*a* and 3,*b*, respectively.

The Kerr rotation spectra are modified appreciably upon addition of one (see Fig. 3,*b*) or two (see Fig. 3,*c*) Co atomic planes to an MLS with an imperfect interface. In the supercells, the Co and Pd planes are separated by *A*-, *B*-, and *C*-type interfacial layers. The essential points as regards the modification of the spectra can be summarized as follows:

(i) The amplitude of the spectra increases as the amount of Co increases. In the IR spectral range, the characteristic features of the Co spectrum become more pronounced.

(ii) For the supercells containing one planar alloy of Co_1Pd_3 composition treated as an interface region, the change of the relative amplitudes of the characteristic peaks in the UV region upon addition of two Co atomic planes is clearly visible.

(iii) For the supercells containing as an interface region a single Co_3Pd_1 atomic plane or two Co_3Pd_1/Co_1Pd_3 atomic planes, the main effect of increasing the number of Co atomic planes is a shift of the UV peak position to lower energy. This effect is accompanied by a narrowing of the bandwidth.

(iv) The amplitudes of the spectra in the energy range above 4 eV are up to 100% higher than those of the ideal 2Co/4Pd and 3Co/3Pd MLS.

From the band-structure calculation results it follows that the Co and Pd electronic states in the alloy interface layers are strongly modified by the hybridization. As the volume in which the hybridization occurs is significantly larger in a MLS with an imperfect interface, the contribution of these hybridized states to the MO spectra increases compared to that for a MLS with an ideal interface. Hence, the similarity between the *n*Co/A/*m*Pd MLS spectra and the spectra of Pd-rich CoPd alloys [48] becomes closer, especially for the MLS with a small Co sublayer thickness. Another effect of interfacial alloy formation is stronger — compared to that for the ideal MLS — spin polarization of the whole Pd spacer. The averaged magnetic moment per Pd atom calculated for the different structures approaches values up to 80% larger than those for the ideal MLS models. One can expect that as a result of the increased magnetic moment induced on the Pd atoms, they will make larger contributions to the MO spectra. This can be clearly seen in the energy range below 2 eV, where the Kerr rotation spectra are very sensitive to the Pd contribution. As was established earlier [48,49], the interband magneto-optical transitions in spin-polarized Pd give a positive Kerr rotation in the IR energy range, whereas the transitions between the electronic states with a large degree of admixture of Co 3d states result in a negative contribution to the Kerr rotation in this range, even when the Co states are considerably modified by the hybridization with Pd states. As a result of the two compensating contributions, the amplitude of the Kerr rotation spectra of the MLS is suppressed in the IR energy range and the rotation becomes positive in the case of 0Co/A/4Pd MLS (see Fig. 3,*a*). As the number of Co atomic planes increases, their relative contribution to the MOKE spectra becomes higher and the Kerr rotation in the IR range becomes negative, which brings the spectra closer to the fcc Co spectrum, as can be seen in Fig. 3. A peak appearing at 1.5 eV in the MLS spectra is evidently related to the corresponding peak in the fcc Co spectrum.

As is seen in Fig. 3,*a*, in the UV spectral range the contribution to the MLS spectra coming from the interfacial alloy region and strongly polarized Pd atomic planes is also rather large, contrary to the case for the ideal model of the MLS, and controls the spectral shape in that energy range. The observed overall increase of the rotation amplitude along the sequence 0Co/A/4Pd, 0Co/B/4Pd, and 0Co/C/2Pd is related to an increase of the relative Co content in the structures, which changes from 8% in 0Co/A/4Pd up to 33% in 0Co/C/2Pd. If one or two Co atomic planes are included in the structures, the relative contribution of Co to the total Kerr spectra increases. Hence, the shape of the spectra becomes closer to that of the fcc Co spectra, and the enhancement of the Kerr rotation peak amplitude in the UV range can be seen in Figs. 3,*b* and 3,*c*. It is worth pointing out, however, that the MOKE spectra are not simple superpositions of the contributions arising from the constituent sublayers.

It was found that of all the model MLS considered, the models in which the interfacial alloy layer is a Pd-rich alloy reproduce better the main spectral features of the experimentally studied Co/Pd MLS and the tendencies in the modification of the spectra as the thickness of the Co sublayer increases. In Fig. 4, the MOKE spectra calculated for the ideal 2Co/7Pd MLS and the 2Co/(Co$_1$Pd$_3$)/5Pd model structure are directly compared to the experimental spectra of the 3.5 Å Co/18.3 Å Pd MLS with sublayer thicknesses closest to the model structure. It is clearly seen that, if the interfacial alloying is taken into account, the characteristic shape of the measured spectrum with the shoulder in the UV range is reproduced well by the calculations. Also, the amplitude of the calculated Kerr rotation is close to the experimentally studied one, unlike the case of the ideal model 2Co/7Pd MLS with the same period, for which the amplitude is 50% smaller. The enhancement of the calculated amplitude and better agreement with the experiment can be observed also for the Kerr ellipticity spectra.

To study the effect of total interlayer intermixing on the MOKE spectra and as a final test of the assumed interface model, the 3.5 Å Co/18.3 Å Pd MLS film was annealed under high vacuum at 800 K for 5 h. At such high temperatures the diffusion processes are very intensive and the whole layered structure is uniformly homogenized, becoming a disordered fcc alloy film of effective composition Co$_{0.2}$Pd$_{0.8}$, as was controlled by our structural study. The huge changes of the MOKE spectra after annealing can be seen from Fig. 4. The Kerr rotation and ellipticity spectra amplitudes increase significantly and the spectral shapes become close to those observed for Co–Pd alloys of comparable composition [48]. The calculated MOKE spectra of disordered Co$_{0.25}$Pd$_{0.75}$ alloy taken from Ref. 48 are also included in Fig. 4 for comparison. As can be seen, the agreement of the calculated and measured Kerr rotation and ellipticity spectra of the alloyed structure is excellent (the systematic shifts of the spectra on the energy scale are of common nature for LDA-based calculations, as was discussed in Sec. 3.1.2.). Thus, on the basis of the results obtained for the Co/Pd MLS, the following conclusions have been reached:

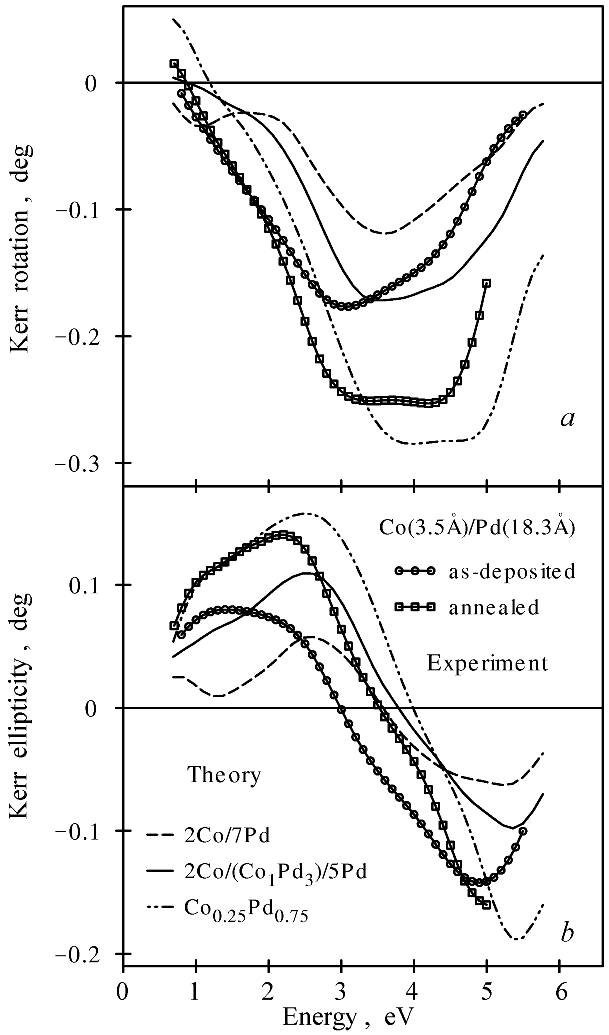

Fig. 4. Comparison of the measured and calculated polar Kerr rotation (*a*) and ellipticity (*b*) spectra of the as-deposited 3.5 Å Co/18.3 Å Pd MLS film and the model 2Co/(Co$_1$Pd$_3$)/5Pd as well as the ideal 2Co/7Pd MLS model. The spectra of the film annealed at 800 K and calculated for the model of fcc disordered Co$_{0.25}$Pd$_{0.75}$ alloy are included [42].

(i) the MLS studied have relatively sharp interfaces with a «chemical thickness» of the order of one atomic layer; and

(ii) they can be well described by a model MLS structure with an ordered Pd-rich interfacial alloy.

In the real Co/Pd MLS the interface microstructure may be more complicated, and probably only partial chemical ordering occurs. As was inferred from the x-ray diffraction data, the Co/Pd MLS studied have well-defined layered structure. Nevertheless, some intermixing at the interface during the samples' deposition process is very probable. This effect leads, in turn, to higher induced spin polarization in a larger volume of Pd and makes the whole volume magneto-optically active. The results obtained allow us to explain the origin of the observed

MOKE spectra of the MLS and to understand why the thickness of the so-called «magnetic interface» can be larger than that of the «crystallographic» one, as was recently reported for other Pd-based multilayered systems [50]. The conclusions are also consistent with the results derived from the phenomenological multireflection approach, not presented here, which indicate that the Pd spin polarization extends through a depth of the order of four Pd atomic layers.

In conclusion it should be pointed out that in the Co–Pd systems the MOKE is governed by the off-diagonal part of the optical conductivity tensor. It was found that the *ab initio* calculations performed for model Co/Pd MLS with sharp interfaces reproduced the main peculiarities of the experimental Co/Pd MOKE spectra only moderately well. It is shown that the main peculiarities and the tendencies in the modification of the MLS spectra with the variation of the Co sublayer thickness are adequately reproduced when the alloying, even limited to one atomic plane, is taken into account. The MOKE spectra calculated for the model structures with ordered Co_1Pd_3 interfacial planes reproduce the measured spectra best. The results obtained demonstrate that interface microstructure plays a crucial role in the formation of the MOKE spectra of the Co/Pd layered structures.

3.2. Co_xPd_{1-x} *alloys*

In real MLS systems chemical and structural disorder often occurres at the interface. These effects can be examined using model disordered alloys.

The description of the magneto-optical properties of a disordered system on a microscopic level and understanding of the effect of chemical order and crystal symmetry on these properties are of great importance. The most powerful approach to calculating the electronic structure of randomly disordered solids is the coherent potential approximation (CPA) in connection with the Korringa–Korr–Rostoker method of band structure calculation (KKR-CPA) [51]. Within this formalism a quantitative description of such phenomena as magnetoresistance [52] and x-ray dichroism [53] was obtained. In both cases the central quantity to be calculated is the optical conductivity tensor [8]. Unfortunately, techniques for dealing with that quantity for finite frequencies in the optical regime of light have not yet been developed. For that reason the theoretical investigations of the optical and magneto-optical properties of disordered Co_xPd_{1-x} alloys in Ref. 48 was done using the supercell approximation. To test the theoretical approach, the MOKE spectra for a set of Co_xPd_{1-x} polycrystalline alloy films with $x = 0.13$, 0.22, 0.31, and 0.44 have been also measured.

To investigate the influence of composition and local environment on the MO properties of disordered alloys, *ab initio* band-structure calculations for *ordered* Co–Pd alloys (Co_1Pd_{15}, Co_1Pd_{11}, Co_1Pd_7, Co_2Pd_{10}, Co_4Pd_{12}, Co_3Pd_9, Co_2Pd_6, Co_1Pd_3, and Co_1Pd_1) have been performed. This sequence corresponds to a variation of the Co content in the range of 6–50%. For Co_1Pd_1 and Co_1Pd_3 alloys the AuCu ($L1_0$) and $AuCu_3$ ($L1_2$) structures, respectively, were assumed. The supercells for all the other alloys except Co_1Pd_{11} consist of two or more adjacent fcc unit cells with Co and Pd atoms distributed over nonequivalent atomic positions according to the specific alloy composition. For the Co_1Pd_7 and Co_1Pd_{15} alloys both cubic and tetragonal supercells were constructed, whereas for the Co_1Pd_{11} alloy a hexagonal unit cell was used. The lattice constant for all the alloys has been chosen to correspond to the experimental data [54].

As was mentioned above, the magneto-optical effects are determined by the dielectric tensor components $\varepsilon_{\alpha\beta}$. This tensor can be represented as a sum $\varepsilon_{\alpha\beta} = \varepsilon^s_{\alpha\beta} + \varepsilon^a_{\alpha\beta}$ of two parts which are symmetric (optical) and antisymmetric (magneto-optical) with respect to the magnetization direction. That is, the relations $\varepsilon^s_{\alpha\beta}(\mathbf{M}) = \varepsilon^s_{\alpha\beta}(-\mathbf{M})$ and $\varepsilon^a_{\alpha\beta}(\mathbf{M}) = -\varepsilon^s_{\alpha\beta}(-\mathbf{M})$ hold, where **M** denotes the magnetization vector. The antisymmetric part $\varepsilon^a_{\alpha\beta}$ can be expressed as $\varepsilon^a_{\alpha\beta} = ie_{\alpha\beta\gamma}\, g_\gamma$, where $e_{\alpha\beta\gamma}$ is the antisymmetric pseudo-tensor and g_γ is a component of the gyration vector **g** [55].

For most materials the relation $|\mathbf{g}| << \det \|\varepsilon^s_{\alpha\beta}\|$ holds, and expressions for all nonreciprocal magneto-optical effects, measured usually as a difference quantity with respect to a reversal of the magnetization, can be decomposed into the product of the complex number $\mathbf{g}\hat{\mathbf{g}}$ and some function depending on the optical part of the dielectric tensor $\varepsilon^s_{\alpha\beta}$ as well as the light propagation and magnetization directions (see, e.g., Ref. 25).

It should be noted that although the optical part of the dielectric tensor may play a crucial role in the MO spectra formation, like, for example, in CeSb [56], or may exhibit a noticeable anisotropy [57], this is not the case for the Co–Pd compounds investigated here. It was found that in the energy range $0.5 < \hbar\nu < 6$ eV the calculated components $\varepsilon^s_{\alpha\beta}$ are smooth and exhibit only a very weak dependence on both the chemical ordering and the alloy composition. Moreover, for the uniaxial

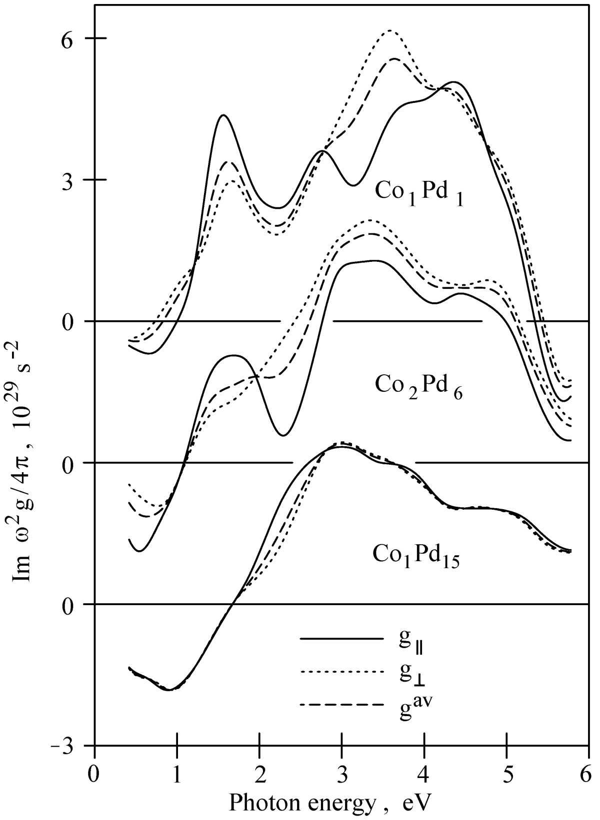

Fig. 5. Orientation dependence of the Im $\omega^2 g(\omega)$ spectra for the Co_1Pd_1 , Co_2Pd_6 and Co_1Pd_{15} . All spectra were convoluted with a Lorentzian of width 0.5 eV [48].

model structures the optical anisotropy defined as $\delta_A = (\varepsilon_{\perp} - \varepsilon_{\parallel})/\epsilon$ does not exceed 5%. Here we denoted $\epsilon = \frac{1}{3}(2\varepsilon^s_{\perp} + \varepsilon^s_{\parallel})$, where $\varepsilon^s_{\perp}$ and $\varepsilon^s_{\parallel}$ stand for the main optical dielectric tensor components corresponding to the light polarization perpendicular and parallel to the n-fold symmetry axis (c) of the crystal. Thus, all features of the MO spectra of the Co–Pd compounds are determined by the $g(\omega)$ function.

As was mentioned above, our calculations involved both cubic and uniaxial models. For the crystal with cubic symmetry the dependence of g on the magnetization direction $\hat{\mathbf{M}}$ is negligible [84], whereas for uniaxial crystals it can be noticeable. Uspenskii et al. [58] have shown that, up to the second order the in spin–orbit coupling strength, this dependence can be expressed in terms of the gyration vectors $g_{\parallel}$ and $g_{\perp}$ calculated for the cases $\hat{\mathbf{M}} \parallel c$ and $\hat{\mathbf{M}} \perp c$, respectively:

$$\mathbf{g} = \hat{\mathbf{M}}(g_{\parallel}\cos^2\theta + g_{\perp}\sin^2\theta) + \hat{\mathbf{n}}(g_{\parallel} - g_{\perp})\sin\theta\cos\theta\ , \qquad (13)$$

where $\hat{\mathbf{n}}$ stands for the unit vector, orthogonal to $\hat{\mathbf{M}}$ and lying in the same plane as $\hat{\mathbf{M}}$ and $\mathbf{c}$, and θ is the angle between the magnetization vector $\mathbf{M}$ and n-fold symmetry axis c.

Figure 5 presents the calculated Im $\omega^2 g_{\parallel}(\omega)$ and Im $\omega^2 g_{\perp}(\omega)$ spectra for a selected set of uniaxial crystals. One can see that for Co_1Pd_1 and Co_2Pd_6 the orientation dependence of the gyration vector is rather strong and manifests itself in changes of the relative magnitude and energy location of both the IR and UV maxima. The feature at 2.5 eV in the $g_{\parallel}(\omega)$ spectra disappears completely for $\mathbf{M} \perp c$. For the more diluted tetragonal Co_1Pd_7 alloy the orientation dependence of the $g(\omega)$ spectra was found to be relatively weak, and it practically disappears for Co_1Pd_{15} (see Fig. 5). The same tendencies were found also for the Re $\omega^2 g(\omega)$ spectra.

To take into account the effects of random orientation of microcrystals in the alloys studied, we have to average Eq. (13) over different relative orientations of the crystal axes and magnetization direction, which gives

$$g^{av}(\omega) = \frac{1}{3}\,[2g_{\perp}(\omega) + g_{\parallel}(\omega)]\ . \qquad (14)$$

The main effect of the averaging (see Fig. 5) on the Co_1Pd_1 spectrum is a change of the band shape in the UV range as compared to the spectrum calculated with the magnetization directed along the c axis. The position of the main UV maximum shifts to lower energy and in Co_2Pd_6 the band becomes broader. In both alloys the structure at ~ 1.5 eV becomes less pronounced.

To study the dependence of the MO spectra on chemical ordering, let us consider the results for alloys with 1:3 stoichiometry. Calculations were done for the cubic $L1_2$ phase and for the tetragonal $D0_{22}$, $D0_{23}$, Co_3Pd_9 , and second kind of Co_4Pd_{12} supercells. Tetragonal supercells Co_3Pd_9 and Co_4Pd_{12} consisting of one and two more central planes, respectively, as compared to the $D0_{22}$ structure, were used. All the alloys have the same nominal composition of $Co_{0.25}Pd_{0.75}$ but differ in the symmetry and local environment of the Co and Pd sites. While all these structures have identical first neighbor coordination (each Co has 12Pd neighbors and each Pd has 8Pd+4Co neighbors), there are differences in the second atomic shell. For the $L1_2$, $D0_{22}$, and $D0_{23}$ cells each Co has 6Co, 4Co+2Pd and 5Co+1Pd second neighbors with local site symmetry O_h , D_{4h} , and C_{4v} , respectively. The atomic coordination around Pd in the second shell consists of 6Pd for the $L1_2$ structure, while there are two inequivalent Pd sites for $D0_{22}$ (with 6Pd and 2Co+4Pd) and for $D0_{23}$ (with 6Pd and 1Co+5Pd). These three structures will be taken as

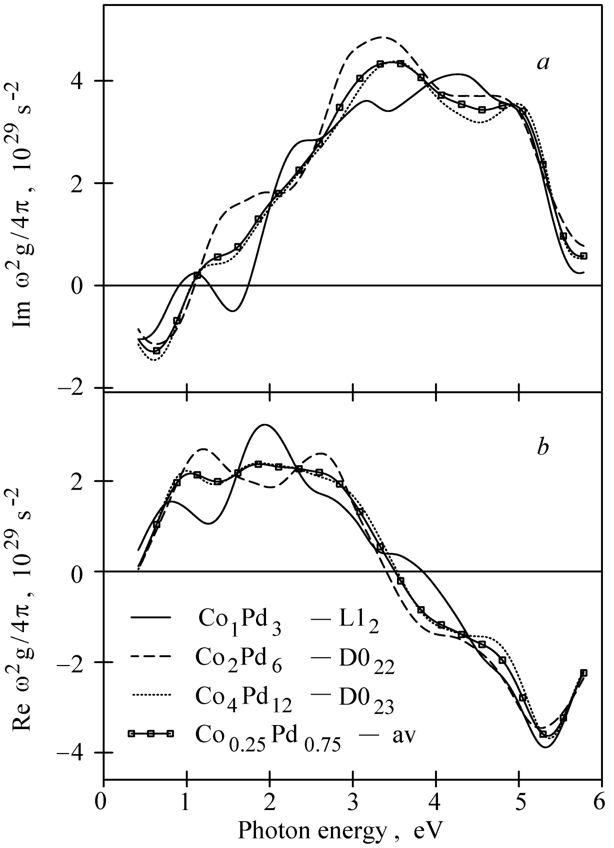

Fig. 6. Effect of the chemical order on the calculated $\omega^2 g(\omega)$ spectra of $Co_{0.25}Pd_{0.75}$ alloy [48].

basic because the other structures studied, like Co_3Pd_9 and Co_4Pd_{12}, are composed of various numbers of the above described inequivalent Co and Pd sites.

In Fig. 6 the spectra of the imaginary (*a*) and real (*b*) parts of $\omega^2 g(\omega)$ are shown. For Co_2Pd_6 ($D0_{22}$) and Co_4Pd_{12} ($D0_{23}$) alloys $\omega^2 g^{\mathrm{av}}(\omega)$ is presented. As a result of the change of the atomic arrangement and accompanied lowering of the symmetry of the local sites along the sequence $L1_2$–$D0_{22}$–$D0_{23}$, the spectra become less structured and the peaks broaden, as can be seen, for example, by comparing the Re $\omega^2 g(\omega)$ spectra in the spectral range up to 3 eV. This effect apparently arises from the fact that lowering of the local symmetry of atomic sites generally leads to the appearance of an increasing number of nonequivalent interband transitions, with their contributions to the MO spectra spread out over a wider energy range. It was found that the resulting $\omega^2 g^{\mathrm{av}}(\omega)$ spectra calculated for Co_3Pd_9 and Co_4Pd_{12} alloys can be well reproduced by averaging the basic $L1_2$, $D0_{22}$, and $D0_{23}$ spectra, weighted by the corresponding numbers of equivalent sites in these structures.

To estimate the $\omega^2 g^{\mathrm{av}}(\omega)$ spectrum of the disordered $Co_{0.25}Pd_{0.75}$ alloy it is necessary to adopt a procedure of averaging the spectra over possible atomic arrangements. Here the simplest assumption was made: that the basic cells appear with equal probabilities and that the contribution of each cell to the spectrum is proportional to its number of atomic sites. On this basis the averaged spectrum was obtained as the weighted average of the $L1_2$, $D0_{22}$, and $D0_{23}$ spectra with the weights of 1, 2, and 4, respectively. As a result of the configuration averaging, the spectrum becomes less structured and is closest to the spectrum of the $D0_{23}$ structure (see Fig. 6). It can be concluded that for the alloys studied the local atomic arrangement and site symmetry control the MO properties.

To discuss the composition dependence of the MO properties of the alloys under consideration, we focus here on the polar Kerr rotation spectra, because they are the quantities measured directly in the experiment. If the optical anisotropy δ_A is small, the complex Kerr rotation angle, neglecting the second-order quantities (δ_A^2, $\delta_A\, g$, and g^2), has the form

$$\phi_K = \vartheta_K + i\eta_K = g/[\sqrt{\epsilon}(1-\epsilon)] \,. \qquad (15)$$

Equation (15) is linear with respect to g and this allows us to use for the uniaxial systems g^{av} instead of g. To take into account finite-lifetime effects the calculated spectra were convoluted with a Lorentzian of width 1.0 eV. Calculated polar Kerr rotation and ellipticity spectra of Co–Pd alloys of different compositions are shown, together with experimentally measured ones, in Fig. 7. To take into account the decrease of Curie temperature for diluted alloys, all experimental spectra have been scaled with the factor $M_{4.2}/M_{300}$, where $M_{4.2}$ and M_{300} are the magnetization at 4.2 K and 300 K, respectively. Both experimental and theoretical data exhibit the same features. As the Co content diminishes, the magnitude of the rotation angle in the energy range 2.5–4.5 eV decreases. The shoulder at ~ 1.5 eV, clearly seen in the ϑ_K spectrum of Co_1Pd_1 alloy, disappears completely in diluted alloys, and the Kerr rotation changes sign below ~ 2 eV. In the UV range, the peak centered at 4 eV in Co_1Pd_1 transforms into a broad two-peak structure. Also, a shift of the Kerr ellipticity zero-crossing to higher energy with decrease of Co content is observed, as well as a diminishing of the amplitude at ~ 5 eV. However, the calculated peak positions of both the Kerr rotation and ellipticity are shifted slightly to higher energies with respect to the experimental ones. The discrepancy is apparently due to a drawback of the LDA-based calculations which has recently been discussed extensively in the literature [74,82].

It is interesting to note that the calculated MOKE spectra of Co_2Pd_{10}, Co_1Pd_7, Co_1Pd_{11}, and also Co_1Pd_{15} alloys are close to each other, although the Co content in the alloys decreases from 16.5% to as low as 6%. From this one can conclude that the MOKE spectra of diluted Co–Pd alloys are determined to a great extent by the MO properties of spin-polarized Pd. This is in line with the relatively large average Pd magnetic moment obtained from the calculations (e.g., $0.24\mu_B$/atom for Co_1Pd_{15}) which depends weakly on Co content in the Co–Pd alloys.

It should be noted that the theoretical spectra shown in Fig. 7, except for the spectrum of $Co_{0.25}Pd_{0.75}$, have been obtained for one specific atomic arrangement. In Fig. 7 the theoretical spectrum for $Co_{0.25}Pd_{0.75}$, obtained as the weighted average of the spectra for $L1_2$, $D0_{22}$, and $D0_{23}$ structures according to the procedure described above, is presented. As a result of the averaging over different atomic configurations, the MOKE spectrum of $Co_{0.25}Pd_{0.75}$ becomes less structured, and the minimum in the polar Kerr rotation spectrum, centered at about 4.5 eV in the ordered Co_1Pd_3–$L1_2$, transforms into a broad structure like that observed in the measured spectrum of the disordered $Co_{0.22}Pd_{0.78}$ alloy film.

It can be concluded that the MOKE calculations in which the effects of random orientation of microcrystals and/or chemical disorder are taken into account reproduce well the experimental spectra of the Co–Pd disordered alloys and the dependence of the spectra on the composition. The optical part of the dielectric tensor of these compounds depends very weakly on both the alloy composition and chemical ordering and does not show noticeable anisotropy for the uniaxial crystals. Moreover, its frequency dependence is structureless and all features in the magneto-optical spectra are determined by the gyrotropic part of the dielectric tensor, which exhibits a considerable orientation anisotropy increasing with the Co content.

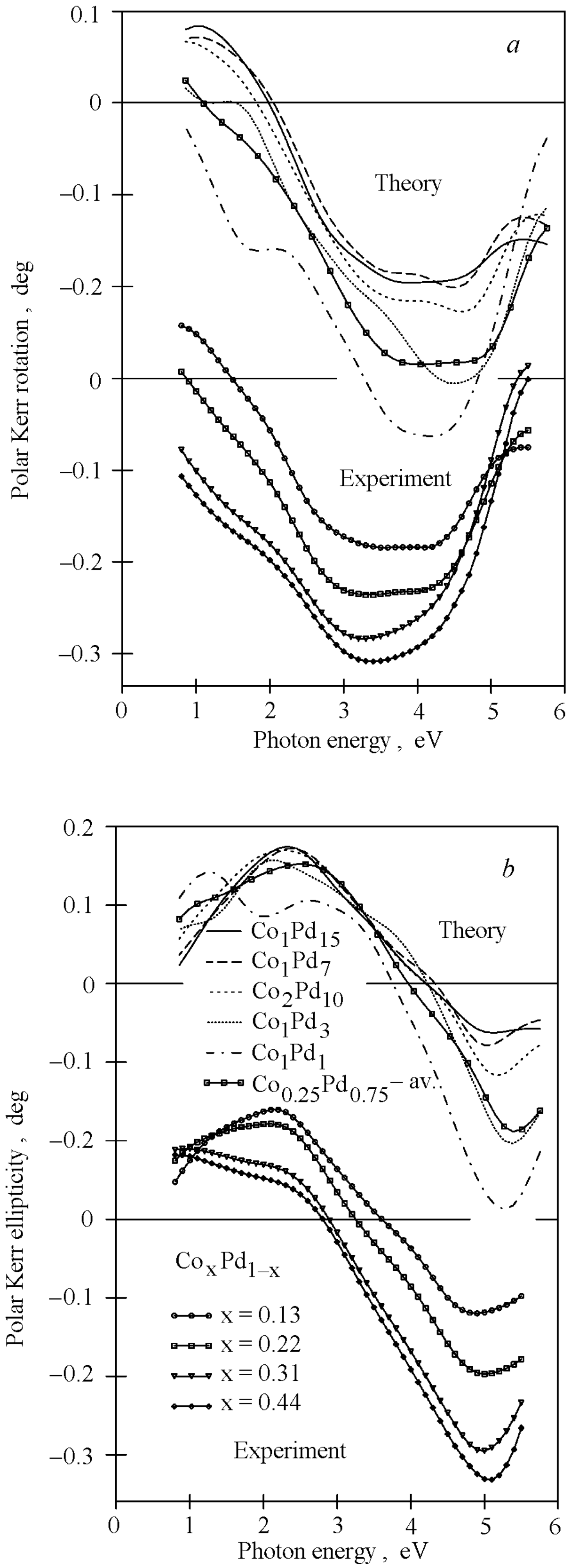

Fig. 7. Comparison of the calculated and experimental polar Kerr rotation (*a*) and ellipticity (*b*) spectra for the different composition of the Co–Pd alloys [48].

4. Magneto-optical properties of Co/Pt multilayers

4.1. Experimental results

A detailed experimental study of the MO properties of Co/Pt MLS using MOKE spectroscopy has been done in the Ref. 74 for the series of sputter-deposited MLS listed in Table 3.

Table 3

The parameters of the Co/Pt MLS studied. No is the sample number, N_{layers} is the number of bilayers, t_{Co} (t_{Pt}) are measured thicknesses of Co (Pt) sublayer [74].

No	N_{layers}	t_{Co} , Å	t_{Pt} , Å
1	50	4.6	13.6
2	47	5.8	15.2
3	43	6.9	12.5
4	40	9.0	14.4
5	33	18.9	14.3

The measured polar Kerr rotation and ellipticity spectra of the Co/Pt MLS studied are shown in Fig. 8. All samples measured possess well-defined MOKE hysteresis curves with saturation characteristics, and all θ_K and η_K spectra were measured under saturation conditions. The Kerr rotation spectra display two well-known features. There is a prominent broad, negative peak in the UV region and a smaller one in the IR part. The IR peak, centered at 1.5 eV, is most prominent for a pure Co thick film [59], and for MLS its amplitude continuously diminishes with decreasing MLS Co sublayer thickness. The UV peak varies slightly in energy position from 4.1 eV to 3.9 eV with increasing Co sublayer thickness. The amplitude of the UV peak exceeds that of the peak centered at 3.7 eV of the pure Co film and depends relatively weakly on the composition of the MLS studied.

The characteristic feature in the Kerr ellipticity spectra is the shift of the zero crossing from 1.5 eV in the pure Co film to 3.7 eV in MLS with decreasing Co sublayer thickness and the formation of a positive peak around 3 eV. The prominent minimum of the Kerr ellipticity centered at 4.9 eV observed in the Co film is presumably shifted in position to the photon energy region $\hbar\omega > 5.5$ eV, inaccessible in the present experiment.

The optical properties of the MLS, in the form of the spectral dependences of the diagonal component of the effective optical conductivity tensor σ_{xx} , are shown for the real $\sigma_{xx}^{(1)}$ and imaginary part $\sigma_{xx}^{(2)}$ in Fig. 9,*a*, and Fig. 9,*b*, respectively. For clarity the spectra of only three samples are shown in the pictures; the other MLS spectra are located in between them. As is seen from the results, generally there is little difference in the absorptive part of the optical conductivity $\sigma_{xx}^{(1)}$ for all MLS studied. The magnitudes of the spectra roughly scale with the thickness of Co sublayers. The corresponding spectra of thick Co and Pt films prepared by the same technique are shown for comparison. It can be observed that the $\sigma_{xx}^{(1)}(\omega)$ curves for the MLS are not located between those for Co and Pt in the energy

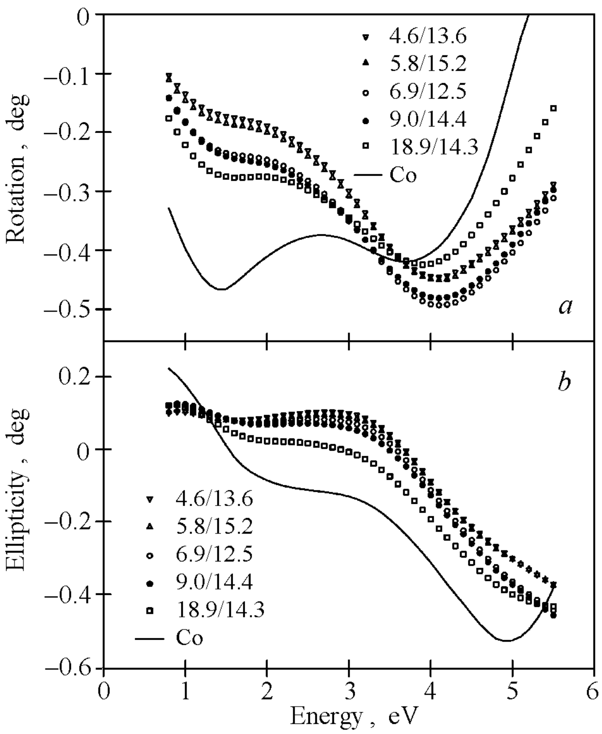

Fig. 8. Experimental polar Kerr rotation (*a*) and ellipticity (*b*) spectra of Co/Pt MLS and fcc Co film. Sublayer thicknesses marked in the pattern are given as t_{Co}(Å)/t_{Pt}(Å) [74].

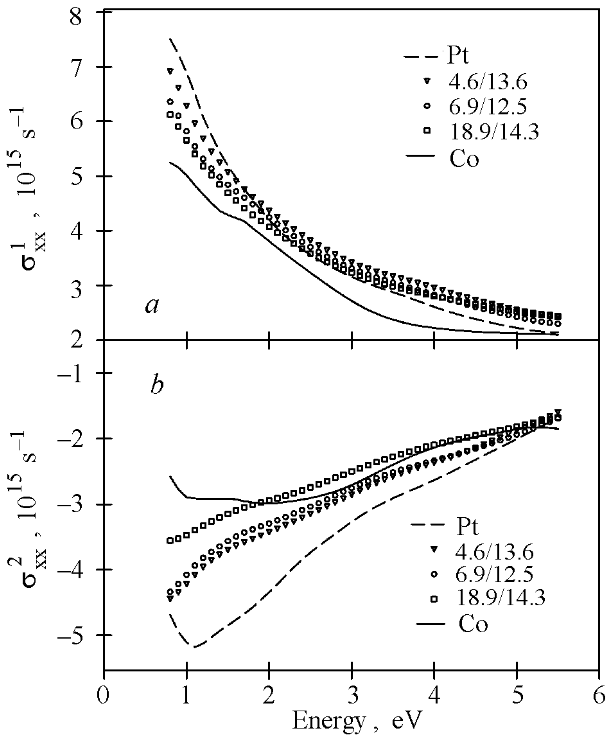

Fig. 9. The absorptive (*a*) and dispersive (*b*) parts of the diagonal components of the conductivity tensor for Co/Pt MLS and Co and Pt films, determined from the ellipsometric measurements [74].

range 2–5.5 eV. Several reasons can be considered for this difference. A common problem in metal optics is the great sensitivity of the optical constants on the state of the sample surface [60].

Another cause can be the fact that the optical properties of thick metal films are slightly different from the ones for MLS constituent sublayers [61]. In other words, for individual layer thicknesses of a few atomic monolayers the effective dielectric constants of the medium differ from the dielectric constants of the bulk or thick-film material. Besides, the response of an ultrathin medium to an electromagnetic wave is substantially influenced by the electronic interaction with adjacent layers.

The spectra of the dispersive part of the optical conductivity tensor $\sigma_{xx}^{(2)}$ are also weakly dependent on the MLS composition and lie in between the spectra for thick Co and Pt films.

To separate the contribution to the MOKE coming from the diagonal and off-diagonal conductivity tensor components the function $\Phi = 4\pi[\omega^2(\varepsilon_{xx} - 1)\sqrt{\varepsilon_{xx}}]^{-1}$ has been evaluated from the optical measurements. The real part of the function $\Phi^{(1)}$ is shown in Fig. 10,*a*. It has been found that for the compounds under consideration, the product of $\Phi^{(1)}$ and $\omega\sigma_{xy}^{(2)}$ gives the main contribution (> 80%) to the polar Kerr rotation spectra. It should be noted that this function is nearly flat over the investigated spectral region for all the MLS studied and depends weakly on their composition. On the contrary, the shape and amplitude of the $\Phi^{(1)}$ spectrum change significantly in the case of the Co film. As a consequence, the absorptive part of the off-diagonal component of the conductivity tensor, $\omega\sigma_{xy}^{(2)}$, presented in Fig. 10,*b* for the MLS studied is in its overall form unexpectedly similar to that of the polar Kerr rotation, whereas for the case of pure Co the shape of the polar Kerr rotation and $\omega\sigma_{xy}^{(2)}$ differ significantly. Inspection of these curves shows that the presence of Pt leads to strong enhancement of $\omega\sigma_{xy}^{(2)}$ in the UV range. The measured enhancement of the polar Kerr rotation is much smaller because of the corresponding increase of the diagonal part of σ (see Fig. 10,*a*).

Thus, it can be concluded that the peak observed in the IR part of the Co/Pt MLS polar Kerr rotation spectra can be related mainly to the MO activity of Co. On the contrary, the peak observed in the UV region is for pure Co connected rather with the peculiarities in the diagonal part of the conductivity tensor, while for Co/Pt multilayers it is governed by the off-diagonal component of σ and originates from the Co–Pt interaction at the MLS interface.

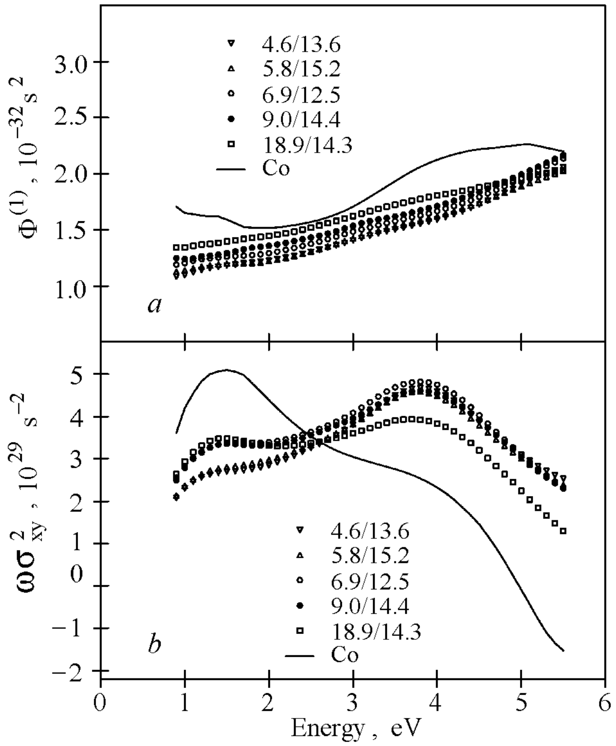

Fig. 10. The contribution to the Kerr rotation spectra from the diagonal part of the conductivity tensor (see text) (*a*) and the absorptive part of the off diagonal component $\omega\sigma_{xy}^{(2)}$ (*b*), determined from the ellipsometric and the complex polar Kerr angle measurements for Co/Pt MLS and Co film [74].

The multilayer MOKE spectra measured are qualitatively similar to the spectra which have been published for Co/Pt MLS prepared by different techniques and for random fcc Co–Pt alloys [21,22,24,62–64] and all exhibit similar MOKE enhancement in the UV region.

4.2. Theoretical results and discussions

In order to reproduce the electronic structure of the interlayer interface, band-structure calculations of some model ordered Co–Pt alloys and MLS with various layer thicknesses have been performed in Ref. 74. An *abcabc* stacking sequence of close-packed planes corresponding to the fcc-(111)-texture was assumed for all the MLS structures except for 1Co/1Pt for which the *ababab* stacking was also studied. No attempt has been made to optimize the interlayer spacing, which was taken to be corresponding to the ideal *c*/*a* ratio. Ordered $CoPt_3$ and the Co_3Pt alloys were calculated in the Cu_3Au crystal structure, while for the CoPt alloy the AuCu structure was used. For all the compounds the mean volume per atom was chosen to be equal to the average of the atomic volumes of pure fcc Pt and hcp Co, with the experimental lattice con-

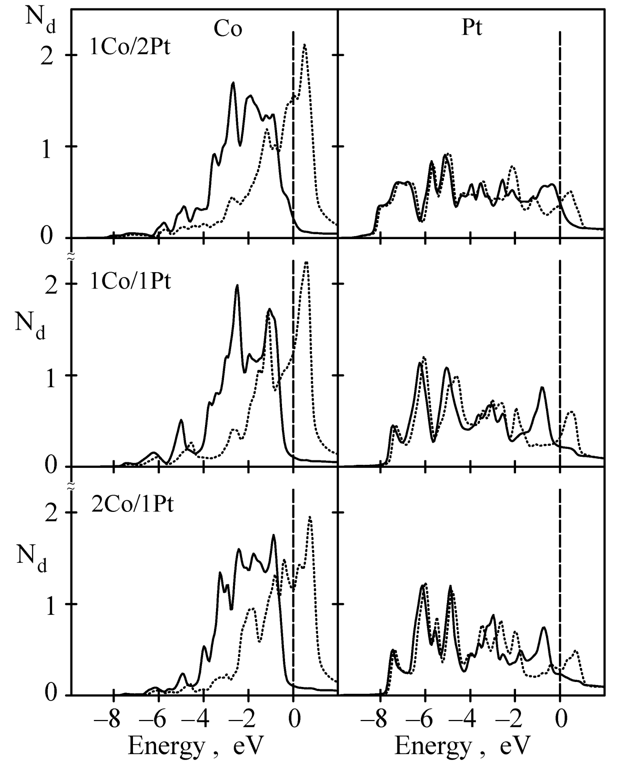

Fig. 11. Spin- and site-projected densities of *d* states (in units of state/(atom · spin · eV)) for Co and Pt in 1Co/1Pt, 2Co/1Pt, and 1Co/2Pt multilayers. Full and dotted lines correspond to majority and minority spin states, respectively, dashed line marks the Fermi energy [74].

stants. The radii of the Co and Pt atomic spheres were chosen equal to 1.46 Å.

The characteristic feature of the electronic structure of Co–Pt multilayers and alloys is the strong hybridization of Co 3*d* and Pt 5*d* states, the later being much more delocalized. Figure 11 shows the spin- and site-projected densities of the electronic states (DOS) for Co and Pt site in 2Co/1Pt, 1Co/1Pt, and 1Co/2Pt multilayers. The valence band width in the MLS is mainly governed by Pt *d*-*d* hybridization in the close-packed planes consisting of Pt atoms and varies moderately with an increase of the Pt sublayer thickness. The strong spin–orbit interaction in the Pt atomic sphere results in splitting of the $d_{3/2}$ and $d_{5/2}$ states, with the energy difference between their centers being ~ 1.5 eV. Inside the Co atomic sphere the effect of the spin–orbit coupling is much weaker than the effect of the effective magnetic field. The centers of both Pt $d_{3/2}$ and $d_{5/2}$ states lie at lower energies than the centers of the corresponding Co states. As a result of the Co $d -$Pt d hybridization, the electronic states at the bottom of the valence band are formed mainly by Pt states, while the states in the vicinity of the Fermi level (E_F) have predominantly Co *d* character with an admixture of Pt *d* states. The hybridization with the exchange-split Co *d* states leads to a strong polarization of the Pt *d* states near E_F . The resulting difference in occupation numbers for Pt states with the opposite spin projections gives rise to a comparatively large spin magnetic moment at the Pt site.

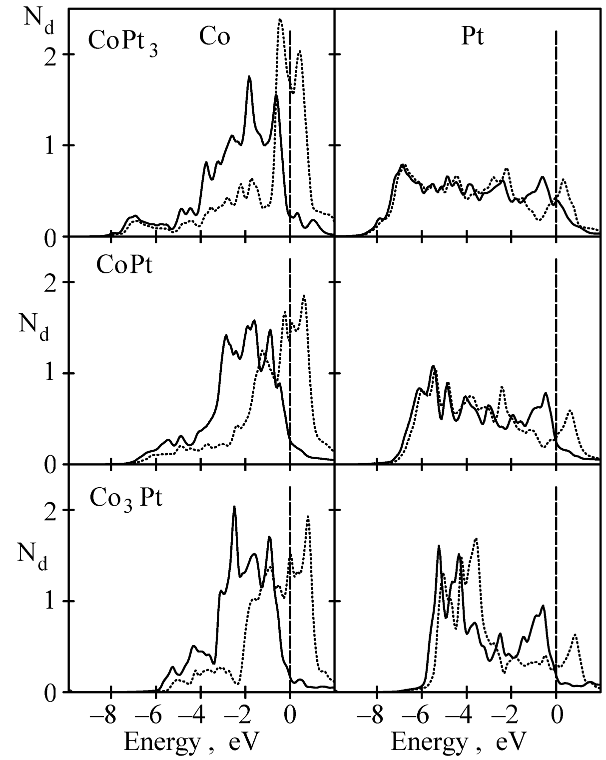

Fig. 12. Spin- and site-projected densities of *d* states (state/(atom · spin · eV)) for Co and Pt in Co_3Pt, CoPt, and $CoPt_3$ alloys. Full and dotted lines correspond to majority and minority spin states, respectively [74].

In the case of the 4Co/2Pt, 2Co/4Pt, and 1Co/5Pt MLS the DOS curves for Co and Pt sites at the interface are similar to the curves shown in Fig. 11. The DOS projected to a site in the interior of the sublayer is close to that of the corresponding bulk metal.

Calculated spin- and site-projected DOS curves for ordered Co_3Pt, CoPt, and $CoPt_3$ alloys are shown in Fig. 12. As compared to the Co/Pt MLS, the electronic structure of the alloys depends much more strongly on the alloy composition. Variation in the relative positions of the Co and Pt *d* bands affects the Co $d -$Pt d hybridization. The valence band width is larger in the Pt-rich alloys because of the larger number of Pt nearest neighbors surrounding the Pt site.

The calculated spin m_s and orbital m_l magnetic moments of the Co–Pt multilayers and alloys are summarized in Table 4. Both the spin and orbital moments at the Co site in the MLS are bigger than in bulk hcp Co with the experimental lattice constant. Nevertheless, from the comparison with the values of m_s and m_l calculated for either hcp or fcc Co with the lattice constant used for the MLS it follows that the moments' enhancement is mainly due to the lattice expansion. In contrast to the case of the MLS, the Co and Pt magnetic moments in the Co–Pt alloys decrease with an increase of Pt content.

Table 4

Calculated spin m_s and orbital m_l magnetic moments of the Co–Pt multilayers and alloys. Values in parentheses correspond to the atoms in the layer below the interface. Magnetic moments of hcp Co with the experimental lattice constant a = 2.507 Å is also given [74].

System	m_s (μ_B/atom)		m_l (μ_B/atom)	
	Co	Pt	Co	Pt
hcp Co (a = 2.507 Å)	1.559		0.079	
hcp Co	1.716		0.130	
fcc Co	1.731		0.115	
2Co/1Pt	1.776	0.183	0.098	0.019
1Co/1Pt	1.752	0.255	0.089	0.028
1Co/2Pt	1.880	0.207	0.099	0.022
4Co/2Pt	1.810 (1.738)	0.192	0.103 (0.104)	0.018
2Co/4Pt	1.765	0.154 (0.049)	0.095	0.016 (0.001)
1Co/5Pt	1.869	0.175 (0.058)	0.090	0.018 (0.006)
Co_3Pt	1.735	0.339	0.087	0.083
CoPt	1.681	0.321	0.090	0.048
$CoPt_3$	1.607	0.199	0.027	0.035

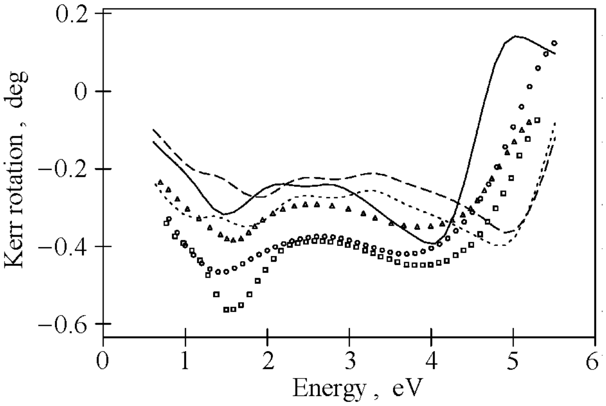

Fig. 13. Experimental and theoretical polar Kerr rotation spectra of Co [74]. The theoretical Kerr rotation spectra of fcc Co calculated using the experimental lattice constant and with the plasma frequency in the Drude term taken from the calculations (dashed curve), with $\hbar\omega_p$ = 5 eV (dotted curve), and calculated using the same lattice constant as for the Co/Pt MLS (solid curve). Experimental spectra are shown by circles (present work), squares (Ref. 68), and triangles (Ref. 21).

When studying the MO properties of the complex Co–Pt compounds it is natural to consider as a reference point the properties of pure Co [65–67]. The calculated energy dependence of the polar Kerr rotation angle of fcc Co with the lattice constant a = 3.539 Å corresponding to the experimental value for hcp Co is shown in Fig. 13 (dashed line). A comparison with the experimental data [21,68] shows that the calculations reproduce correctly the overall shape of the spectra but the UV peak is shifted by about 1 eV to higher energies. The discrepancy is similar to that observed in the theoretical Kerr rotation spectra of Ni [85,86] and is apparently due to a failure of LSDA to describe correctly the width and the spin splitting of d bands in ferromagnetic 3d metals. A better agreement with the experiments is obtained for the Kerr rotation calculated with a larger lattice constant a = 3.734 Å, which is equal to the value chosen for all model MLS studied (see solid line in Fig. 13). The increase of the lattice constant results in a narrowing of the d band and, consequently, in an energy scaling of the calculated spectrum. The same tendency has been observed not only for pure Co but also for Co–Pt alloys and multilayers.

Although the lattice expansion removes the shift of the peaks, the calculated amplitude of the peak at 2 eV remains smaller than the experimental one. To elucidate the reason for the discrepancy in amplitudes, the dependence of the MOKE spectra on the intraband part of the conductivity tensor was examined [74]. It was found that in the case of pure Co the Kerr rotation is rather sensitive to the values of γ and ω_p^2 for energies up to 5 eV. Variation of the values changes the amplitude and the position of the UV peak as well as of the peak at 2 eV. The sensitive effect of the Drude term on the UV peak is due to the interband contribution to σ_{xx} being small in this energy range. Thus, although the absolute values of the intraband conductivity are small, its relative contribution is significant. The calculated plasma frequency of hcp Co with the experimental lattice constant was found to be 7.2 eV, while the experimental value for the hcp Co single crystal is ~ 5 eV [57]. Such a discrepancy is in agreement with the previous observation [69] that the calculated values of ω_p are, as a rule, 20–50% higher than the experimental values. The polar Kerr rotation calculated with $\hbar\omega_p = 5$ eV is shown by the dotted line in Fig. 13. The use of the smaller value of ω_p leads to a better agreement with the experiment. Nevertheless, it was not possible to achieve close agreement with experiment in the IR range by varying the Drude constants over reasonably wide limits. It has been found that for Co–Pt multilayers and alloys the dependence of MOKE on the intraband contribution is much weaker, and in the following we use the calculated values of ω_p to evaluate the intraband conductivity.

Theoretical results for the absorptive part of the conductivity tensor $\sigma_{xx}^{(1)}$ for fcc Co, Pt, and some model Co–Pt multilayers and alloys are shown in Fig. 14. For energies higher than 1.5 eV the $\sigma_{xx}^{(1)}$ curves of the MLS and the alloys have similar energy dependence and fall within the range between the $\sigma_{xx}^{(1)}$ curves of bulk Co and Pt, the conductivity of Co-rich MLS being closer to $\sigma_{xx}^{(1)}$ of Co.

The calculated dependence of $\sigma_{xx}^{(1)}$ on Co contents correlates well with the data obtained from the ellipsometric measurements of Co/Pt multilayers with different Co layer thickness. Although the calculations give $\sigma_{xx}^{(1)}$ of a higher amplitude than the experimental data, the theoretical results reproduce the changes of $\sigma_{xx}^{(1)}$ with the variation of the Co sublayer thickness. Of all the MLS considered, only $\sigma_{xx}^{(1)}$ of 4Co/2Pt has a subtle feature at ~ 5 eV corresponding to bulk Co. The fact that the σ_{xx} curves of the Co–Pt compounds of different composition and of different chemical ordering have similar shapes with no pronounced features suggests

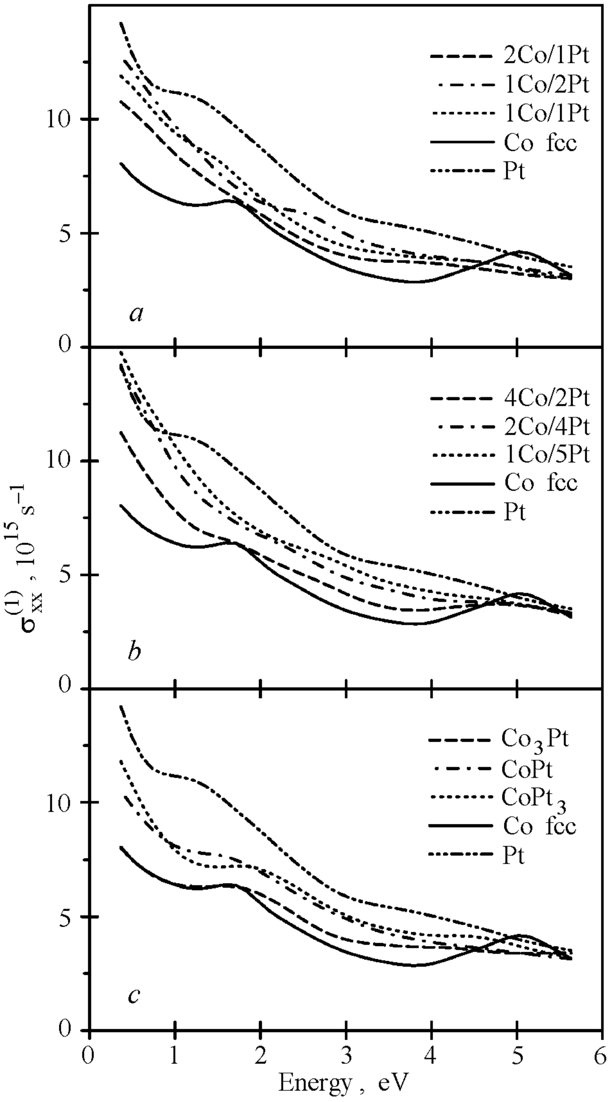

Fig. 14. Theoretical $\sigma_{xx}^{(1)}$ spectra of the Co–Pt multilayers (*a*, *b*) and alloys (*c*) [74].

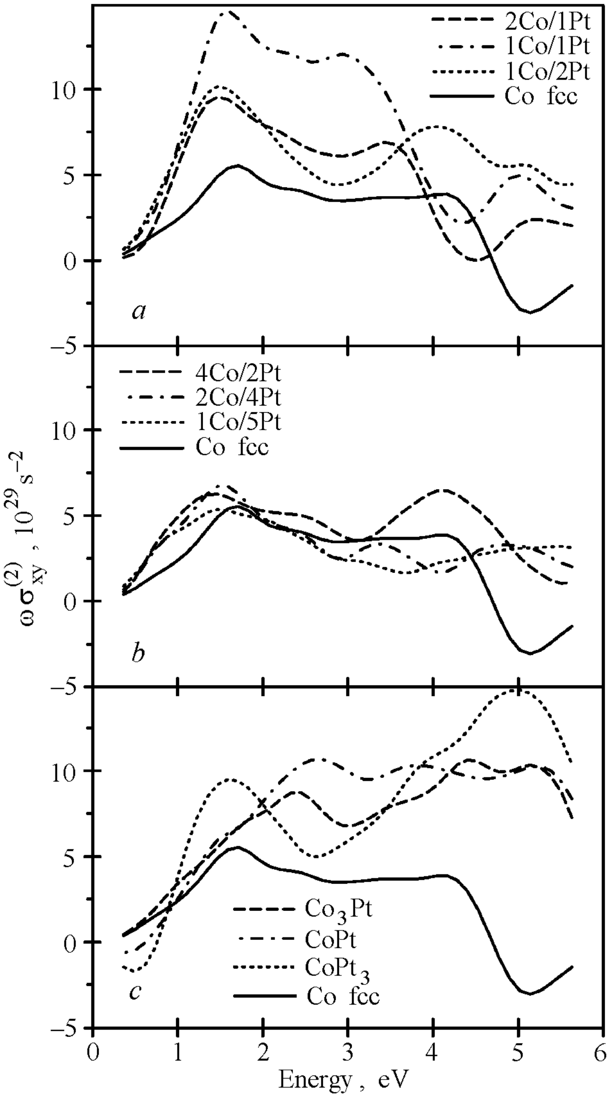

Fig. 15. Theoretical $\omega\sigma_{xy}^{(2)}$ spectra of the Co–Pt multilayers (*a*, *b*) and alloys (*c*) [74].

that, unlike the case of bulk Co, the two-peak structure of the polar Kerr rotation spectra of Co/Pt MLS comes from the energy dependence of the off-diagonal part of the conductivity tensor.

The results of the calculations of the absorptive part of $\omega\sigma_{xy}$ of Co–Pt MLS and alloys are shown in Fig. 15. The calculated $\omega\sigma_{xy}^{(2)}$ of pure fcc Co is shown for reference by the solid curve in all figures. All the compounds can be divided into three distinct groups according to differences between their $\omega\sigma_{xy}^{(2)}$ and that of pure Co. The first group consists of 2Co/1Pt, 1Co/1Pt, and 1Co/2Pt multilayers (Fig. 15,*a*), which have no more than two consecutive planes of equivalent atoms. For these MLS the energy dependence of $\omega\sigma_{xy}^{(2)}$ varies strongly with MLS composition, with the absolute values of $\omega\sigma_{xy}^{(2)}$ being significantly larger compared to Co. In the case of 2Co/1Pt and 1Co/1Pt the curves have similar shape, but $\omega\sigma_{xy}^{(2)}$ of the latter is ~ 1.5 times greater. The position of the peak at ~ 1.5 eV is not altered compared to Co, while the feature at ~ 3.5 eV is shifted to lower energies by 1 eV, and an additional peak appears around 5.5 eV. There are two maxima in $\omega\sigma_{xy}^{(2)}$ of 1Co/2Pt, which lies at approximately the same energies as in Co, but their intensities are 2 times higher.

The situation is quite different in the case of multilayers with greater sublayer thickness (Fig. 15,*b*). Some increase in $\omega\sigma_{xy}^{(2)}$ is observed only for 4Co/2Pt MLS, with the shape of the curve being similar to that of Co. The $\omega\sigma_{xy}^{(2)}$ of 2Co/4Pt and 1Co/5Pt lies very close to each other and are reduced compared to $\omega\sigma_{xy}^{(2)}$ of Co in the energy range of 2.5–4.5 eV. It should be noted that the last two MLS have Co and Pt sublayer thicknesses which are close to those of experimentally studied films.

Our results for 2Co/1Pt and 2Co/4Pt multilayers are somewhat different from those given in Ref. 70. The discrepancy is partially due to slightly different values of the structural parameters. Nevertheless, calculations performed with the same parameters as in Ref. 70 show that the difference between the two calculations disappears only when the combined corrections to the LMTO Hamiltonian and overlap matrices are not included. This is not surprising, because even with the current-density matrix elements computed accurately, the neglect of the combined corrections terms affect the calculated conductivity tensor via changes in band energies.

The calculated $\omega\sigma_{xy}^{(2)}$ for model alloys are shown in Fig. 15,*c*. The common feature of all the spectra is a strong enhancement of $\omega\sigma_{xy}^{(2)}$ in the energy range 4–6 eV. Of the three curves, $\omega\sigma_{xy}^{(2)}$ for $CoPt_3$ is of a different shape, with two distinct maxima at ~ 1.5 eV and 5 eV, the amplitude of the latter being more than three times greater than the feature in the spectrum of Co at ~ 4.5 eV.

It has been shown [84,86] that in pure 3*d* metals the off-diagonal conductivity is proportional to the strength of the spin–orbit coupling. In transition metal compounds, however, the dependence of the MO properties on the spin–orbit coupling and effective magnetization of constituent atoms is far more complicated [71]. To understand this better, model calculations were performed with the spin–orbit coupling set to zero on either the Co or the Pt site. It was found that «switching off» the spin–orbit coupling inside the Co atomic sphere affects the off-diagonal part of the conductivity tensor only slightly, while neglecting the spin–orbit interaction in the Pt sphere results in a strong decrease of $\omega\sigma_{xy}^{(2)}$. These results are in qualitative agreement with those obtained by the authors of Ref. 72, who also observed a strong dependence of $\omega\sigma_{xy}^{(2)}$ on the value of the spin–orbit coupling on the Pt site. We also investigated the effect of excluding the matrix elements of the effective magnetic field at the Co and Pt sites from the LMTO Hamiltonian. When the matrix elements on the Co sphere are zero, the off-diagonal part of the conductivity decreases drastically. At the same time, «switching off» the effective magnetic field at the Pt site produces a negligible effect at the $\omega\sigma_{xy}^{(2)}$ spectra. Thus, a strong spin–orbit coupling at only one of the inequivalent atomic sites and a large value of the effective magnetization at the other can be sufficient for alloys to manifest strong MO activity.

In addition, it has been found that the dominant contribution to the $\omega\sigma_{xy}^{(2)}$ spectra in the energy range of interest (1–6 eV) comes from transitions to unoccupied states lying in a rather narrow energy interval of ~ 1 eV just above the E_F . At the same time, these transitions give a relatively small contribution to the diagonal part of the optical conductivity. As has been mentioned above, the electronic states in the vicinity of the E_F are formed by strongly hybridized Co *d* and Pt *d* states.

It is worthwhile to note that in the case of transition-metal compounds, the wave functions of the initial and final states involved in an optical transition are delocalized. Consequently, it is difficult, if possible at all, to separate the contributions of any intra- or interatomic transitions to the MO spectra. The assumption that the enhanced MO effects in Co–Pt compounds are due to Co *d* – Pt *d* hybridization allows one to explain the relatively small (as compared to Co–Pt alloys) magnitude of

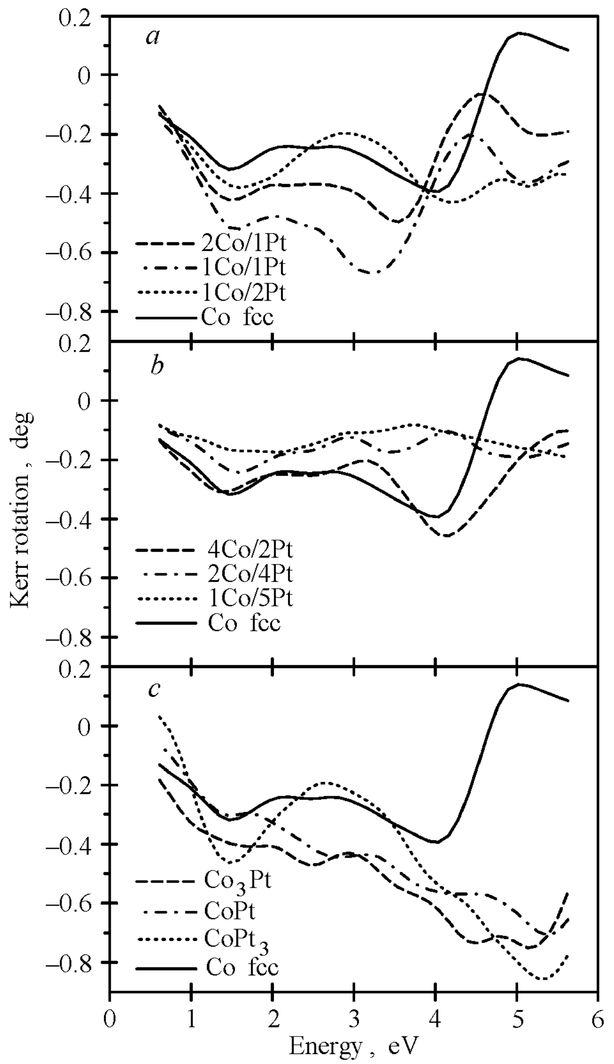

Fig. 16. Theoretical polar Kerr rotation spectra of the Co–Pt multilayers (*a*, *b*) and alloys (*c*) [74].

the calculated $\omega\sigma_{xy}^{(2)}$ in 2Co/4Pt and 1Co/5Pt multilayers. In these MLS there are Pt layers consisting of atoms which have Co atoms among neither the first nor the second nearest neighbors and the contribution of these layers to $\omega\sigma_{xy}^{(2)}$ is small. However, switching off the spin–orbit interaction for these atoms leads to a rather strong variation of the spectrum. Neglecting the spin–orbit coupling for Pt atoms at the Co–Pt interface only leads to relatively pronounced changes, but the magnitude of $\omega\sigma_{xy}^{(2)}$ remains considerably higher than the magnitude of $\omega\sigma_{xy}^{(2)}$ calculated with the spin–orbit interaction at all Pt atoms set to zero.

Calculated polar Kerr rotation spectra are shown in Fig. 16. From a comparison with the experimental MOKE spectra of the Co/Pt MLS shown in Fig. 8 it can be seen that the calculated spectra of MLS do not satisfactory reproduce the experimental data. The magnitude of the calculated MOKE spectra of 2Co/4Pt and 1Co/5Pt MLS (Fig. 16,*a*) in the energy range 3–5 eV is significantly smaller than that of pure Co, while an enhancement of the rotation angle of MLS vs. pure Co is observed in the experiment. The enhancement is indeed found for Co/Pt MLS with smaller sublayer thickness (Fig. 16,*b*), but in contrast to the experimental data the peak is shifted to lower energy with respect to its position in Co. Surprisingly, better agreement with the experimentally observed MOKE spectra is observed in the case of Co–Pt alloys (Fig. 16,*c*). The calculated spectra reproduce fairly well both the increase of magnitude and the shift of the UV peak to higher energies.

The discrepancy between the experimental Kerr rotation spectra of Co/Pt MLS obtained in the present work and the calculated spectra of the model Co/Pt multilayers may be due to inadequacy of the adopted structure model of the MLS with the sharp interlayer interface. The observed energy dependence of the MOKE spectra of the MLS and their variation with the Co sublayer thickness may be explained by the reasonable assumption that a Co–Pt alloy is formed at the interface.

It is interesting to compare the results of our calculations with the recently published polar Kerr rotation spectra of an artificial Co_3Pt alloy film [73]. X-ray diffraction data show that after annealing at 650 K the alloy consists of alternating sequence of close-packed Co and CoPt planes with an hcp-like stacking. Because of the well-defined order along the crystallographic *c* direction, the structure of the alloy is rather close to that of the model 1Co/1Pt multilayer. Nevertheless, because of the different compositions of the two compounds, the direct comparison of the experimental and calculated MOKE spectra should be made with care. Calculated MOKE spectra of 1Co/1Pt multilayers with *ababab* and *abcabc* layer sequences are shown in Fig. 17 together with the experimental spectra. Except in the IR range, the calculated spectra are similar, with slightly different amplitudes. Both theoretical spectra have a peak at ~ 3 eV which is clearly seen on the experimental curve. A 5 eV feature in the experimental spectrum is also reproduced by the calculations but the corresponding peaks are shifted slightly to higher energies. The shift may be caused by the difference of the experimental and theoretical lattice constants. After annealing at 950 K the Co_3Pt alloy film has been shown to consist of a chemically disordered fcc phase. The modification of atomic arrangement and chemical short range order causes significant

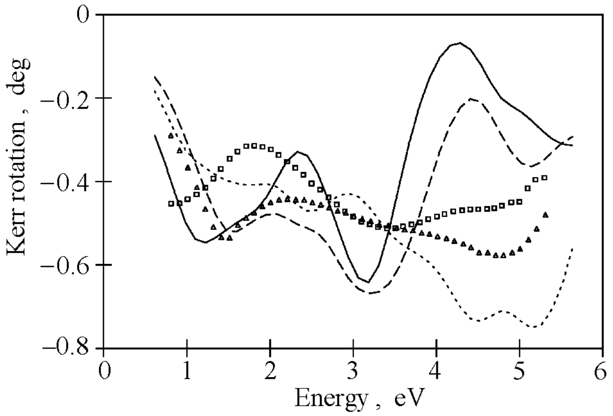

Fig. 17. Theoretical polar Kerr rotation spectra of 1Co/1Pt multilayers with *ababab* (solid line) and *abcabc* (dashed line) stacking. Calculated spectrum of Co_3Pt alloy is shown by the dotted line. Experimental spectra for ordered hexagonal Co_3Pt phase (squares) and chemically disordered fcc phase (triangles) are taken from Ref. 73 [74].

changes of the observed MOKE spectra. The 3 eV peak disappears, while the amplitude of the spectra in the UV range increases and the 5 eV feature transforms into a peak. Similar changes are readily seen when comparing the calculated MOKE spectra of 1Co/1Pt multilayers with the calculated spectrum of the Co_3Pt alloy.

In conclusion it should be pointed out that the Kerr rotation of Co/Pt MLS is governed mainly by the off-diagonal part of the conductivity tensor. The infrared part of the spectrum originates from the MO activity of the Co layers themselves, and it scales with the Co content. On the other hand, the peak in the UV region is due to the hybridization of strongly spin-polarized Co *d* states with spin–orbit-split Pt *d* states, and its magnitude depends weakly on the MLS composition. It has been demonstrated that the chemical and structural ordering is accompanied by substantial electronic structure changes and result in a drastic MOKE spectra modification.

It should be noted that the *ab initio* description of the MOKE spectra for model Co/Pt multilayers performed under the assumption of a sharp, ideal interface is not adequate for the detailed explanation of the experimentally observed spectra. Simultaneously, in the case of model Co–Pt alloys the calculations properly reflect the main features of the spectra observed experimentally. Thus it can be concluded that in the real multilayer structures the limited interdiffusion region at the interface and its structure and chemical composition play a major role in the formation of the MO spectra of the Co/Pt MLS.

4.3. The effect of interfacial alloying on the magneto-optical spectra in Co/Pt multilayers

To examine the consequences of interfacial intermixing for Co/Pt MLS MOKE spectra and their relation to the chemical nature of the interface, special model supercells of the multilayered structures with alloyed interfaces and fcc (111) texture were constructed in Ref. 75. The same lattice constant and space group as for the idealized model were used in the calculations. As an interface between the neighboring Co and Pt layers, one or two Co–Pt mixed atomic planes were introduced. Three types of multilayered structures were considered: in the form of single-layer Pt-rich Co_1Pt_3 and Co-rich Co_3Pt_1 ordered interfacial planar alloys and also in the form of a double alloy layer Co_3Pt_1/Co_1Pt_3 composed of consecutive single layers of different composition. The calculated spectra for Co/Pt MLS structures in which Co and Pt atomic planes are separated by a single interfacial alloy layer of different compositions are shown in Fig. 18. As can be seen, the presence of the interfacial alloy plane does not appreciably alter the spectra in the IR range, while significant enhancement of the Kerr rotation amplitude in the UV spectral range is clearly seen.

The enhancement of the Kerr rotation in the UV range brings the spectra to better agreement with the experiment. However, the magnitudes of the calculated spectra are still significantly smaller than those of the experimental ones. In the «real» Co/Pt systems the intermixing probably extends to

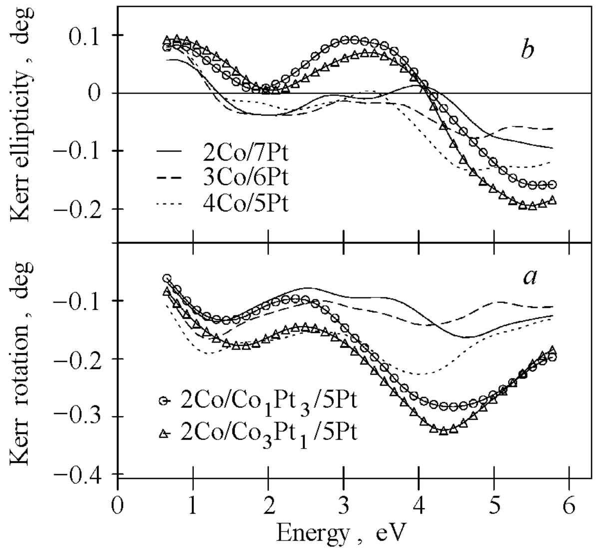

Fig. 18. Calculated polar Kerr rotation (*a*) and ellipticity (*b*) spectra for the model of Co/Pt multilayers with sharp interfaces (lines) and with single-layer interfacial alloys (symbols) [75].

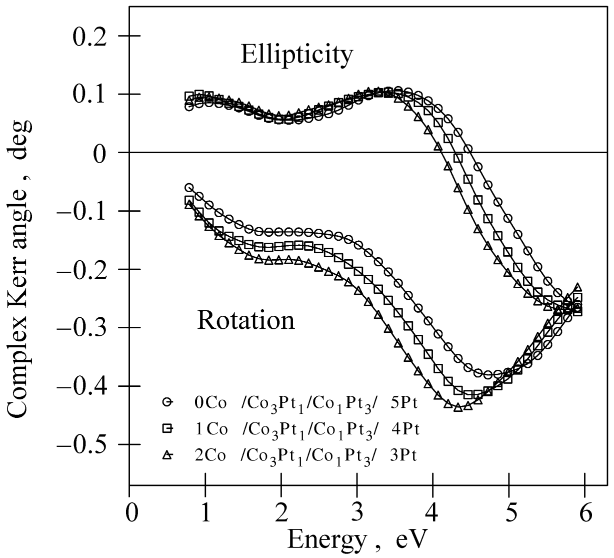

Fig. 19. Calculated polar Kerr rotation (*a*) and ellipticity (*b*) spectra for the model of Co/Pt multilayers with double-layer interfacial alloy [75].

more than one atomic plane, with the composition changing gradually. In Fig. 19 the results of the calculations for the Co/Pt MLS model structure composed of double interfacial Co_3Pt_1/Co_1Pt_3 alloy atomic planes are presented. From Figs. 18 and 19 it can be seen that in the IR region the amplitudes of the spectra depend weakly on the interfacial layer thickness and composition, whereas in the UV range the amplitudes increase by about 50% as compared to the spectra with a single interfacial alloy layer. Alloying at the Co/Pt MLS interfaces leads to an increase of the volume in which the strong $3d$–$5d$ hybridization occurs and, consequently, the contribution of these hybridized states to the MO spectra increases compared to the ideal MLS models. Another effect of interfacial alloy formation is stronger spin polarization of the whole Pt spacer. The averaged magnetic moment per Pt atom calculated for the structures with alloyed interface increases by up to 90% compared to that calculated for the ideal MLS model. It was found that the contribution to the MLS spectra coming from the interfacial alloy region and polarized Pt atomic planes controls the shape and magnitude of the spectra in the UV energy range.

In conclusion, the results obtained clearly illustrate the crucial role of the interface structure on the magneto-optical spectra of the Co/Pt multilayers. It is shown that the main peculiarities and the tendencies in the modification of the MLS spectra with the variation of the Co sublayer thickness are adequately reproduced when alloying, limited to two atomic planes, is taken into account. The very good agreement between the calculated and measured MOKE spectra demonstrates the validity of the adopted model and approach.

5. Magneto-optical properties of Co/Cu multilayers

In the pioneering study of Katayama et al. [76] it was shown that the Kerr rotation in Fe/Cu bilayers can be enhanced at the absorption edge energy of Cu. Since then, several investigations of MOKE spectra of Fe,Co/noble-metal bilayers and multilayers have been done [77–81]. The observed features of the MOKE spectra were interpreted as mainly related to the plasma edge in the noble metal and also to magneto-optically active transitions in the noble metal as a consequence of the spin polarization of the noble metal by the proximity of magnetic layers at the interface.

In Ref. 82 the complex MOKE spectra and optical properties — refractive index n and extinction coefficient k — were measured in a wide spectral range for a set of Co/Cu MLS structures. For the study the following set of Co/Cu MLS was prepared: 14.9 Å Co/10.1 Å Cu, 15.2 Å Co/15.2 Å Cu, 15.1 Å Co/21.7 Å Cu, and 22.3 Å Co/23.7 Å Cu, all with the same number of repetitions of the Co/Cu bilayer being equal to 40. The MLS have been deposited by the face-to-face dc sputtering system described in Ref. 83. All of the samples were deposited on a water-cooled glass substrate. The argon pressure during the deposition was about 60 mPa, and the deposition rate was about 0.5 Å/s. The chemical composition of the films was determined by x-ray fluorescence analysis with an EDX system from the peak intensities of the characteristic fluorescence radiation. The crystal structure was examined by low- and high-angle x-ray diffraction (XRD) using Co-$K(\alpha)$ radiation. The layered structure was confirmed by low angle XRD. The modulation period was deduced from the position of the Bragg peaks. From the high-angle XRD the pronounced (111) texture was inferred.

In Fig. 20 the measured polar Kerr rotation θ_K and ellipticity η_K spectra of the Co/Cu MLS studied are shown. The measured spectra of θ_K and η_K of a thick (~ 2000 Å) fcc Co film are included for comparison.

The essential points of the experimental MOKE results can be summarized as follows:

i) The θ_K spectra of the Co/Cu MLS exhibit two peak structure and are strongly reduced compared to the pure Co thick film.

ii) The broad negative θ_K peak appearing in the UV energy region has an amplitude which is ap-

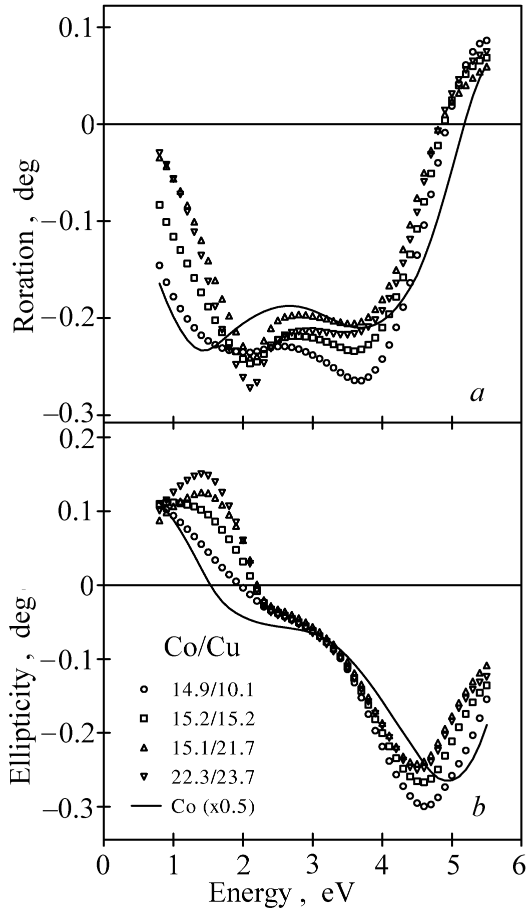

Fig. 20. Experimental polar Kerr rotation (*a*) and ellipticity (*b*) of Co/Cu MLS and thick fcc Co film (multiplied by a factor of 0.5). Co and Cu sublayer thicknesses are given in legend in units of Å [82].

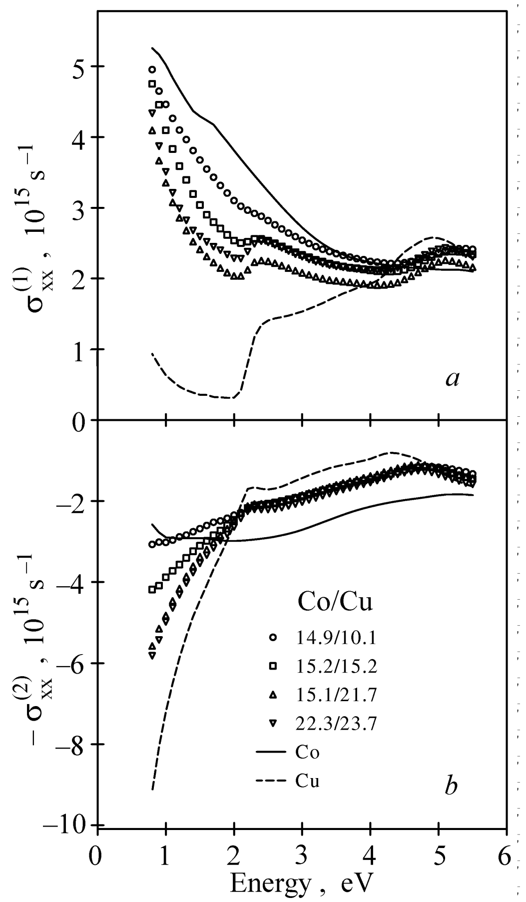

Fig. 21. The absorptive (*a*) and dispersive (*b*) parts of the conductivity tensor of Co/Cu MLS and thick fcc Co and Cu films determined from the ellipsometric measurements [82].

proximately proportional to the MLS Co content. The energy position of this peak remains the same as for the Co thick film.

iii) The θ_K spectra in Co/Cu MLS exhibit a peak at $\hbar\omega \sim 2.1$ eV not observed in the pure Co film. The amplitude and width of this peak are directly connected with the Cu sublayer thickness. For the MLS with the thinnest Cu sublayer the peak transforms into a broad shallow minimum located between ~ 1.5 eV and ~ 2.1 eV, the former energy corresponding to the θ_K peak position of the Co thick film.

iv) As the amount of Co in the MLS decreases, the spectra generally scale down, while there is an increase in the prominence of the θ_K peak located at the energy of ~ 2.1 eV.

v) At the energies above ~ 2.1 eV the Kerr ellipticity spectra are very similar. The UV peak position shifts to lower energy compared to the Co thick film, and its amplitude scales with the amount of Co. In the energy range 0.8–2.1 eV a strong dependence of the spectra on the MLS composition is seen.

The measured optical properties of the MLS as well as of thick fcc Co and Cu films, prepared by the same technique, are shown in the form of the spectral dependences of the absorptive ($\sigma_{xx}^{(1)}$) and dispersive ($\sigma_{xx}^{(2)}$) parts of the diagonal component of the optical conductivity tensor in Figs. 21,*a* and 21,*b*, respectively. The well-known prominent feature at the energy ~ 2.1 eV in the Cu optical conductivity tensor, where there is a superposition of the Drude-like intraband transitions and the interband transition edge, is clearly observed.

As can be seen from Fig. 21,*a*, the $\sigma_{xx}^{(1)}$ spectra for the MLS studied lie between the spectra of pure Co and Cu films. These spectra have two features, a shoulder at an energy of ~ 2.1 eV and a broad maximum at about 5 eV. The feature at ~ 2.1 eV is related to the Cu plasma-edge resonance absorption, and its prominence increases with the Cu content. For all Co/Cu MLS studied the $\sigma_{xx}^{(1)}$ spectra have similar shape, and their magnitude in the IR range scales with the amount of Co. This can easily be understood by taking into account weak absorption of Cu metal in the energy region.

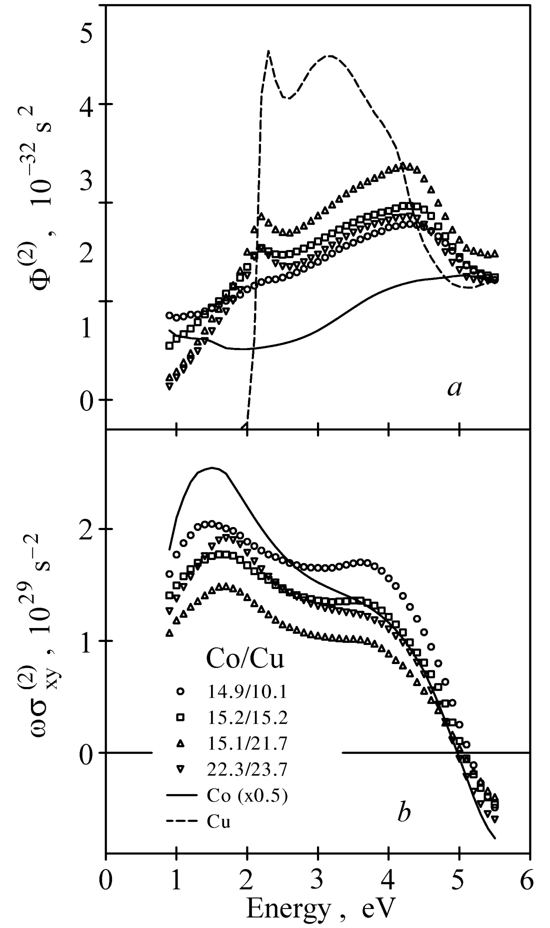

Fig. 22. The contribution to the Kerr rotation spectra from the diagonal part of the conductivity tensor (see text) (*a*) and the $\omega\sigma_{xy}^{(2)}$ of Co/Cu MLS and the thick fcc Co film determined from the ellipsometric and the MOKE measurements (*b*) [82]. The $\omega\sigma_{xy}^{(2)}$ of Co is multiplied by a factor of 0.5.

The MOKE depends on the diagonal part of the optical conductivity through the denominator of Eq. (2). To separate the contribution to the MOKE coming from the diagonal and off-diagonal components of the optical conductivity tensor the function $\Phi(\omega)$ has been evaluated from the optical measurements:

$$\Phi(\omega) = \Phi^{(1)}(\omega) + i\Phi^{(2)}(\omega) = \frac{1}{\omega\sigma_{xx}\sqrt{1 + i(4\pi/\omega)\,\sigma_{xx}}} . \tag{16}$$

It has been found that for the compounds under consideration the imaginary part of the function multiplied by $\omega\sigma_{xy}^{(2)}$ gives the main contribution into the polar Kerr rotation spectra. (Here and in the following $\sigma_{xy}^{(2)}$ stands for the absorptive part of the off-diagonal conductivity component.) For the Co/Cu MLS the function $\Phi^{(2)}(\omega)$ exhibits a two-peak structure (see Fig. 22,*a*), a sharp peak at the same energy ~ 2.1 eV as in the Kerr rotation spectra and a broader one at an energy around 4.5 eV. Thus, it can be clearly seen that diagonal part of the optical conductivity tensor significantly influences the shape of the MOKE spectra.

In Fig. 22,*b* the $\omega\sigma_{xy}^{(2)}$ spectra of the Co/Cu MLS are shown. The shape of the curves for all MLS is qualitatively similar to the shape of the $\omega\sigma_{xy}^{(2)}$ determined for the Co thick film. Inspection of the curves shows that the magnitude of the $\omega\sigma_{xy}^{(2)}$ spectra in the UV spectral region scales with the amount of Co. However, this is not true for the IR spectral region: in particular, the position of the low energy peak shifts from that for the fcc Co film and depends on the MLS composition. The changes can be explained by a modification of the electronic states involved in the optical transitions due to the presence of the Co/Cu interface.

It can be concluded that the IR peak observed in the polar Kerr rotation spectra is mainly determined by the corresponding feature in the diagonal part of the conductivity tensor. The position of the θ_K peak observed in the UV spectral region coincides with the position of the peak in the $\omega\sigma_{xy}^{(2)}$ spectra, but its shape is to a great extent affected by the spectral form of σ_{xx} , just as in the case of pure Co.

To clarify the microscopic origin of the magneto-optical properties of the Co/Cu multilayers, we have performed self-consistent local-spin-density calculations of the electronic structure of some model Co/Cu structures by means of the spin-polarized fully relativistic (SPR) LMTO method.

Since the experimentally investigated MLS have pronounced fcc-(111)-texture, in the *ab initio* calculations we constructed a number of nCo/mCu model MLS periodic along the [111] direction and consisting of close-packed n Co and m Cu planes with an *abc* stacking sequence. All the structures possess D_{3d}^3 symmetry. The lattice constant ($a = 3.574$ Å) was chosen as an average of those of the fcc Co and Cu metals. No attempt has been made to optimize the interlayer spacing, which was taken to be constant corresponding to the ideal c/a ratio.

The spin- and l-projected density of the electronic states for Co and Cu atoms in the representative 6Co/6Cu multilayer are shown in Fig. 23 for the sites at the interface and in Fig. 24 for the sites located in the middle of the appropriate sublayer. The densities of d-states of bulk fcc Co and Cu are shown at the top of Fig. 24 for comparison. As could be anticipated, the density of Co and Cu d states of the interior atoms are similar to those of bulk metals. At the same time, the Co and Cu states at the interfacial sites are strongly hybridized. It is

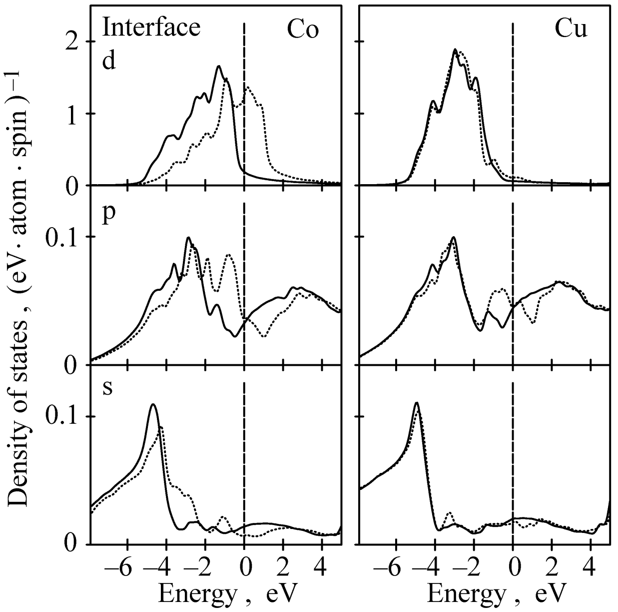

Fig. 23. Spin- and l-projected density of states at Co and Cu sites (state/(eV·atom·spin)) at the interface in 6Co/6Cu multilayer. Full and dotted lines correspond to majority and minority spin states, respectively. The Fermi level is denoted by vertical dashed line [82].

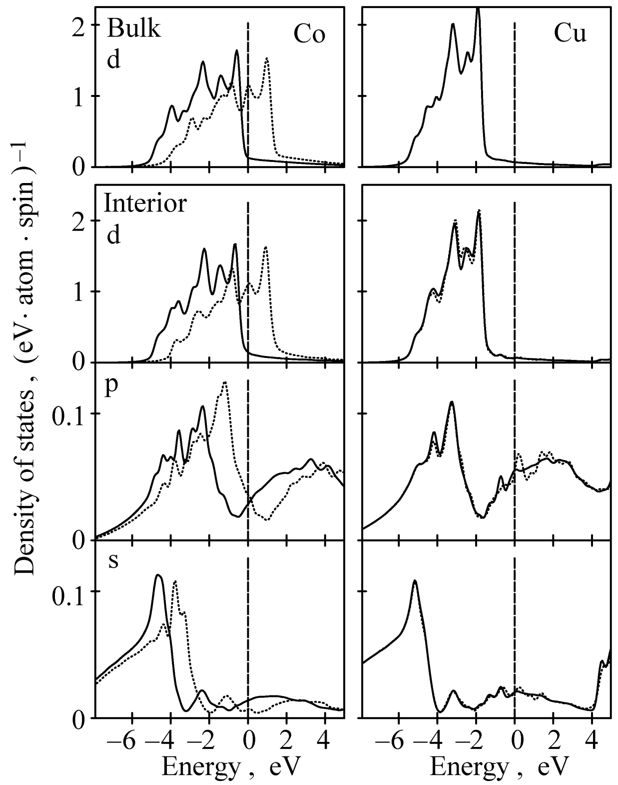

Fig. 24. Spin- and l-projected density of states at Co and Cu sites (state/(eV·atom·spin)) located in the middle of the corresponding sublayer in 6Co/6Cu multilayer. The density of d-states of bulk fcc Co and Cu is also shown. Full and dotted lines correspond to majority and minority spin states, respectively. The Fermi level is denoted by vertical dashed line [82].

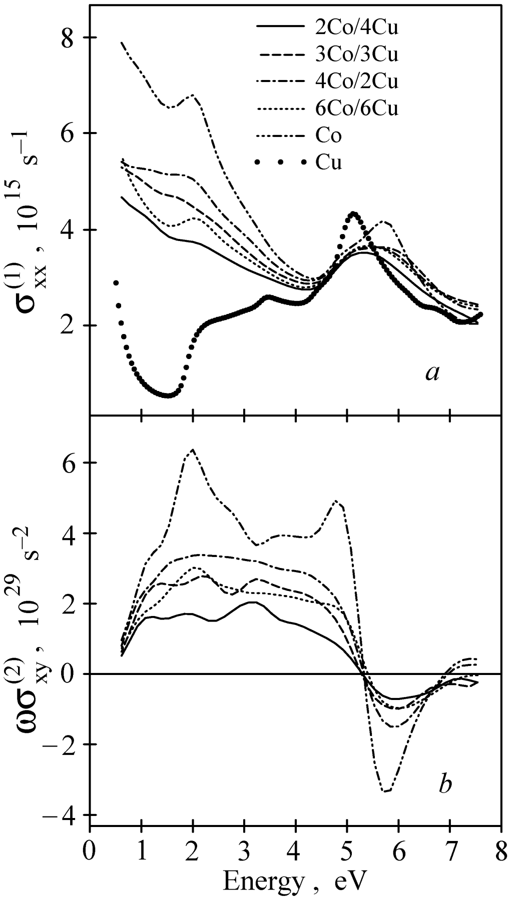

Fig. 25. Calculated $\sigma^{(1)}_{xx}$ (a) and $\omega\sigma^{(2)}_{xy}$ (b) spectra of the model Co/Cu multilayers [82].

interesting to note that the Cu states at the interface are considerably spin-polarized due to the hybridization with Co states. It was found that the resulting Cu sp and d spin magnetic moments are of opposite sign and almost compensate each other.

To show the main trends in the formation of the optical and magneto-optical spectra of the Co/Cu MLS, the conductivity tensor of 2Co/4Cu, 3Co/3Cu, 6Co/6Cu, and 4Co/2Cu model multilayers was calculated. The calculated $\sigma^{(1)}_{xx}$ spectra are shown in Fig. 25,a. All the spectra except that of Cu were broadened with a Lorentzian of width 1.2 eV to simulate the finite electron lifetime effects. For Cu spectrum a Lorentzian of width 0.4 eV was used. To take into account the intraband contribution the phenomenological Drude term was also added to the diagonal components of σ. In accordance with the experimental data the curves lie very close to each other at energies higher than ~ 4 eV. In the visible and IR spectral regions a noticeable increase of the absorption with increasing Co content can be seen. An interesting feature of these spectra is the minimum at the energy $\hbar\omega \sim 1.5$ eV, which corresponds to a minimum of the interband absorption in pure Cu. From the comparison of $\sigma_{xx}^{(1)}$ of 3Co/3Cu and 6Co/6Cu it can be seen that this peculiarity is enhanced as the number of adjacent Cu layers increases. An analysis of the partial density of states shows that such a behavior of $\sigma_{xx}^{(1)}$ can be explained by the energy location of the Co and Cu *d* states (see Figs. 23 and 24). The dominant interband contribution to the $\sigma_{xx}^{(1)}$ spectra at photon energies lower than ~ 4 eV comes from transitions involving the Co and Cu *d* states. As in the pure Cu metal, the Cu *d* states in the MLS are located $\sim$ 1.5 eV below the Fermi level and, consequently, give no contribution to $\sigma_{xx}^{(1)}$ at lower photon energy. On the contrary, optical transitions to/from the Co *d* states are possible at arbitrary energy, because the minority spin Co *d* states are only partially filled. As a result of a superposition of the absorption in Co and Cu sublayers, the magnitude of the $\sigma_{xx}^{(1)}$ spectra of the Co/Cu MLS increases with the Co content at $\hbar\omega \leq 4$ eV. The peak in $\sigma_{xx}(\omega)$ at $\hbar\omega \sim 5.5$ eV is mainly due to transitions from the *s* states at the bottom of the valence band to the *p* states above the Fermi level. The densities of Co and Cu *s* states are rather similar, except for the spin splitting of the former. As a result, the peak becomes broader with increasing Co content in the MLS, its magnitude being almost unchanged.

Calculated $\omega\sigma_{xy}^{(2)}$ spectra are shown in Fig. 25,*b*. The magnitude of the spectra of the Co/Cu MLS is smaller than that of pure fcc Co, also shown in Fig. 25,*b*, and approximately scales with the Co content. As compared to the $\omega\sigma_{xy}^{2}$ curve of Co, the spectra of the MLS have a less pronounced structure. For the model multilayers studied the peak centered at $\sim$ 2 eV in the Co spectrum is observed most distinctly for the 6Co/6Cu structure, where the Co sublayer is sufficiently thick. It is remarkable that all the spectra cross zero at the same energy of about 5 eV. Considering the $\omega\sigma_{xy}^{(2)}$ spectra leads one to conclude that the dominant contribution is provided by optical transitions involving Co electronic states. The states are modified by the hybridization with Cu states at the interface, the hybridization effects being of greater importance for the MLS with smaller Co sublayer thickness.

Magneto-optical effects originate from a complicated interplay of the spin–orbit coupling and exchange splitting. As can be inferred from perturbation theory (see, e.g., Refs. 12 and 84), the $\sigma_{xy}^{(2)}$ spectrum can be expanded as a sum of contributions proportional to the spin–orbit coupling strength ξ_{tl} of the electronic states with angular momentum *l* at a site *t*. From the results of test calculations with $\xi_{tl} = 0$ for all $l \neq 2$ it has been found that the MO properties of the Co/Cu multilayers are governed mainly by the spin–orbit coupling of *d* electrons. Then calculations were done with the value of ξ_{tl} nonzero only for either the Co *d* or Cu *d* states. The results of the calculations for a 2Co/4Cu multilayer are shown in Fig. 26. It can be seen that the Cu contribution is, in general, significantly smaller than the contribution from the Co sites. There are two inequivalent Cu atoms in the 2Co/4Cu multilayer, one of them being located at the Co/Cu interface and the another one in the interior of the Cu slab. From test calculations with ξ_{tl} set to zero for the interfacial Cu sites it has been found that the contribution from the interior Cu sites to the $\sigma_{xy}^{(2)}$ spectrum is negligible. The spin-obit coupling strengths for Co and Cu *d* states are, however, of the same order of magnitude. The relatively small effect of the Cu sites on the off-diagonal conductivity component can be explained by the fact that the exchange splitting at the Cu sites is much smaller than at the Co ones (see Figs. 23 and 24). Calculations were performed assuming zero exchange splitting at all Cu sites, and it was found that the effect of «switching-off» the exchange splitting on the $\omega\sigma_{xy}^{(2)}$ of Co/Cu MLS is negligible. The results support the conclusion that the dominant role is played by the Co contribution to the MO properties of the Co/Cu MLS.

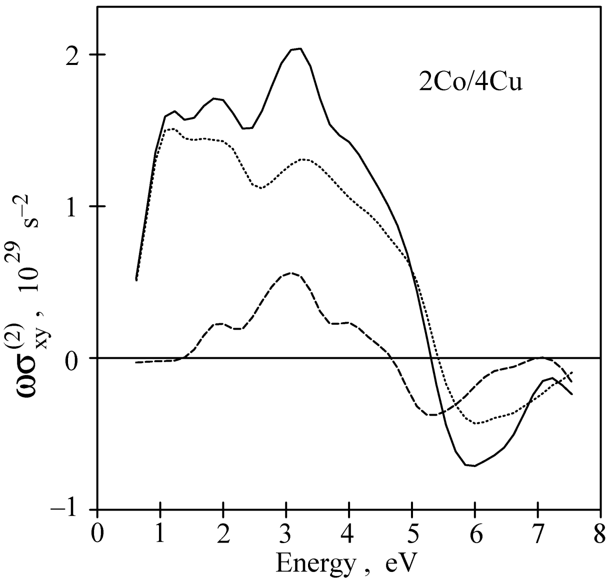

Fig. 26. The influence of the Co and Cu spin-orbit coupling strength on the theoretical $\omega\sigma_{xy}^{(2)}$ spectrum of 2Co/4Cu multilayer. The whole spectrum is shown by solid line. Dashed and dotted lines denote the spectra calculated with nonzero spin-orbit coupling strength at Co and Cu sites, respectively [82].

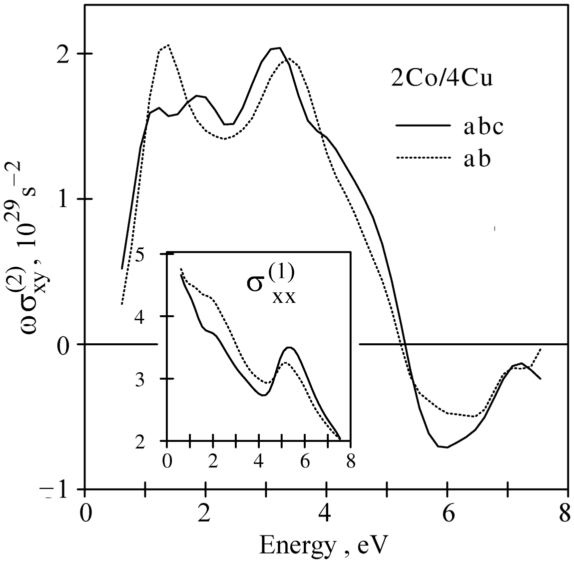

Fig. 27. Calculated $\omega\sigma^{(2)}_{xy}$ spectra of 2Co/4Cu multilayers with *abc* and *ab* stacking sequences. In the insert the corresponding $\sigma^{(1)}_{xx}$ spectra are shown [82].

To investigate the dependence of the $\sigma_{\alpha\beta}$ on local environment, calculations were performed for 2Co/4Cu MLS with *abc* and *ab* stacking sequences of the close-packed planes. In the both MLS the number of Co and Cu atoms among both the first and the second nearest neighbors around each site is the same, but the local symmetry is different. The calculated $\omega\sigma^{(2)}_{xy}$ spectra are shown in Fig. 27. Although the overall shape of the curves is similar, the fine structure is rather different. There are, also, differences in the corresponding $\sigma^{(1)}_{xx}$ curves shown in the insert in Fig. 27. It has been found that the joint density of states calculated for MLS with different kinds of stacking sequences are almost identical. Taking into account that the joint density of states is determined only by the band structure of a compound, one can conclude that the details of the short range order affect the optical and MO spectra of the Co/Cu MLS mainly via the transition matrix elements.

Calculated polar Kerr rotation and ellipticity spectra for the Co/Cu MLS are shown in Fig. 28. The spectra reproduce well the dependence of the magnitude of the UV peak on the Co content observed experimentally for the Co/Cu MLS studied. However, the calculated spectra are more structured. A well defined peak at ~ 2 eV in the polar Kerr rotation, which is a characteristic feature of all the measured spectra, is distinctly present in the theoretical spectrum of the 6Co/6Cu multilayer. A possible explanation is that due to the smaller Co and Cu sublayer thicknesses in the calculated model MLS as compared to the experimentally studied samples, the transitions to/from electronic states modified by the hybridization at the Co/Cu interfaces give a relatively large contribution to the MO spectra.

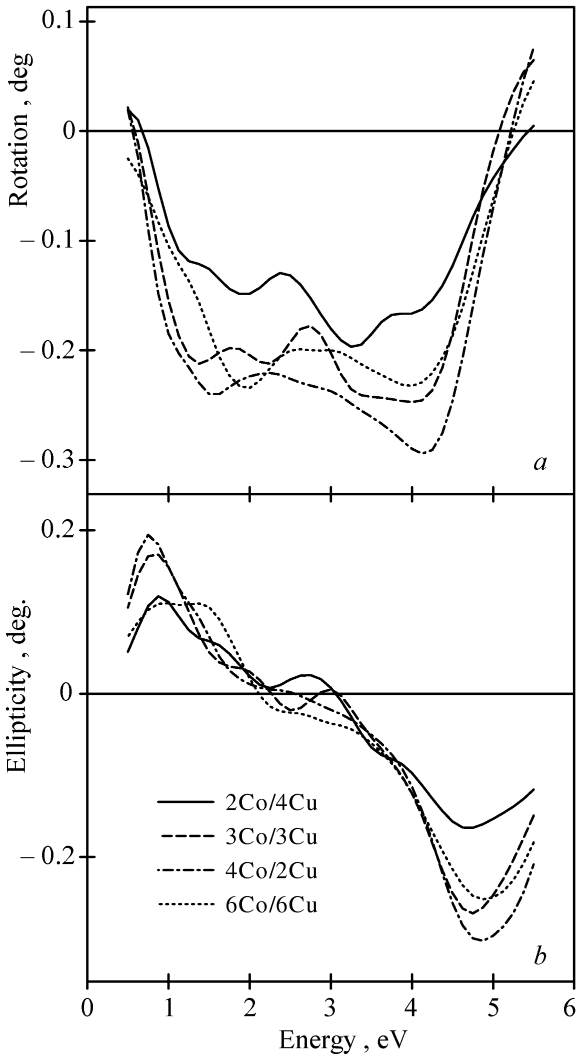

Fig. 28. Calculated polar Kerr rotation (*a*) and ellipticity (*b*) spectra of the model Co/Cu multilayers [82].

Accordingly to the experimental data, the low-energy peak in the $\omega\sigma^{(2)}_{xy}$ spectra of the Co film as well as of the Co/Cu MLS is located below 2 eV. The feature in the $\sigma^{(1)}_{xx}$ curves which is related to the Cu plasma edge and manifests itself as a sharp peak in the Kerr rotation spectra is centered at 2.1 eV. On the other hand, the calculations predict that the peak in $\omega\sigma^{(2)}_{xy}$ of Co and the edge of interband transitions in Cu should lie at a similar energy position of approximately ~ 2 eV. The discrepancy may be due to the fact that the LSDA approximation is only moderately successful in the description of the energy band structure and MO properties of ferromagnetic 3*d* metals, especially Ni and Co [74,85,86].

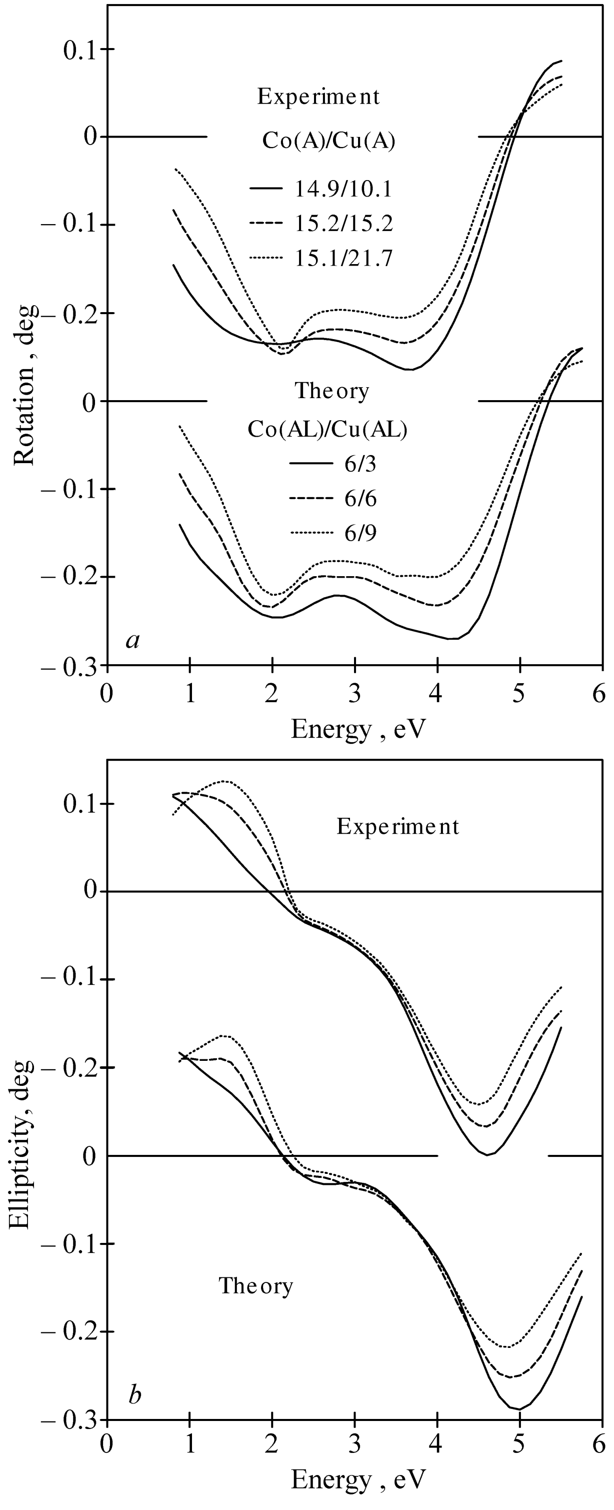

Fig. 29. The comparison of the polar Kerr rotation (*a*) and ellipticity (*b*) spectra measured for Co/Cu MLS films with the spectra calculated for the model *n*Co/*m*Cu multilaers (the sublayer thicknesses are expressed in the key for the experimental films (in Å) and for the calculated structures (in atomic layers AL) [82].

Ab initio calculations of polar Kerr rotation and ellipticity spectra were performed for 6Co/3Cu, 6Co/6Cu, and 6Co/9Cu multilayers assuming model multilayer structures with ideal interfaces. The calculated spectra are compared with the experimental ones in Fig. 29. Despite the idealized multilayer structures, good agreement between the theory and experiment is observed. Besides the overall similarity in the shape of the measured and calculated spectra, the calculations reproduce well the main trends in amplitudes of the spectra in different energy regions.

In conclusion it should be pointed out that from both the experimental and theoretical studies it follows that despite the spin polarization of the Cu *d* states due to the hybridization with the Co states at the MLS interface, the dominant contribution to the off-diagonal part of the optical conductivity tensor of the Co/Cu MLS comes from interband transitions involving Co electronic states. The feature observed at $\hbar\omega \sim 2.1$ eV in the spectra of the optical conductivity tensor component $\sigma_{xx}^{(1)}$ is related to the edge of interband transitions from Cu *d* states in the Cu sublayers and is responsible for the peak at 2.1 eV in the polar Kerr rotation spectra of the MLS studied. There are some discrepancies between the experimental and theoretical results mainly in the description of the Co-related peaks of the optical and MO spectra of the Co/Cu MLS. Nevertheless, the *ab initio* calculations reproduce the main features of the spectra and provide an explanation of their microscopic origin.

6. Magneto-optical anisotropy in Fe_n/Au_n superlattices

Many important physical properties of magnetically ordered compounds depend on the relative orientation of the magnetization and the crystallographic axes, as the spin subsystem is coupled to the lattice by the spin–orbit (SO) interaction. The magnetocrystalline anisotropy (MCA), which is the energy that directs the magnetization along a certain crystallographic axis, is a ground state property of a crystal. The magneto-optical anisotropy (MOA), defined as the dependence of the off-diagonal part of the optical conductivity tensor on the magnetization direction, arises as a result of electronic excitations and is due to the spin and orbital polarizations of initial and final states.

Although the MCA has been widely studied both experimentally [87] and theoretically [88–91] in a large number of materials, the investigations of the MOA are still restricted to a few cases only. Theoretical calculations have been performed for Co, FePt, CoPt [92], CoPd [48], and CrO_2 [58]. Experimentally, however, the orientation dependence of the magneto-optical (MO) Kerr effect has been observed in only one magnetic system, hcp Co. In the equatorial Kerr effect Ganshina et al. [93], and in the longitudinal Kerr effect (LKE) configuration Osgood et al. [94] studied the dependence of the magnitude of the Kerr effect on the orientation of the magnetization with respect to the c axis, both lying in the basal plane of the hcp Co sample. For the polar Kerr effect (PKE) configuration with magnetization perpendicular to the sample plane, Weller et. al. [68] observed an orientation dependence of the PKE by using two epitaxial hcp Co films with different, (0001) and $(11\bar{2}0)$, basal planes.

An extensive experimental and theoretical study of the observed large magneto-optical anisotropy was presented in Ref. 95 for a series of Fe_n/Au_n superlattices prepared by molecular beam epitaxy with $n = 1, 2, 3$ of Fe and Au atomic planes of (001) orientation. The $(Fe_1/Au_1) \times 20$ and $(Fe_2/Au_2) \times 10$ and $(Fe_3/Au_3) \times 7$ MLS were grown by MBE under UHV conditions (base pressure during preparation below 5×10^{-10} mbar) on a 30 nm (001) Au buffer layer (preceded by a 4 nm Fe (001) seed layer), deposited on a MgO (001) cleaved substrates in a multi-stage process [96]. The whole structure was finally covered by a 5 nm Au cap layer. The Fe and Au monolayers were deposited alternately at 340 K at the rate of about 0.2 nm/min, as controlled by a quartz microbalance with an accuracy of ± 5%. A very uniform growth conditions are preserved for subsequent layers, resulting in a high epitaxial quality of the superlattices. For the growth mode and the resulting structure of the Fe/Au MLS an important role is played by the Au self-surfactant effect, which was observed when single Fe films were grown on the reconstructed (001)Au surface [96,97]. During the Fe growth, the Au surface segregation occurs by an atomic place exchange that leads to the formation of one Au monolayer on top of the growing Fe film. This process, particularly important for the growth of the Fe_1/Au_1 monatomic superlattices, is responsible for a deviation from a perfect layer structure, as was observed by Takanashi et al. [98] by XRD measurements. The conversion-electron Mössbauer spectroscopy (CEMS) analysis [99] clearly reveals that the $L1_0$ phase, characterized by a tetragonal distortion that is reflected in a large contribution of the quadrupole interaction to the hyperfine pattern, is present in the $(Fe_1/Au_1) \times 20$ MLS. However, the amount of the $L1_0$ phase is only ~ 30% of that expected for perfect layer growth. The vertical mass transport accompanying the MLS growth leads to Fe aggregation, so that the resulting structure may be regarded as a mixture of a monolayer and double-layer (and to a less extent also tri-layer) MLS. Nevertheless, it is enough to induce a strong perpendicular anisotropy, which forces the magnetization to the normal direction. The $L1_0$ phase disappears abruptly when the MLS modulation period is increased. For the $(Fe_2/Au_2) \times 10$ MLS, only traces of the component attributed to the tetragonally distorted phase can be found in the CEMS spectrum. The CEMS spectrum for the $(Fe_3/Au_3) \times 7$ sample resembles the one measured for a single Fe tri-layer film sandwiched between Au [99].

6.1. Experimental results and data analysis

Most MO studies of the MLS employ polar magnetization geometry, PKE, and normal light incidence. The PKE configurations alone cannot be used, however, to study the MO orientation effects in a very rich family of magnetic layered structures. The reason is that the main structural anisotropy axis is the axis perpendicular to the film surface, and no other basal planes exist. The only possibility is to use the polar and longitudinal (or equatorial) Kerr effect geometries simultaneously. This approach is more complicated as additional data on the optical constants are required to extract the basic quantities — optical conductivity tensor components — underlying the MO spectra.

In Fig. 30 the complete set of experimentally obtained ellipsometric and magneto-optical spectra in both the polar and longitudinal magnetization geometry for the Au(5 nm)/$(Fe_1/Au_1) \times 20$/ Au(30 nm)/Fe(4 nm) /MgO(001) sample is presented. As is seen in Fig. 30,*a*, the spectral dependence of the effective refractive index n and the extinction coefficient k of the sample exhibits an overall shape close to that of Au metal, with the well-known feature at the photon energy 2.5 eV, where there is the superposition of the Drude-like intraband transitions and the interband transition edge. Such dependence can easily be understood by taking into account that the predominant parts of the sample are the Au overlayer and underlayer. The effective magneto-optical PKE rotation θ^{PK} and ellipticity η^{PK} spectra of the sample are shown in Fig. 30,*b*. The essential points of the experimental θ^{PK} spectrum are the prominent negative peak centered at around 2.5 eV (i.e., in the Au plasma-edge spectral region), and a hump clearly visible near 3.2 eV. The θ^{PK} changes sign above 4 eV, and a positive peak at 4.7 eV is formed. The θ^{PK} enhancement at the plasma edge of Au (around

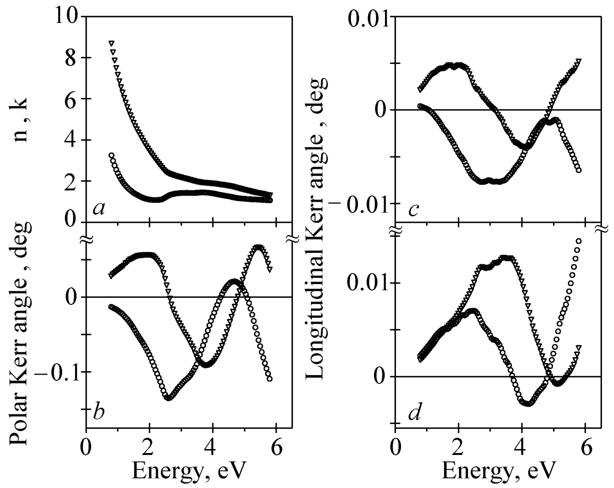

Fig. 30. Experimental results for Fe_1/Au_1 MLS: refractive index and extinction coefficient (*a*), polar Kerr rotation and ellipticity (*b*), longitudinal Kerr rotation and ellipticity for *s* (*c*) and *p* (*d*) light polarizations. In the panels, refractive index and rotation are depicted as circles, and extinction coefficient and ellipticity as triangles [95].

2.5 eV) is well explained by the classical optic multilayer model and is not related to the modification of the electronic structure of the intrinsic magnetic Fe_1/Au_1 multilayer. The corresponding η^{PK} spectrum changes sign at the energy of the plasma edge of Au and in the UV spectral region exhibits a two-peak structure with a negative peak at 3.8 eV and a positive one at 5.5 eV. The PKE spectra measured in the Fe_2/Au_2 and Fe_3/Au_3 superlattices (not shown) exhibit similar behavior to Fe_1/Au_1 , with the peak structure in the UV spectral range shifted to higher energy. The main features and trends in PKE spectra of Fe_n/Au_n superlattices modulated by integer atomic layers of Fe and Au are in agreement with those reported in Refs. 100 and 101. Similar characteristic structure in the PKE spectra in the UV spectral range (more distinct than in the multilayers) was observed in ultrathin Fe layers sandwiched by Au layers and was assigned to optical transitions involving quantum-well states [102,103].

The corresponding complex LKE spectra measured in the longitudinal Kerr magnetization geometry at a angle of light incidence 75 deg are shown in Fig. 30,*c* and Fig. 30,*d* for *s* and *p* light polarizations, respectively. The measured θ^{LK} and η^{LK} appear one order of magnitude smaller than for the PKE. In the LKE spectra, the plasma edge of the Au overlayer and underlayer of the sample manifests itself as a peak or shoulder near 2.6 eV. As it is seen in Fig. 30,*c* and *d*, in the spectral region above 2.5 eV the θ^{LK} spectra are dominated by a peak at 3.2 and a minimum at around 5.0 eV for *s* polarization and a peak at 4.1 eV for *p* polarization. The corresponding features in the η^{LK} spectra are the peak centered at 4.1 for *s* polarization and the peaks at 3.4 eV and 5.1 eV for *p* polarization, respectively. The LKE spectra are consistent for the *s* and *p* light polarizations, and the optical functions *n* and *k* determined from the LKE data alone agree well with those measured directly by the elipsometric method. It should be pointed out that one cannot expect direct correspondence between the shape of the spectra and the position of the energy peaks measured in polar and longitudinal geometry because the LKE spectra are strongly dependent on the angle of incidence of the light (particularly for *p* polarization, when the angle of incidence approaches its principal value, equal to about 75 deg for the structures studied). Therefore, the direct comparison of the PKE and LKE spectra is not adequate, and appropriate treatment should be done by evaluation of the optical conductivity tensor components from the measured spectra. It is well known that the absorptive part of the tensor only, but not the Kerr rotation itself, is directly connected with the optical transitions between electronic states, their strengths and energy positions. Therefore, in the following, we will consider the energy dependence of the conductivity tensor components underlying the MO effects for the superlattices studied.

The effective optical conductivity tensor components, diagonal σ_{xx}^{eff} and off-diagonal $\omega\sigma_{xy}^{\text{eff}}$, $\omega\sigma_{xz}^{\text{eff}}$ were determined with the use of Eq. (3) from the measured optical and MO spectra according to Eq. (2) for the PKE and Eq. (6) for the LKE. The Fe_n/Au_n superlattices studied are two-dimensional structures and can exhibit optical anisotropy (i.e., the σ_{xx} and σ_{zz} tensor components can differ). Consequently, Eq. (5) for an optically anisotropic medium should be used instead of Eq. (6) to determine the off-diagonal tensor component. Unfortunately, in the case of thin *metallic* films or MLS direct ellipsometric measurements allow one to determine the σ_{xx}^{eff} tensor component only. As will be shown in the next Section, the errors caused by the using the Eq. (6) for an optically isotropic medium to extract σ_{xz}^{eff} from LKE data are of little importance for the Fe_n/Au_n .

The results for effective complex σ_{xx}^{eff} , $\omega\sigma_{xy}^{\text{eff}}$, and $\omega\sigma_{xz}^{\text{eff}}$ optical conductivity spectra of the -Au(5 nm)/(Fe_1/Au_1)×20/Au(30 nm)/Fe(4 nm)/MgO(001) sample are presented in Fig. 31,*a* and *b*, respectively. In Fig. 31,*a* the σ_{xx} spectra of a 100 nm thick fcc Au film deposited on GaAs(001)

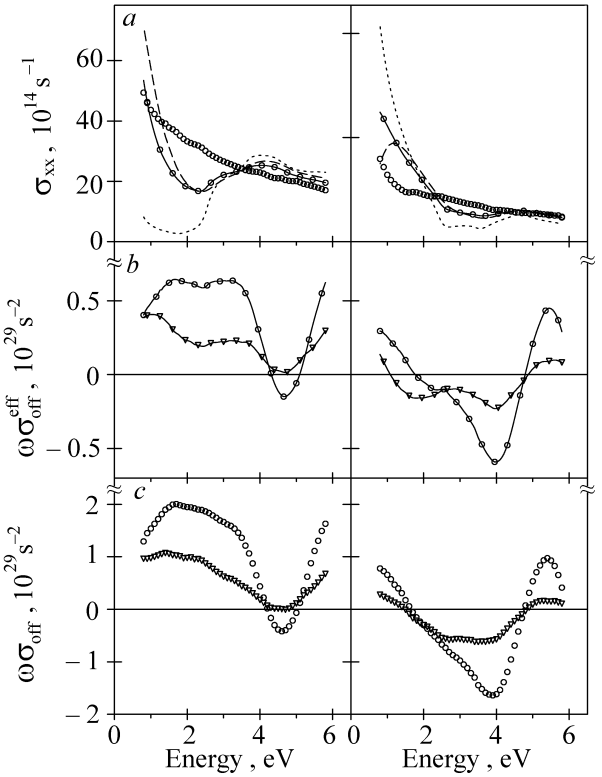

Fig. 31. Experimental absorptive (left panels) and dispersive (right panels) parts of the optical conductivity for the Fe_1/Au_1 sample. In the panels (*a*) the effective diagonal tensor components of the whole sample (solid lines with circles), the buffer sample (dashed lines), thick Au film (dotted lines), and the extracted (see text) component of the intrinsic Fe_1/Au_1 structure (circles) are shown. In the panels (*b*) the off-diagonal effective tensor components derived from the polar (solid lines with circles) and longitudinal (solid lines with triangles) Kerr effect are shown. In the panels (*c*) there are the extracted off-diagonal tensor components of the intrinsic magnetic Fe_1/Au_1 structure derived from PKE (circles) and LKE (triangles) [95].

as well as the buffer sample Au(30 nm)/Fe(4 nm)/MgO(001) used as the substrate to grow the Fe_n/Au_n superlattices are also included. As can be seen from Fig. 31,*a* there is significant difference between the effective $\sigma^{\rm eff}_{xx}$ spectra for the whole structure and the buffer sample as compared to that of the Au film in the spectral range below 2.5 eV. The rapid changes of the optical constants at the energy 2.5 eV caused by onset of Au interband transitions are clearly visible for all the samples. The characteristic features of the absorptive part of the $\omega\sigma^{\rm eff}_{xy}$ spectrum (Fig. 31,*b*, solid lines with circles) of the whole structure are two broad peaks of comparable amplitude centered at around 1.6 and 3.3 eV and a negative minimum at 4.7 eV. The dispersive part of the $\omega\sigma^{\rm eff}_{xy}$ is dominated by a negative peak at 3.9 eV and a positive one at 5.3 eV. The complex $\omega\sigma^{\rm eff}_{xz}(\omega)$ functions (Fig. 31,*b*, solid lines with triangles) evaluated independently from the LKE data measured for *s* and *p* light polarization are the same. As compared to the energy dependence of $\omega\sigma^{\rm eff}_{xy}(\omega)$, significant differences between the shape and the magnitude of the spectra are clearly visible. The IR peak position in the absorptive part of $\omega\sigma^{\rm eff}_{xz}$ shifts to lower energy, and the spectrum amplitude is much smaller.

The spectra of the conductivity tensor components discussed above represent the effective tensor components of the whole complex sample composed of the specific magnetic Fe_n/Au_n structure and the Au cap layer and underlayer film. To compare the theoretical *ab initio* calculations with the experiment and to discuss the origin of the magneto-optical and MOA effects of the magnetic superlattices, the tensor components for the intrinsic magnetic Fe_n/Au_n structure alone should be extracted from the experimental data. For this purpose we adopted the phenomenological matrix formalism based on the Maxwell theory, providing computer modeling of the MO response for a given structure (known as multi-reflection calculation) [104]. The procedure assumes that the dielectric tensors of the constituent layers of the structure and their thicknesses are known. In our calculation, the thicknesses of the constituent layers determined from the technological data were used. To avoid possible uncertainties and to obtain the most precise results, the optical and magneto-optical response of the buffer underlying the Fe_n/Au_n structure, composed of the Au(30 nm)/Fe(4 nm)/MgO(001), was directly measured with the use of a control sample and was subsequently used in the multi-reflection calculations. Finally, a two-layer system was considered, composed of the nonmagnetic Au cover layer and the magnetic $(Fe_n/Au_n) \times N$ superlattice on the Au(30 nm)/Fe(4 nm)/MgO(100) buffer substrate. In the procedure, the contribution of a single layer of given thickness is determined through its characteristic matrix, composed of the medium boundary and the medium propagation matrices [104]. The overall structure of the film is treated as a single layer with the parameters expressed in terms of those of individual sublayers.

The unknown tensor components of the intrinsic $(Fe_1/Au_1) \times N$ MLS structure were extracted by solving numerically the multi-reflection equations. The results for the Fe_1/Au_1 structure are shown in Fig. 31,*a* for σ_{xx} (circles) and in Fig. 31,*c* for $\omega\sigma_{xy}$ (cirles) and $\omega\sigma_{xz}$ (triangles). The spectra represent the results after eliminating the MO contribution from the complex underlayer and Au overlayer. In the following discussion, the off-diagonal component $\omega\sigma_{xy}$ for the magnetization **M** parallel to the (001) direction will be denoted as $\omega\sigma_{\rm off}^{\|}$ whereas for the $\omega\sigma_{xz}$ with the magnetization **M** perpendicular to the (001) direction we will use the notation $\omega\sigma_{\rm off}^{\perp}$. As compared to the effective tensor components, the feature related to the plasma edge of Au at 2.5 eV disappears for the $\omega\sigma_{\rm off}^{\|}$ and $\omega\sigma_{\rm off}^{\perp}$ spectra. The overall structure of the extracted off-diagonal tensor components of the magnetic superlattice alone is similar to that of the effective ones, and the most significant changes in the spectra appear in the IR spectral range. The most important conclusion is that both the effective and the extracted off-diagonal tensor components of the magnetic superlattice exhibit large orientational anisotropy with respect to the magnetization direction.

6.2. Comparison of the experimental and theoretical spectra in $\mathbf{Fe}_n/\mathbf{Au}_n$ *MLS*

The band structure calculations in Ref. 95 considered an $\rm Fe_1/Au_1$ MLS system with one-by-one stacking of (001) planes whose structure can be regarded as $L1_0$-type (Fig. 32,*a*). The lattice parameters used were chosen as follows. The in-plane atomic spacing was taken as an average between the Au and Fe bulk values ($a = 4.066$ Å). The out-of-plane lattice spacing for the $\rm Fe_1/Au_1$ MLS was taken from the recent work of Sato et al. [101] as 1.915 Å, which is slightly lower than the previously published value [98,105] used in our previous calculation [106]. The structures $\rm Fe_2/Au_2$ and $\rm Fe_3/Au_3$ are presented in Figs. 32,*b* and 32,*c*. There is no experimental knowledge about the three interlayer spacings, Au–Au, Au–Fe, and Fe–Fe, in these structures. The Au–Au spacing was taken the same as in fcc Au, 2.04 Å. For the Au–Fe spacing, the value 1.74 Å can be derived from the rigid sphere model as a mean between the fcc Au (2.04 Å) and bcc Fe (1.43 Å) bulk values. Similar values for the Au–Fe interlayer spacings have been obtained by total energy minimization using the LMTO *ab initio* calculations. Using the experimentally determined superlattice periods in $\rm Fe_2/Au_2$ and $\rm Fe_3/Au_3$ MLS structures published in Ref. 101 as constraints, the one-parameter minimization was performed. As a result, values of 1.76 Å and 1.74 Å for the Au–Fe interlayer spacing and corresponding values of 1.69 and 1.58 Å for the Fe–Fe interlayer spacing were obtained for the $\rm Fe_2/Au_2$ and $\rm Fe_3/Au_3$ MLS, respectively.

For the quantitative analysis of the magneto-optical anisotropy it is convenient to present the anisotropy as the difference between the off-diagonal conductivity tensor components $\omega\sigma_{\rm off}^{\|} - \omega\sigma_{\rm off}^{\perp}$, where the factor ω provides compatibility with the ωσ spectra themselves. In Fig. 33 the $\omega\sigma_{\rm off}^{\|}$ and $\omega\sigma_{\rm off}^{\perp}$ spectra of the MLS of the nominal $\rm Fe_1/Au_1$ structure, extracted from the experimental PKE and LKE data as described in the previous Section, and the MOA are compared to the corresponding spectra calculated for the ideal $\rm Fe_1/Au_1$ $L1_0$ structure.

Overall, both the spectral shape and the magnitude of the experimental optical conductivity spectra are qualitatively reproduced by the LSDA calculations. However, the positions of the calculated

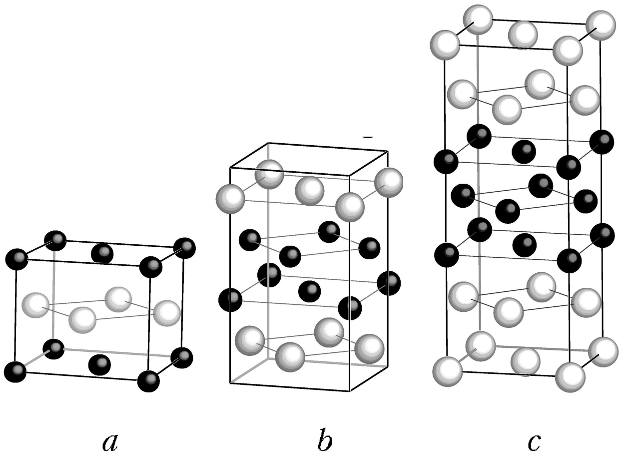

Fig. 32. The unit cells used for $\rm Fe_1/Au_1$ ($L1_0$) (*a*), $\rm Fe_2/Au_2$ (*b*), and $\rm Fe_3/Au_3$ MLS (*c*). Black spheres are Fe atoms and shadowed ones are Au atoms [95].

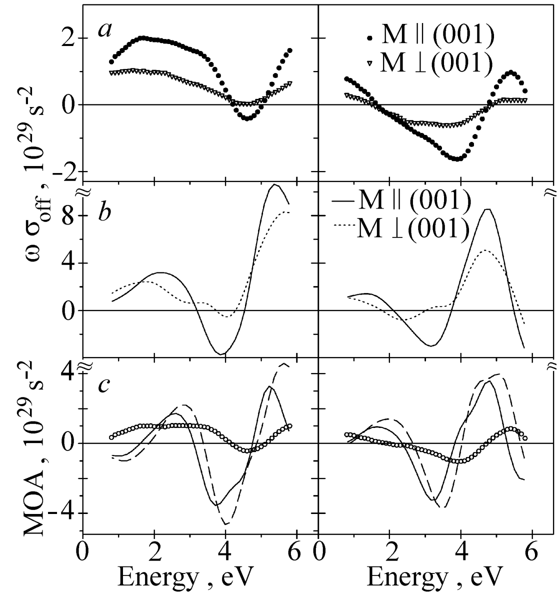

Fig. 33. Absorptive (left panels) and dispersive (right panels) parts of the off-diagonal conductivity tensor of $\rm Fe_1/Au_1$ MLS; experimental results (*a*), LSDA calculated spectra for $\rm Fe_1/Au_1$ MLS (*b*), the MO anisotropy spectra (*c*) (symbols represent experimental data, solid lines LSDA, and dashed lines LDA+U theory) [95].

prominent peaks in the absorptive part of $\omega\sigma_{\text{off}}^{\|}$ at 3.8 eV and 5.2 eV are shifted to smaller energies as compared to the experiment. Also, the theoretical calculations predict larger MOA in comparison with the experimental value in the nominal Fe_1/Au_1 structure. One of the possible reasons is that due to the inexact treatment of the electron exchange and correlations the LSDA underestimates the binding energy of d states and the threshold of interband transitions in noble metals as compared to photoemission and optical measurements [107,108].

It seems quite likely that the use of a more appropriate approximation for the self-energy can give rise to a shift of the quasiparticle energy bands originating from the Au 5d states and, as a result, to a better agreement between the theory and the experiment. In Ref. 95 the LDA+U method [109] was adopted as a step beyond the LSDA in the treatment of the electronic correlations. As was discussed in Refs. 110 and 111, the LDA+U method can be considered as a rough approximation to both the self-interaction correction and to the self-energy of a system with strongly interacting electrons. Moreover, it has been found that the application of the LDA+U method to pure noble metals allows one to improve the calculated energy position of the threshold of the interband optical transitions and provides a better approach to the description of their MO spectra [112]. In the case of the Fe_1/Au_1 MLS $U_{\text{eff}} = 2.5$ eV was applied to Au 5d states [95]. This value of U_{eff}, considered as a parameter of the model, was found to give the best agreement between the calculated and experimental optical conductivity for fcc Au. The use of the LDA+U approximation for Fe_1/Au_1 MLS does improve slightly the calculated energy position of the peaks of the off-diagonal optical conductivity for both orientations of the magnetization (not shown) but there is no improvement in the shape of the spectra. Comparing the MOA calculated within the LSDA and LDA+U methods (see Fig. 33,c) to the experimental spectrum, one can conclude that the LDA+U approximation does not improve the description of the MOA in the nominal Fe_1/Au_1 structure.

Another and maybe even more important source of the discrepancies is that the sample studied is not an ideal monoatomic Fe_1/Au_1 MLS of $L1_0$ structure but rather a mixture of mono- and double-layer structures. Having this in mind, we modeled the effective optical conductivity of the structure by a weighted average of the conductivities calculated for the Fe_1/Au_1 and Fe_2/Au_2 MLS: $\omega\sigma_{\text{off}} = x\omega\sigma_{\text{off}}^{1/1} + (1 - x)\omega\sigma_{\text{off}}^{2/2}$. The best agreement between the theory and the experiment, both in the MOA (Fig. 34,a) and the shape of the off-diagonal optical conductivity (not shown), was achieved with $x = 0.3$. This value agrees well with the results of the CEMS analysis [99].

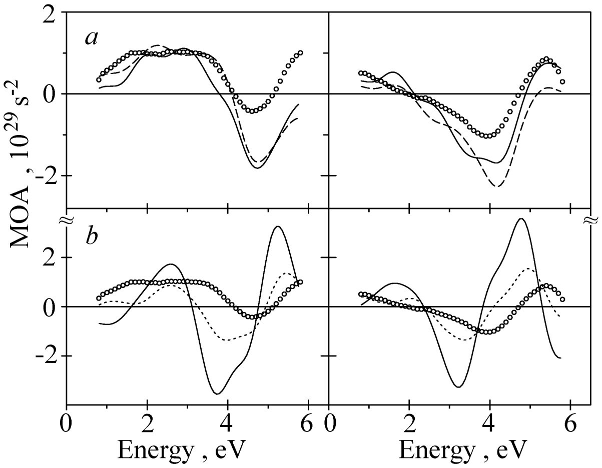

Fig. 34. Absorptive (left panels) and dispersive (right panels) part of the MOA measured for the Fe_1/Au_1 MLS (circles) compared with LSDA calculated spectra; MOA modeled with effective optical conductivity: $\omega\sigma_{\text{off}} = x\omega\sigma_{\text{off}}^{1/1} + (1 - x)\omega\sigma_{\text{off}}^{2/2}$ for $x = 0.3$ (solid lines) and calculated for supercell containing 1/1 and 2/2 substructures (see Fig. 35) (dashed lines) (a); MOA calculated for perfect Fe_1/Au_1 structure (solid lines) and for the structure with the substitutional disorder (see Fig. 36) (dotted lines) (b) [95].

In a more advanced approach, the interface roughness was studied by calculating the MO properties of the mixture of mono- and double layers, distributed over the whole structure. The composed Fe/Au structure was modeled using a large supercell containing side-by-side Fe_1/Au_1 and Fe_2/Au_2 component structures spread over 3 and 7 lattice constants (see Fig. 35). This ratio of the areas was chosen in correspondence with the simple procedure described above, in which the resulting spectra were expressed as the sum of individual

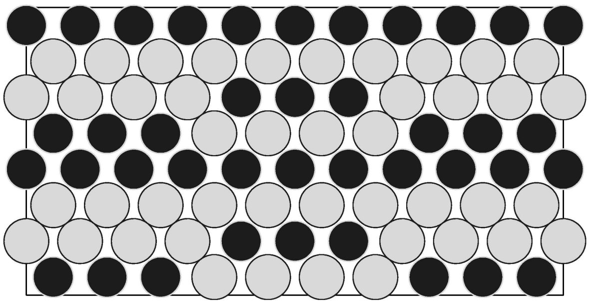

Fig. 35. Unit cell (doubled along z direction) of the Fe/Au structure composed of the 1/1 and 2/2 substructures (black spheres are Fe atoms and shadow ones are Au atoms) [95].

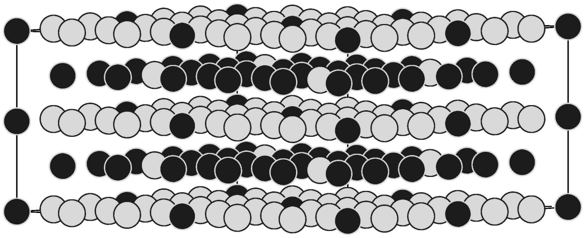

Fig. 36. Doubled $c(3/\sqrt{2}\times 3/\sqrt{2})$ unit cell used for modeling of alloying effect in the Fe/Au MLS (black spheres are Fe atoms and shadow ones are Au atoms) [95].

Fe_1/Au_1 and Fe_2/Au_2 contributions. The results of the *ab initio* calculations for the composed structure are shown in Fig. 34,*a*, from which an even better overall agreement between the theory and experiment both in the shape and the amplitude of the MOA spectra is observed. As the opposite case to the structure composed of well-defined mono- and double layers, a series of modelings was performed for examination of the effect of substitutional disorder on the MO spectra and MOA. Although the solubility of Au in bulk bcc Fe at temperatures up to 400 K is negligible [113], enhanced solubility of Au within the Fe layer up to 3% was observed for a 70 Å thick Fe film on Au(001) [114]. Even up to one order greater substitutional disorder was reported for the Fe/Au (001) structures in the monolayer regime by Blum et al. [97]. The incorporation of Au atoms in the Fe layers can be considered as an explanation (as discussed in Ref. 97) for larger Fe–Au interlayer spacing observed experimentally in the Fe_1/Au_1 structure, as compared to the spacings derived under the assumption of rigid atomic spheres of bulk Fe and Au metals. The effect will lead to larger effective Fe–Fe and Fe–Au interlayer spacings in Fe_n/Au_n MLS. The particular model structure used in the calculations is presented in Fig. 36. The structure is composed of alternating atomic planes of Fe and Au in which one per nine atoms is interchanged by Au and Fe, respectively (an interlayer spacing of 1.915 Å was taken). It was found that the moderate substitutional disorder leads mainly to a scaling of the amplitudes of the calculated $\sigma^{\parallel}_{\rm off}$ and MOA spectra without significant changes of their shape. In Fig. 34,*b* the MOA spectra calculated for the model structure (see Fig. 36) are shown. It is seen that an approximately twofold reduction of the MOA magnitude is observed when the level of the substitution is 11%.

Figures 37 and 38 show the experimentally obtained $\omega\sigma^{\parallel}_{\rm off}$ and $\omega\sigma^{\perp}_{\rm off}$ spectra in the MLS of nominal Fe_2/Au_2 and Fe_3/Au_3 structures for two orien-

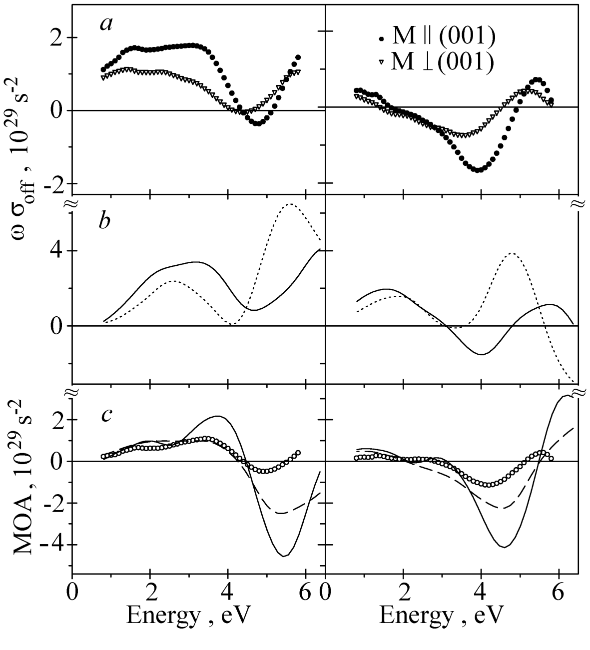

Fig. 37. Absorptive (left panels) and dispersive (right panels) parts of the off-diagonal conductivity tensor of Fe_2/Au_2 MLS; experimental results (*a*), LSDA calculated spectra (*b*). In the panels (*c*) the MOA spectra are shown (symbols represent experimental data, solid lines LSDA calculations for perfect Fe_2/Au_2 MLS, and dashed lines calculations for the structure with the substitutional disorder) [95].

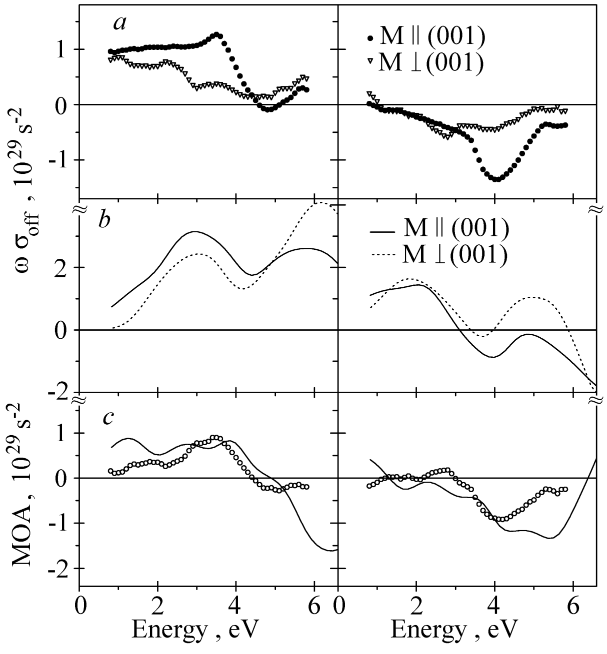

Fig. 38. Absorptive (left panels) and dispersive (right panels) parts of the off-diagonal conductivity tensor of Fe_3/Au_3 MLS; experimental results (*a*), LSDA calculated spectra (*b*). In the panels (*c*) the MOA spectra are shown (symbols represent experimental data, solid lines represent LSDA theory for perfect Fe_3/Au_3 MLS) [95].

tations of magnetization: $\mathbf{M} \parallel (001)$ and $\mathbf{M} \perp (001)$, together with the MOA, in comparison with the corresponding spectra calculated for the ideal Fe_2/Au_2 and Fe_3/Au_3 structures. For Fe_2/Au_2 MLS, the overall shape of the theoretical spectra corresponds well to the experimental ones (Fig. 37,*b*), and a better agreement of the MOA as compared to the previously discussed case of the ideal Fe_1/Au_1 (see Fig. 33) is observed (Fig. 37,*c*). The reason is that the ideal Fe_2/Au_2 MLS is a better approximation to the real experimental situation than was the case for the Fe_1/Au_1 MLS [99]. However, in the high-energy part of the spectra, above 4 eV, the $\omega\sigma^{\parallel}_{\text{off}}$ and $\omega\sigma^{\perp}_{\text{off}}$ and MOA amplitudes remain considerable higher than the ones obtained experimentally. To examine the origin of such a discrepancy, the influence of the substitutional disorder on the MOA was modeled in the case of the Fe_2/Au_2 MLS. In Fig. 37,*c* the MOA spectra calculated for a Fe_2/Au_2 MLS model structure are shown. The model structure used in this case is similar to that considered for the case of Fe_1/Au_1 MLS (Fig. 36) with the same substitutional disorder level and is composed of double numbers of the Fe-rich and Au-rich atomic layers with the experimental modulation period of 7.25 Å. It was found that the MOA magnitude for the Fe_2/Au_2 MLS in the high-energy part of the theoretical spectra is markedly reduced and is closest to the experimental values when the effect of the limited substitutional disorder at a level of the order of 10% is taken into account.

The experimental and theoretical results for the Fe_3/Au_3 structure are presented in Fig. 38. The overall agreement between the calculated and observed $\omega\sigma^{\parallel}_{\text{off}}$ and $\omega\sigma^{\perp}_{\text{off}}$ spectra for the Fe_3/Au_3 structure is less satisfactory than for the Fe_2/Au_2 MLS. One of the possible reasons is that the real structure of the Fe_3/Au_3 superlattice is far from the ideal model considered. Nevertheless, both the theoretical and the experimental MOA spectra are of comparable magnitudes. The modeling of the interfacial roughness effects and alloying for the Fe_3/Au_3 structure from first principles (much more complicated than for the simpler structures) is currently in progress.

Some conclusions can be drawn from the modeling performed: (i) The magnitude of the off-diagonal optical conductivity and MOA spectra is very sensitive to the actual structure at the interfaces, and thus the MO spectroscopy can provide useful independent information about the Fe/Au MLS structures, complementary to that derived from CEMS measurements. (ii) In the modeling of the roughness effect, even using areas of the component structures as small as a few atomic spacings leads to a result qualitatively close to that obtained from a simple additive formula for the superposition of the spectra. (iii) The magnitude of the MOA decreases with increasing the number of Fe and Au atomic layers of the superlattices. (iv) The limited substitutional disorder does not suppress the MOA effect in the Fe_n/Au_n MLS.

As was mentioned in Sec. 6.1 Fe_n/Au_n MLS can exhibit optical anisotropy, but the σ_{zz} component of the optical conductivity tensor is unavailable directly in the experiment. On the other hand, both σ_{xx} and σ_{zz} can be easily obtained from the calculations and allows us to verify numerically the correctness of using Eq. (6) instead of Eq. (5) to determine $\omega\sigma^{\perp}_{\text{off}}$ from the experimental data. The absorptive parts of the diagonal components of the conductivity tensor calculated for ideal Fe_1/Au_1 and Fe_2/Au_2 structures are shown in Figs. 39,*a* and *c*. The largest difference between the σ_{xx} and σ_{zz} spectra is observed for the Fe_1/Au_1 MLS below a photon energy of about 3.5 eV. For the Fe_2/Au_2 and also Fe_3/Au_3 (not shown in the figure) MLS the calculated optical anisotropy is significantly smaller. The theoretical conductivity tensor components were used to calculate the complex longitudinal Kerr angle according to the exact formula (5). Then the approximate $\omega\sigma^{\perp}_{\text{off}}$ was derived from the calculated LKE angle using the Eq. (6) for an isotropic medium. The off-diagonal conductivity spectra recalculated in this way are compared to $\omega\sigma^{\perp}_{\text{off}}$ obtained directly from the *ab initio* calculations in Fig. 39,*b* and *d*. A marked difference be-

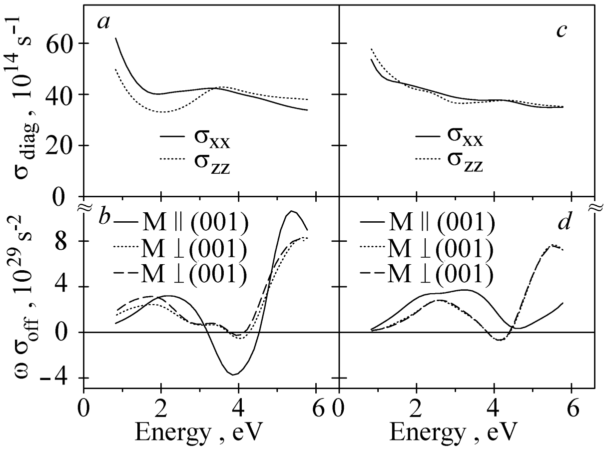

Fig. 39. LSDA calculated absorptive parts of the diagonal σ_{xx} and σ_{zz} (panels *a* and *c*) and off-diagonal $\omega\sigma^{\parallel}_{\text{off}}$ and $\omega\sigma^{\perp}_{\text{off}}$ (panels *b* and *d*) components of the optical conductivity tensor for Fe_1/Au_1 (left panels) and Fe_2/Au_2 (right panels) MLS. The *ab initio* calculated $\omega\sigma^{\perp}_{\text{off}}$ spectra are represented by dotted lines and the corrected ones by dashed lines (see text) [95].

tween the «exact» and «approximate» $\omega\sigma_{\rm off}^{\perp}$ values is observed in the IR range for the $\mathrm{Fe}_1/\mathrm{Au}_1$ MLS only. It diminishes to a negligible value above this energy region and can be completely neglected in the whole energy range for the $\mathrm{Fe}_2/\mathrm{Au}_2$ and $\mathrm{Fe}_3/\mathrm{Au}_3$ structures. The possible errors caused by using Eq. (6) instead of Eq. (5) are then small and do not affect the conclusion that the large MOA is related to the anisotropy of the off-diagonal conductivity tensor components.

6.3. Microscopic origin of the magneto-optical and orbital moment anisotropy in $\mathrm{Fe}_n/\mathrm{Au}_n$ *MLS*

To understand better the microscopic origin of the MOA, let us consider in detail the electronic structure of the $\mathrm{Fe}_1/\mathrm{Au}_1$ $L1_0$ MLS. Spin-projected densities of Fe and Au *d* states are shown in Fig. 40 and the calculated spin and orbital magnetic moments are summarized in Table 1. Within the Au(Fe) monolayer, each atom is surrounded by four other Au(Fe) atoms at a separation corresponding to the nearest-neighbor spacing in bulk Au(Fe). Because of the smaller number of the nearest neighbors of the same type, both the Fe and Au *d* states are much narrower than in the corresponding bulk metals. As a result the majority spin Fe *d* states are fully occupied, which leads to a significant enhancement of Fe spin magnetic moment (2.87 μ_B) compared to the value of 2.2 μ_B for bulk Fe. This enhanced magnetization has been observed [105], but the experimental value of $2.75 \pm 0.25\mu_B$ is somewhat smaller than the calculated one. Such a difference can be explained by the deviation of the sample structure from the ideal $L1_0$.

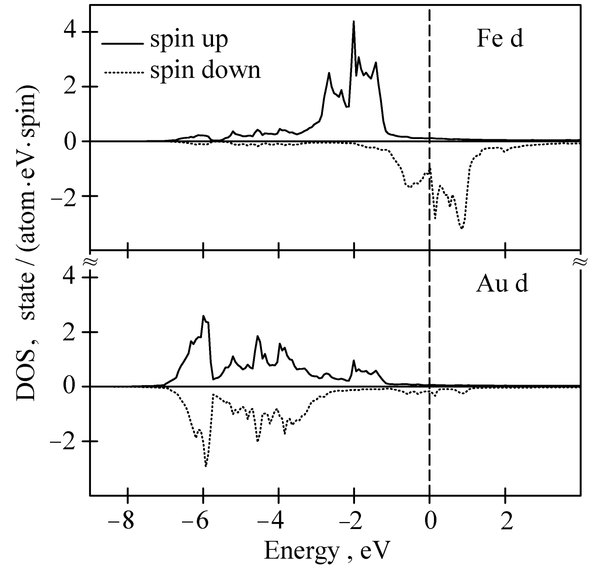

Fig. 40. LSDA spin-projected fully-relativistic partial DOS (in state/(atom · eV · spin)) of the $L1_0$ ordered $\mathrm{Fe}_1/\mathrm{Au}_1$ MLS [95].

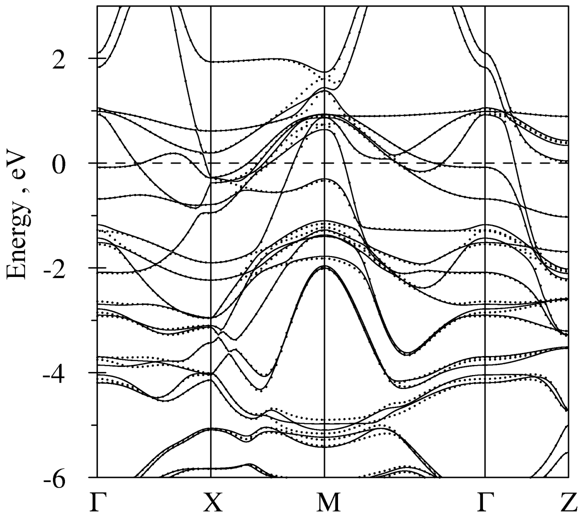

Fig. 41. LSDA energy band structure of the $L1_0$ ordered $\mathrm{Fe}_1/\mathrm{Au}_1$ MLS for two orientations of magnetization: **M** || (001) (solid lines), and **M** ⊥ (001) (dotted lines) [95].

The energy bands in $\mathrm{Fe}_1/\mathrm{Au}_1$ MLS calculated for different magnetization directions are shown in Fig. 41. This comparison is useful as it helps to identify the states that are sensitive to the change of the magnetization direction and, consequently, can potentially give a contribution to MOA, MCA, and the anisotropy of the orbital moment. In $\mathrm{Fe}_1/\mathrm{Au}_1$ MLS, for example, such states are the electronic states at about −4.0, −2.8, and −1.4 eV in the vicinity of the Γ point and those with energies −5.2, −1.5, and 0.5−1.8 eV located around the *M* symmetry point as well as along the Γ–*X*–*M*–Γ directions.

Comparing the values of the magnetic moments calculated for different magnetization directions, one can see from Table I that the Fe spin moments are almost independent of the magnetization direction. At the same time the anisotropy of the Fe orbital moment, which is determined mainly by the Fe *d* states, is quite large and is of the same order of magnitude as was experimentally observed in Co/Au MLS [115]. This behavior could be expected, as in the presence of the SO interaction the anisotropy of the orbital moment is of the order of ξ/Δ, where ξ is the SO coupling strength and Δ is the crystal field splitting, while the anisotropy of the spin moment is proportional to $(\xi/\Delta)^2$ [116]. As the Au *d* states are fully occupied, the spin and orbital moments at the Au site are small and depend weakly on the magnetization direction.

To understand better the anisotropic behavior of the Fe and Au orbital magnetic moments, let us introduce a site-dependent function $dm_l(E)$ given by

$$dm_{tl}(E) = \sum_{n\mathbf{k}} \langle \Psi_{tl}^{n\mathbf{k}} \,|\, \hat{l}_z \,|\, \Psi_{tl}^{n\mathbf{k}} \rangle \, \delta(E - E_{n\mathbf{k}}) \,, \qquad (17)$$

where $\hat{l}_z$ is the z projection of the angular momentum operator, $E_{n\mathbf{k}}$ and $\Psi_{tl}^{n\mathbf{k}}$ are the energy of the nth band and the part of the corresponding LMTO wave function formed by the states with angular momentum l inside the atomic sphere centered at the site t, respectively (see Ref. 95). In analogy to the l-projected density of states, $dm_{tl}(E)$ can be referred to as the site- and l-projected density of the expectation value of $\hat{l}_z$. This quantity has purely relativistic origins, and when the SO interaction is equal to zero one has $dm_{tl}(E) \equiv 0$. As van Vleck [117] showed for a free ion, the absence of orbital degeneracy is a sufficient condition for the quenching of the orbital moment, which mean that the first-order contribution should vanish: $\langle \Psi_{\mathbf{k}} \,|\, \hat{l}_z \,|\, \Psi_{\mathbf{k}} \rangle = 0$. Thus the $dm_{tl}(E)$ can be considered as a measure of the unquenching of the orbital moment due to the SO interaction.

Table 5

Calculated spin M_S and orbital M_L magnetic moments (in μ_B) of Fe_1/Au_1 versus magnetization direction [95].

Atom	State	$\mathbf{M} \parallel [001]$		$\mathbf{M} \perp [001]$	
		M_S	M_L	M_S	M_L
Fe	*s*	0.0097	0.0000	0.0098	0.0000
	p	−0.0033	−0.0006	−0.0030	0.0005
	d	2.8593	0.0920	2.8612	0.0587
	f	0.0019	−0.0008	0.0019	−0.0010
	total	2.8676	0.0906	2.8698	0.0582
Au	*s*	−0.0346	0.0000	−0.0345	0.0000
	p	−0.0567	0.0035	−0.0566	0.0058
	d	0.1085	0.0293	0.1098	0.0300
	f	0.0100	−0.0014	0.0100	−0.0016
	total	0.0272	0.0315	0.0287	0.0342

Furthermore, just as the number of states is defined as the integral of the DOS, we can define the integral of $dm_{tl}(E)$ as

$$m_{tl}(E) = \int_{E_b}^{E} dm_{tl}(E)\, dE \,, \qquad (18)$$

where E_b is the bottom of the valence band. Then the orbital moment m_l at the site t is given by

$$m_l \equiv m_{tl}(E_F) \qquad (19)$$

(here and henceforth we will drop the index t for simplicity).

Both $dm_l(E)$ and $m_l(E)$ are defined in a local coordinate system chosen in such a way that the z axis is directed along the magnetization and, consequently, they depend on the relative orientation of the magnetization, with respect to the crystallographic axes. In the case of Fe_n/Au_n MLS we will use the notations $m_l^{\parallel}(E)$ and $m_l^{\perp}(E)$ for $m_l(E)$ calculated with $\mathbf{M} \parallel (001)$ and $\mathbf{M} \perp (001)$, respectively. The difference of these two functions

$$\Delta m_l(E) = m_l^{\parallel}(E) - m_l^{\perp}(E) \qquad (20)$$

can provide useful information on the orientation dependence of the orbital moment. Figure 42 shows the functions $dm_l(E)$, $m_l(E)$, and $\Delta m_l(E)$ calculated for Fe and Au sites in Fe_1/Au_1 MLS. Here and in the rest of the paper we will only consider the contribution from the d orbitals to the m_l related functions. All the three functions show strong energy dependence. The variations of the functions at Au and Fe sites are comparable, but the Au d

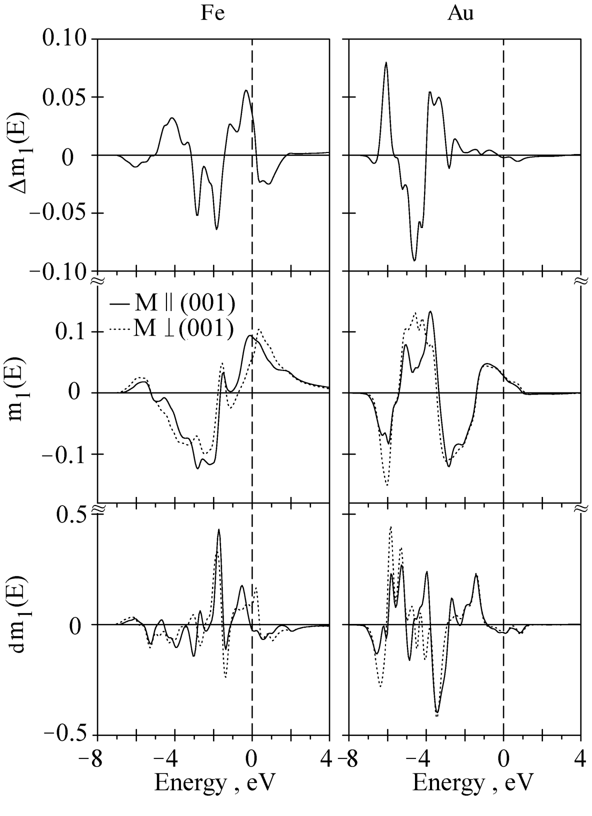

Fig. 42. The $dm_l(E)$ and $m_l(E)$ for two orientations of magnetization together with $\Delta m_l(E)$ for the $L1_0$ ordered Fe_1/Au_1 MLS (see text) [95].

orbital moment $m_l(E_F)$ is significantly smaller, as the Au d states are almost fully occupied (see Fig. 40). The anisotropy of the Au orbital moment $\Delta m_l(E)$ vanishes at E_F . At about −1.2 eV the Fe $d_\uparrow$ states are already occupied, while the $d_\downarrow$ states are still almost empty (Fig. 40), and, as a result, both $m_l(E)$ and $\Delta m_l(E)$ are zero at this energy. At the Fermi energy, however, strong anisotropy of Fe d orbital moment was observed.

To better understand such behavior, let us analyze the orbital character of the partial density of Fe d states in the vicinity of the Fermi level (Fig. 43). It should be recalled that the only nonzero matrix elements of the $\hat{l}_z$ operator calculated between real harmonics with $l = 2$ are $|\langle d_{x^2-y^2} | \hat{l}_z | d_{xy}\rangle| = 2$ and $|\langle d_{xz} | \hat{l}_z | d_{yz}\rangle| = 1$. Hence, the largest contribution to $m_l(E)$ can be expected from the $d_{x^2-y^2}$ and d_{xy} orbitals. Also, it should be pointed out that, in contrast to the case of transition metal films considered in Ref. 90, in which the on-site SO interaction is the only source of unquenching of the orbital moment, in a compound consisting of $3d$ metal atoms with a large magnetization and a relatively weak SO coupling and $5d$ atoms for which the SO coupling is strong, the unquenching of the $3d$ orbital moment can be caused to a great extent by the $3d$–$5d$ hybridization. In the particular case of Fe_1/Au_1 MLS there is a peak at −0.5 eV in the density of Fe $d_{x^2-y^2}$ states (Fig. 43) which hybridize rather strongly with Au d states. The density of d_{xy} states is constant in this energy interval and, as a consequence, the $dm_l(E)$ has a maximum at this energy for $\mathbf{M} \parallel (001)$. The states that form the peak of the DOS just above the Fermi level are predominantly of $d_{3z^2-r^2}$ character, and they do not contribute to $dm_l(E)$. When the magnetization direction changes from $\mathbf{M} \parallel (001)$ to $\mathbf{M} \perp (001)$ the local coordinate system in which $dm_l(E)$ is calculated should also be changed accordingly. In the new coordinate system the $d_{3z^2-r^2}$ orbital transforms into a linear combination of the $d_{3z^2-r^2}$ and $d_{x^2-y^2}$ orbitals, and a sharp peak of $dm_l^{\perp}(E)$ appears above the Fermi level and follows the shape of the corresponding peak of the density of $d_{3z^2-r^2}$ states. At the same time, the $d_{x^2-y^2}$ orbital, which plays the crucial role in the formation of the peak of $dm_l^{\parallel}(E)$ at −0.5 eV, transforms into $\sqrt{3}/2\, d_{3z^2-r^2} + 1/2\, d_{x^2-y^2}$, and, as a result of the reduced contribution of the $d_{x^2-y^2}$ orbital to the wave function, $dm_l^{\perp}(E)$ is suppressed below the Fermi level. These simple considerations allow one to explain the strong dependence of the Fe orbital moment on the magnetization direction in the Fe_1/Au_1 MLS.

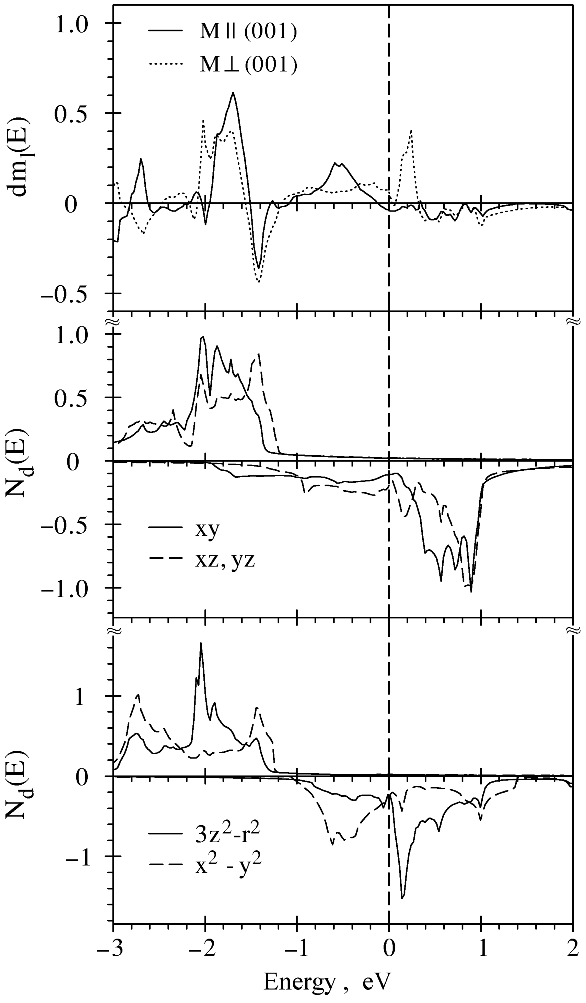

Fig. 43. The d-orbitals projected $dm_l(E)$ on Fe site for two orientations of magnetization and d-partial density of states (in state/(atom · eV · spin)) for the $L1_0$ ordered Fe_1/Au_1 MLS [95].

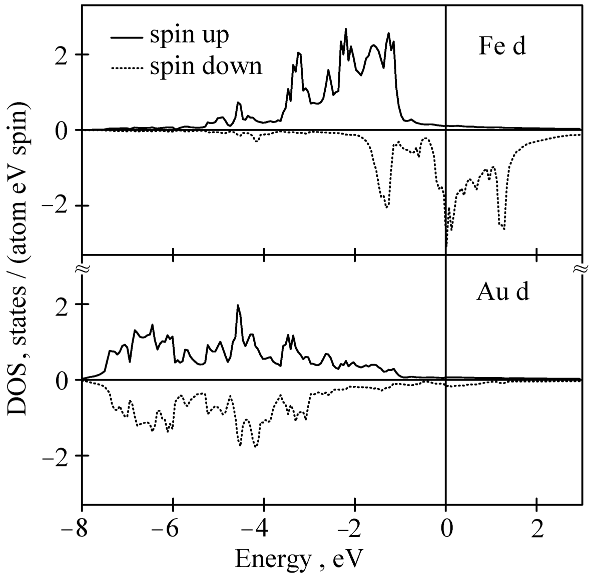

Fig. 44. LSDA spin-projected fully-relativistic partial DOS (in state/(atom · eV · spin)) of the Fe_2/Au_2 MLS [95].

Spin-projected densities of Fe and Au d states for Fe_2/Au_2 MLS are shown in Fig. 44, and the calculated spin and orbital magnetic moments are given in Table 2. As compared to the results for Fe_1/Au_1 MLS, the change in the local environment and the increase of the number of Fe nearest neighbors around the Fe sites result in broadening of the d bands and a decrease of the calculated Fe spin magnetic moment to 2.79 μ_B . As opposed to the Fe_1/Au_1 MLS, where we observed strong anisotropy of the Fe d orbital moment, the Fe_2/Au_2 MLS exibits very small anisotropy of the orbital magnetic moment (Table 6 and Fig. 45). In Fig. 45 the functions $dm_l(E)$, $m_l(E)$, and $\Delta m_l(E)$ calculated for Fe and Au sites in Fe_2/Au_2 MLS are shown. Although all the three functions show strong energy dependence as in the case of Fe_1/Au_1 , negligible anisotropy of the Fe d orbital moment was observed at the Fermi energy. The explanation can be found in Fig. 46. In the case of Fe_2/Au_2 MLS there also are two peaks in the partial density of Fe d states below and above the Fermi level but in contrast to the Fe_1/Au_1 MLS they have the same $d_{x^2-y^2}$ character (Fig. 46) with a strong admixture of $d_{3z^2-r^2}$. Moreover, the partial weights of $d_{x^2-y^2}$ and $d_{3z^2-r^2}$ states at the Fermi level are such that $m_l(E_F)$ changes only slightly upon the changing of the magnetization direction from $\mathbf{M} \parallel (001)$ to $\mathbf{M} \perp (001)$, and the anisotropy of the Fe orbital moment $\Delta m_l(E_F)$ is very small (see insert in Fig. 45).

Table 6

Calculated spin M_S and orbital M_L magnetic moments (in μ_B) of Fe_2/Au_2 versus magnetization direction [95].

Atom	State	$\mathbf{M} \parallel$ [001]		$\mathbf{M} \perp$ [001]	
		M_S	M_L	M_S	M_L
Fe	s	−0.0045	0.0000	−0.0044	0.0000
	p	−0.0192	0.0001	−0.0191	−0.0005
	d	2.8056	0.0835	2.8064	0.0934
	f	0.0084	−0.0013	0.0084	−0.0015
	total	2.7902	0.0824	2.7912	0.0914
Au	s	−0.0260	0.0000	−0.0259	0.0000
	p	−0.0200	0.0026	−0.0200	0.0036
	d	0.0778	0.0155	0.0770	0.0182
	f	0.0059	−0.0009	0.0059	−0.0012
	total	0.0377	0.0172	0.0370	0.0206

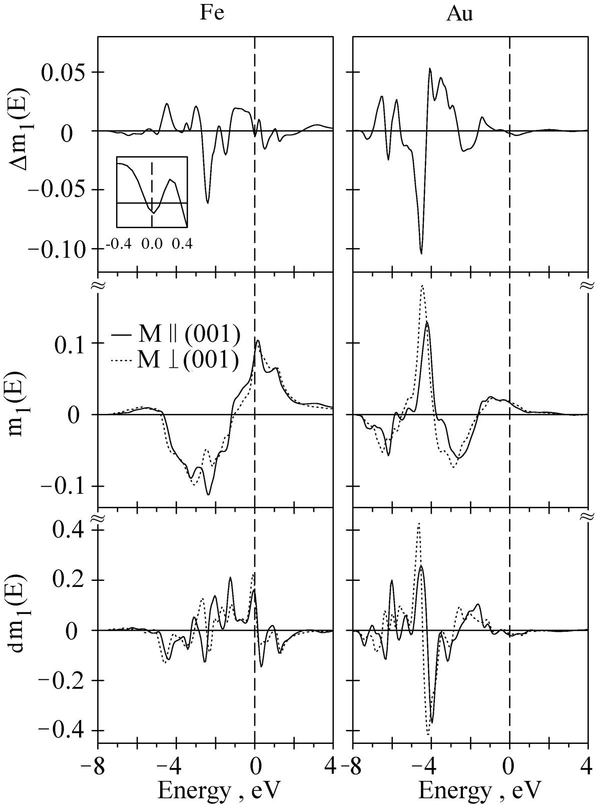

Fig. 45. The $dm_l(E)$ and $m_l(E)$ for two orientations of magnetization together with $\Delta m_l(E)$ for the Fe_2/Au_2 MLS [95].

The dependence of the MOA on the SO coupling and hybridization strengths is very complicated (see, e.g., Ref. 118) and does not allow one to introduce a simple model consideration as in the case of the MC anisotropy [89,90]. While the anisotropic band splitting can be directly related to the MCA, the situation with MOA is more complex, as the eigenvalues and wave functions of both the initial and final states enter the expression for the matrix elements. Therefore, the only way to obtain a realistic description of the MOA is to perform numerical calculations. The optical conductivity can be expressed as a sum of additive contributions coming from interband transitions with the initial and/or final states lying in different nonoverlapping energy intervals. In the case of Fe_1/Au_1 , the Fe $d_\uparrow$ and Fe $d_\downarrow$ states are well separated in energy but overlap with the Au d states in a wide energy interval (see Fig. 40). Even less distinct separation in the energy position of the initial Fe and Au d states is observed in the case of the Fe_2/Au_2 MLS (see Fig. 44). It seems to be more informative to examine the dependence of the MOA on the site-dependent optical transition matrix elements. The calculations have been performed in the way described in Ref. 119, where, within an atomic sphere about either one of the atomic positions, the optical transition matrix elements were set to zero. In this

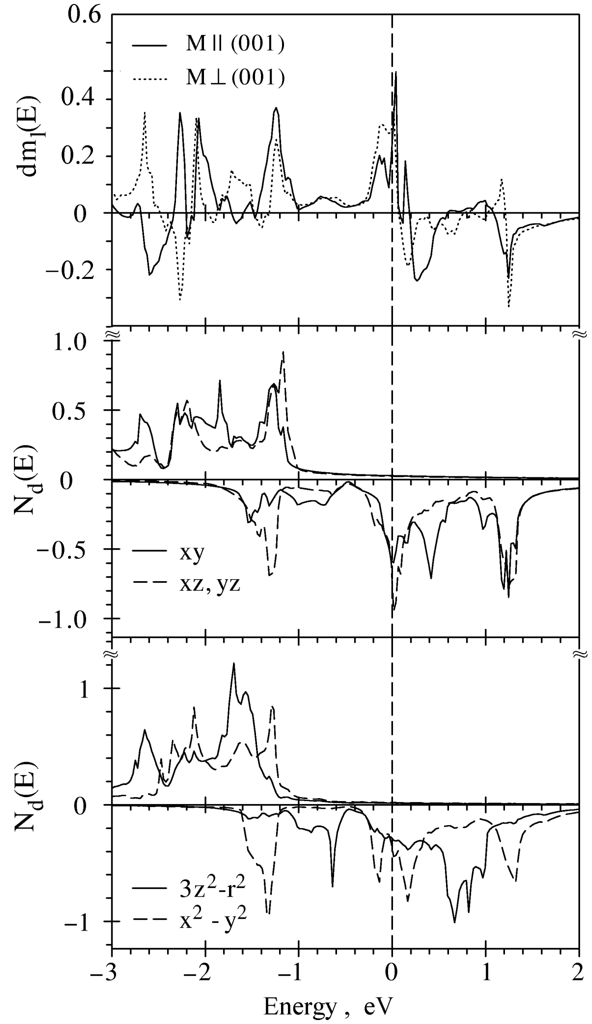

Fig. 46. The $dm_l(E)$ on Fe site for two orientations of magnetization and d-partial density of states (in state/(atom · eV · spin)) for the Fe_2/Au_2 MLS [95].

way, the optical conductivity spectra and MOA can be analyzed in terms of the contributions arising from the transitions on the particular sites. The decomposition of the MOA into the contributions from interband transitions on the Fe and Au sites in Fe_1/Au_1 MLS is shown in Fig. 47,*a*. As it can be seen, the magnitude of the MO anisotropy spectrum is determined by both the Au and Fe sites, depending on the spectral region. Only in the 0 to ~ 1 eV energy interval can the MOA be connected exclusively with the transition on the Fe site. The interband transitions on the Au site are mainly responsible for the MOA spectra in the ~ 1 to ~ 5 eV energy interval. The transitions occur between the Au $d_\downarrow$ states located at energies $E \leq 1$ eV below the Fermi level and the hybridized states of p and f characters lying in the energy range up to 2 eV above the Fermi level. The enhanced density of these final states arises due to the strong hybridization with Fe $d_\downarrow$ states in the energy interval. In particular, the peak at 3.7 eV in the MOA spectra is completely determined by these transitions. The peak at 5.3 eV is equally due to both the Fe and Au related transitions. The results of the analysis for Fe_2/Au_2 MLS is shown in Fig. 47,*b*. As in the case of Fe_1/Au_1 MLS, the transitions on both the Fe and Au sites determine the resulting MOA spectra in the Fe_2/Au_2 MLS; however, the main contribution arises from transitions on the Au site in the whole spectral range. We have verified that the prominent peak in the Fe_2/Au_2 MOA spectra at 5.5 eV is mostly determined by Au d related transitions to the final states extending up to ~ 4 eV above the Fermi level.

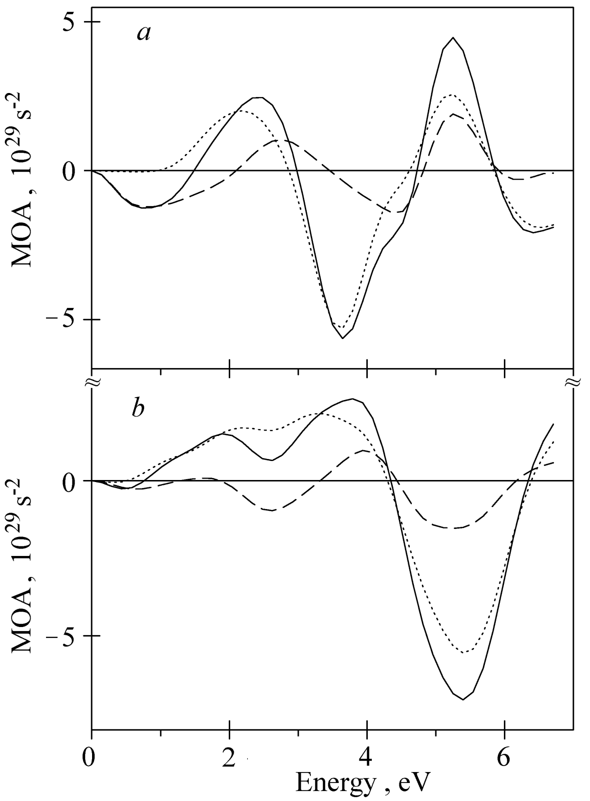

Fig. 47. Decomposition of the calculated MOA spectra (solid lines) into the contributions coming from all interband transitions on Fe (dashed lines) and Au (dotted lines) sites in Fe_1/Au_1 (*a*) and Fe_2/Au_2 (*b*) MLS [95].

Two major effects lead to the appearance of the MOA when the magnetization direction is changed: (i) the change of the band energies (Fig. 41) and (ii) the change of the orbital character of the wave functions. To determine which of the effects dominates we performed two model calculations. In the first one, the spectra were obtained using the as-calculated band energies, while the corresponding mo-

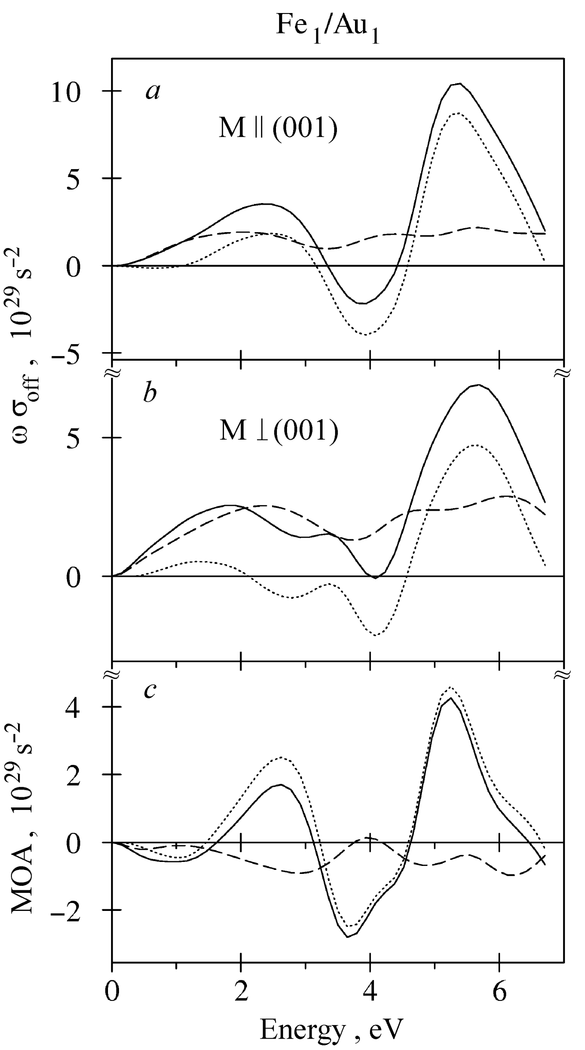

Fig. 48. Calculated absorptive off-diagonal part of the optical conductivity (*a*, *b*) and MO anisotropy (*c*) in the Fe$_1$/Au$_1$ MLS (solid lines) together with the results of the calculations for the SO coupling set to zero on Au site (dashed lines) and Fe site (dotted lines) [95].

mentum matrix elements at every **k** point were averaged over the magnetization directions. The calculated MOA is zero in this case, whereas the MOA obtained from the second calculation, in which — vice versa — the averaged band energies and as-calculated matrix elements were used, is in very good agreement with the results of the *ab initio* calculation. It clearly demonstrates that the main effect of MOA comes from the change of the orbital character of the wave functions due to rotation of the magnetization axis. This is exactly the origin of the anisotropy of the orbital moment also, as discussed before. Although the common origin of both anisotropies is the spin-orbit interaction, the relationship between the orbital moment anisotropy and the MOA is not simple. While the orbital moment anisotropy is determined by the integral property of the occupied states (Eqs. (17)–(20)), the magneto-optical anisotropy is related to the energy-dependent quantity given by the convolution of all the initial occupied and final unoccupied states within the given energy difference (Eq. (9)).

The dependence of the MOA on the exchange splitting and the SO interaction was examined in the same way as in Refs. 74 and 119. It was found that the SO coupling of Au is equally responsible for the large MOA as the exchange splitting of Fe. If we set the SO coupling on Fe to zero, the off-diagonal optical conductivity is changed in the whole energy interval by a negative shift similar for both magnetization directions (Fig. 48,*a* and *b*). Thus the contribution of the SO coupling on the Fe site to the conductivity is significant but almost isotropic. As a result, the MO anisotropy is practically independent of the SO coupling strength on the Fe site (Fig. 48,*c*). On the other hand, putting the SO coupling on the Au site to zero affects strongly the off-diagonal optical conductivities, leading to a strong suppression of the MOA. As in the case of the Fe$_1$/Au$_1$ MLS, setting the SO coupling on Fe to zero in the Fe$_2$/Au$_2$ MLS changes the MO anisotropy to a lesser extent than the off-diagonal optical conductivity (not shown). However, putting the SO coupling on the Au site to zero affects strongly both the off-diagonal optical conductivity and the MOA. Thus the SO coupling of Au is mainly responsible for the large MO anisotropy in the Fe/Au MLS.

7. Summary

The investigation of the optical and magneto-optical properties of Co/Pd, Co/Pt, Co/Cu, and Fe/Au multilayers both experimentally and theoretically from first principles has been reviewed.

A detailed comparative experimental and theoretical study of the electronic structure and the magneto-optical properties of Co/Pd multilayers shows that in these systems the MOKE is governed by the off-diagonal part of the optical conductivity tensor. *Ab initio* calculations performed for model Co/Pd MLS with sharp interfaces reproduced the main peculiarities of the experimental Co/Pd MOKE spectra only moderately well. The Co/Pd MLS with the interface microstructure modeled by ordered planar alloys of different compositions were examined. The MOKE spectra calculated from first principles for these MLS differ considerably from those obtained for the models with sharp interfaces. It is shown that the main peculiarities and the tendencies in the modification of the MLS spectra with the variation of the Co sublayer thickness are adequately reproduced when the alloying, even limited to one atomic plane, is taken into account. The MOKE spectra calculated for the model structures with ordered Co_1Pd_3 interfacial planes, reproduce the measured spectra best. The results obtained demonstrate that interface microstructure plays a crucial role in the formation of the MOKE spectra of the Co/Pd layered structures.

The Kerr rotation of Co/Pt MLS is governed mainly by the off-diagonal part of the conductivity tensor. The infrared part of the spectrum originates from the MO activity of the Co layers themselves and scales with the Co content. On the other hand, the peak in the UV region is due to the hybridization of strongly spin-polarized Co d states with spin–orbit-split Pt d states, and its magnitude depends weakly on the MLS composition. It has been demonstrated that the chemical and structural ordering is accompanied by substantial electronic structure changes and results in a drastic modification of the MOKE spectra. The *ab initio* description of the MOKE spectra for model Co/Pt multilayers performed under the assumption of a sharp, ideal interface is not adequate for the detailed explanation of the experimentally observed spectra. The modeding of the multilayers with alloyed interfaces clearly illustrates the crucial role of the interface structure on the magneto-optical spectra of the Co/Pt MLS. It is shown that the main peculiarities and the tendencies in the modification of the MLS spectra with the variation of the Co sublayer thickness are adequately reproduced when the alloying, limited to two atomic planes, is taken into account. Very good agreement between the calculated and measured MOKE spectra demonstrates the validity of the adopted model and approach.

It was shown that although the dominant contribution to the off-diagonal part of the optical conductivity tensor of the Co/Cu MLS comes from the interband transitions involving Co electronic states, the interband transitions from Cu d states in the Cu sublayers play an important role. The Cu states at the interface are spin-polarized due to hybridization with Co states. The feature observed at $\hbar\omega \sim 2.1$ eV in the spectra of the optical conductivity tensor component $\sigma_{xx}^{(1)}$ is related to the edge of interband transitions from Cu d states in the Cu sublayers and is responsible for the peak at 2.1 eV in the polar Kerr rotation spectra of the Co/Cu MLS. The *ab initio* calculations reproduce the main features of the Co/Cu MLS spectra and provide an explanation of their microscopic origin.

A large orientation dependence of the magneto-optical response was experimentally observed in the Fe_n/Au_n multilayer structures. It was found that the magnitude of the magneto-optical anisotropy is very sensitive to the actual atomic structure of the superlattice and decreases as the number of atomic layers of the same type increases. In the case of the Fe_1/Au_1 MLS the calculations describe the measured spectra well only after taking into account the real structure of the MLS, namely, the mixture of mono- and double-layer structures. It can be verified that limited substitutional disorder at the interfaces leads to a decrease of the MO anisotropy.

The orientation anisotropy of the d orbital moment calculated from first principles shows that as the Au d states are almost completely occupied, the spin and orbital moments at the Au site are small and depend weakly on the magnetization direction in the Fe_1/Au_1 . At the same time, the anisotropy of the Fe orbital moment, which is determined mainly by the Fe d states, is quite large. Two strong maxima in the Fe d partial density of states arise in the vicinity of the Fermi level of the Fe_1/Au_1 MLS, which are predominantly of d_{x2-y2} character below the Fermi level and of d_{3z2-r2} character just above the Fermi level. Such an orbital character of the partial density of states leads to strong anisotropy of the Fe d orbital moment in the Fe_1/Au_1 MLS. In the case of the Fe_2/Au_2 MLS there are two strong maxima in the Fe d partial density of states, both being of predominantly of d_{x2-y2} character. As a result, a change of the magnetization direction leads to an almost isotropic Fe d orbital moment in the Fe_2/Au_2 MLS.

The interplay of the strong SO interaction on the Au sites and the large exchange splitting on the Fe sites through Au d – Fe d hybridization is responsible for the large MOA and the anisotropy of the Fe d orbital moment. The main effect of the MO anisotropy arises from the changing of the orbital character of the wave functions due to the change of the magnetization direction.

The results obtained imply that the magneto-optical properties of multilayers with various compositions and structures can be quantitatively predicted from first principles band-structure calculations. Such a possibility is important for basic research as well as applications.

1. M. Faraday, *Phil. Trans. R. Soc.* **136**, 1 (1846).
2. J. Kerr, *Phil. Mag.* **3**, 321 (1877).
3. M. J. Freiser, *IEEE Trans. Mag.* **4**, 1 (1968).
4. C. D. Mee and E. D. Daniel, *Magnetic Recording*, McGraw-Hill, New York (1987); M. Mansuripur, *The Physical Principles of Magneto-Optical Recording*, University Press, Cambridge (1995).
5. K. H. J. Buschow, in: *Ferromagnetic Materials*, E. P. Wohlfarth and K. H. J. Buschow (eds.), North-Holland, Amsterdam (1988), Vol. 4, p. 588.
6. W. Reim and J. Schoenes, in: *Ferromagnetic Materials*, E. P. Wohlfarth and K. H. J. Buschow (eds.), North-Holland, Amsterdam (1990), Vol. 5, p.133.
7. J. Schoenes, in: *Materials Science and Technology, Electronic and Magnetic Properties of Metals and Ceramics*, K. H. J. Buschow (vol.ed.), R. W. Cahn, P. Haasen and E. J. Kramer (eds.), Verlag Chemie, Weinheim (1992), Vol. 3A, p. 147.
8. H. Ebert, *Rev. Prog. Phys.* **59**, 1665 (1996).
9. V. N. Antonov, A. N. Yaresko, A. Ya. Perlov, V. V. Nemoshkalenko, P. M. Oppeneer, H. Eschrig, *Low Temp. Physics* **25**, 527 (1999).
10. H. R. Hulme, *Proc. R. Soc.* **A135**, 237 (1932).
11. C. Kittel, *Phys. Rev.* **A83**, A208 (1951).
12. P. N. Argyres, *Phys. Rev.* **97**, 334 (1955).
13. B. R. Cooper, *Phys. Rev.* **A139**, A1504 (1965).
14. R. Kubo, *J. Phys. Soc. Jpn.* **12**, 570 (1957).
15. A. E. Kondorsky and A. V. Vediaev, *J. Appl. Phys.* **39**, 559 (1968).
16. C. S. Wang and J. Callaway, *Phys. Rev.* **B9**, 4897 (1974); M. Singh, C. S. Wang, and J. Callaway, *Phys. Rev.* **B11**, 287 (1975).
17. G. H. O. Daalderop, F. M. Mueller, R. C. Albers, and A. M. Boring, *J. Magn. Magn. Mat.* **74**, 211 (1988); H. Ebert, P. Strange, and B. L. Gyorffy, *J. Phys.* **49**, 31 (1988); Yu. Uspenskii and S. V. Halilov, *Sov. Phys. JETP* **68**, 588 (1989).
18. S. S. P. Parkin, N. More, and K. P. Roche, *Phys. Rev. Lett.* **64**, 2304 (1990).
19. M. N. Baibich, J. M. Broto, A. Fert, F. Nguyen Van Dau, F. Petroff, P. Etienne, G. Creuzet, A. Friederich, and J. Chazelas, *Phys. Rev. Lett.* **61**, 2472 (1988).
20. M. G. Samant, J. Stöhr, S. S. S. Parkin, G. A. Held, B. D. Hermsmeier, F. Herman, M. van Schilfgaarde, L.-C.Duda, D. C. Mancini, N. Wassdahl, R. Nakajima, *Phys. Rev. Lett.* **72**, 1112 (1994).
21. W. B. Zeper, F. J. A. M. Greidanus, P. F. Carcia, and C. R. Fincher, *J. Appl. Phys.* **65**, 4971 (1989).
22. D. Weller, W. Reim, K. Spörl, and H. Brändle, *J. Magn. Magn. Mater.* **93**, 183 (1991).
23. C.-J. Lin, G. L. Gorman, C. H. Lee, R. F. C. Farrow, E. E. Marinero, H. V. Do, H. Notarys, and C. J. Chien, *J. Magn. Magn. Mater.* **93**, 194 (1991).
24. K. Sato, H. Ikekame, Y. Tosaka, K. Tsuzukiyama, Y. Togami, and M. Fujisawa, *J. Magn. Magn. Mater.* **126**, 572 (1993).
25. S . Visnovsky, *Czech. J. Phys.* **B34**, 969 (1984).
26. G. Metzger, P. Pluvinage, and R. Torguet, *Ann. Phys. (Paris)* **10**, 5 (1965).
27. W. H. Kleiner, *Phys. Rev.* **142**, 318 (1966).
28. A. H. MacDonald and S. H. Vosko, *J. Phys. C: Solid State Phys.* **12**, 2977 (1979).
29. H. Ebert, H. Freyer, A. Vernes, and G.-Y. Guo, *Phys. Rev.* **B53**, 7721 (1996).
30. H. Ebert, *Phys. Rev.* **B38**, 9390 (1988).
31. I. V. Solovyev, A. B. Shik, V. P. Antropov, A. I. Liechtenstein, V. A. Gubanov, and O. K. Andersen, *Sov. Phys. Solid State*. **31**, 1285 (1989).
32. O. K. Andersen, *Phys. Rev.* **B12**, 3060 (1975).
33. V. V. Nemoshkalenko, A. E. Krasovskii, V. N. Antonov, Vl. N. Antonov, U. Fleck, H. Wonn, and P. Ziesche, *Phys. Status Solidi* **B120**, 283 (1983).
34. V. N. Antonov, A. Ya. Perlov, A. P. Shpak, and A. N. Yaresko, *J. Magn. Magn. Mater.* **146**, 205 (1995).
35. V. N. Antonov, A. I. Bagljuk, A. Ya. Perlov, V. V. Nemoshkalenko, Vl. N. Antonov, O. K. Andersen, and O. Jepsen, *Low Temp. Phys.* **19**, 494 (1993).
36. A. Santoni and F. J. Himpsel, *Phys. Rev.* **B43**, 1305 (1991).
37. U. von Barth and L. A. Hedin, *J. Phys.* **C5**, 1629 (1972).
38. V. V. Nemoshkalenko and V. N. Antonov, *Computational Methods in Solid State Physics*, Gordon and Breach, London (1998).
39. P. E. Blöchl, O. Jepsen, and O. K. Andersen, *Phys. Rev.* **B49**, 16223 (1994).
40. K. Sato, *Jpn. J. Appl. Phys.* **20**, 2403 (1981).
41. D. E. Aspnes and A. A. Studna, *Appl. Opt.* **14**, 220 (1975).
42. S. Uba, L. Uba, A. N. Yaresko, A. Ya. Perlov, V. N. Antonov, and R. Gontarz, *J. Phys.: Condens. Matter* **10**, 3769 (1998).
43. K. Sato, H. Ikekame, Y. Tosaka, and S.-C. Shin, *J. Magn. Magn. Mater.* **126**, 553 (1993).
44. S. Uba, L. Uba, and R. Gontarz, *IEEE Trans. Magn.* **30**, 806 (1994).
45. M. Nawate, T. Takeuchi, Y. Tamura, and S. Honda, *Proc. Int. Conf. on Magnetism (Warsaw, 1994)*, S. Krompiewski, A. Szajek, and J. Morkowski (eds.), Poznan, Osrodek Wydawnictw Naukowych (1994), p 517.
46. S. K. Kim, Y. M. Koo, V. A. Chernov, and H. Padmore, *Phys. Rev.* **B53**, 11114 (1996).
47. H. Giordano, A. Atrei, M. Torrini, U. Bardi, M. Gleeson, and C. Barnes, *Phys. Rev.* **B54**, 11762 (1996).
48. S. Uba, A. N. Yaresko, L. Uba, A. Ya. Perlov, V. N. Antonov, R. Gontarz, and H. Ebert, *Phys. Rev.* **B57**, 1534 (1998).
49. W. Reim, H. Brändle, D. Weller, and J. Schoenes, *J. Magn. Magn. Mater.* **93**, 220 (1991).
50. J. Vogel, A. Fontaine, V. Cros, F. Petroff, J.-P. Kappler, G. Krill, A. Rogalev, and J. Goulon, *Phys. Rev.* **B55**, 3663 (1997).
51. A. B. Shick, V. Drchal, J. Kurdnovský, and P. Weinberger, *Phys. Rev.* **B54**, 1610 (1996); H. Ebert, B. Drittler, and H. Akai, *J. Magn. Magn. Mater.* **104–107**, 733 (1992).
52. J. Banhart and H. Ebert, *Europhys. Lett.* **32**, 517 (1995).
53. H. Ebert, *Jpn. J. Appl. Phys.* **32**, Suppl. 32-2 (1993); H. Ebert and H. Akai, *Mat. Res. Soc. Symp. Proc.* **253**, 329 (1992).
54. R. M. Bozorth, P. A. Wolff, D. D. Davis, V. B. Compton, and J. H. Wernick, *Phys. Rev.* **122**, 1157 (1961).
55. L. D. Landau and E. M. Lifshitz, *Electrodynamics of Continuos Media*, Pergamon, New York (1960).
56. A. N. Yaresko, P. M. Oppeneer, A. Ya. Perlov, V. N. Antonov, T. Kraft, and H. Eschrig, *Europhys. Lett.* **36**, 551 (1996).
57. M. M. Kirillova, G. A. Bolotin, and L. V. Nomerovannaja, *Opt. Spectrosc.* **49**, 742 (1980).
58. Yu. A. Uspenskii, E. T. Kulatov, and S. V. Halilov, *Phys. Rev.* **B54**, 474 (1996); G. Y. Guo and H. Ebert, *Phys. Rev.* **B50**, 10377 (1994).

59. The MOKE spectrum of the Co film presently studied differs from the previously published [S. Uba, L. Uba, R. Gontarz, V. N. Antonov, A. Ya. Perlov, and A. N. Yaresko, *J. Magn. Magn. Mater.* **140–144**, 575 (1995)] due to the smaller film thickness of the later and known dependences of MOKE on the film microstructure, see, e.g., T. Suzuki, D. Weller, C.-A. Chang, R. Savoy, T. Huang, B. A. Gurney, and V. Speriosu, *Appl. Phys. Let.* **64**, 2736 (1994).
60. D. E. Aspnes, in: *Handbook of Optical Constants of Solids*, E. D. Palik (ed.), Academic, Orlando, FL (1985).
61. S. Logothetidis, S. Boultadakis, N. K. Flevaris, and D. Fuchs, *J. Magn. Magn. Mater.* **93**, 444 (1991).
62. H. Brändle, D. Weller, J. C. Scott, S. S. P. Parkin, and C.-J. Lin, *IEEE Trans. Magn. MAG-28*, 2967 (1992).
63. K. Sato, H. Hongu, H. Ikekame, J. Watanabe, K. Tsuzukiyama, Y. Togami, M. Fujisawa, and T. Fukazawa, *Jpn. J. Appl. Phys.* **31**, 3603 (1992).
64. S. Visnovsky, M. Nyvlt, V. Parizek, P. Kielar, V. Prosser, and R. Krishnan, *IEEE Trans. Magn. MAG-29*, 3390 (1993).
65. V. N. Antonov, A. Ya. Perlov, A. P. Shpak, and A. N. Yaresko, *J. Magn. Magn. Mater.* **146**, 205 (1995).
66. P. M. Oppeneer, T. Kraft, and H. Eschrig, *Phys. Rev.* **B52**, 3577 (1995).
67. G. Y. Guo, and H. Ebert, *Phys. Rev.* **B50**, 10377 (1994).
68. D. Weller, G. R. Harp, R. F. C. Farrow, A. Cebollada, and J. Sticht, *Phys. Rev. Lett.* **72**, 2097 (1994).
69. S. N. Rashkeev, Yu. A. Uspenskii, and I. I. Mazin, *Zh. Eksp. Teor. Fiz.* **88**, 1687 (1985).
70. G. Y. Guo, and H. Ebert, *Phys. Rev.* **B51**, 12633 (1995).
71. P. M. Oppeneer, V. N. Antonov, T. Kraft, H. Eschrig, A. N. Yaresko, and A. Ya. Perlov, *Solid State Commun.* **94**, 255 (1995).
72. D. Weller, J. Sticht, G. R. Harp, R. F. C. Farrow, R. F. Marks, and H. Brändle, *Mat. Res. Soc. Symp. Proc.* **313**, 501 (1993).
73. G. R. Harp, D. Weller, T. A. Rabedeau, R. F. C. Farrow, and M. F. Toney, *Phys. Rev. Lett.* **71**, 2493 (1993).
74. S. Uba, L. Uba, A. N. Yaresko, A. Ya. Perlov, V. N. Antonov, and R. Gontarz, *Phys. Rev.* **B53**, 6526 (1996).
75. L. Uba, S. Uba, A. N. Yaresko, A. Ya. Perlov, V. N. Antonov, and R. Gontarz, *J. Magn. Magn. Mater.* **193**, 159 (1999).
76. T. Katayama, Y. Suzuki, H. Awano, Y. Nishihara, and N. Koshizuka, *Phys. Rev. Lett.* **60**, 1426 (1988).
77. Y. B. Xu, Q. Y. Jin, Y. Zhai, M. Lu, Y. Z. Miao, Q. S. Bie, and H. R. Zhai, *J. Appl. Phys.* **74**, 3470 (1993).
78. M. Sakurai and T. Shinjo, *J. Appl. Phys.* **74**, 6840 (1993).
79. Y. B. Xu, Q. Y. Jin, Y. Zhai, Y. Z. Miao, M. Lu, and H. R. Zhai, *J. Magn. Magn. Mater.* **126**, 541 (1993).
80. Y. B. Xu, M. Lu, Q. S. Bie, Y. Zhai, Q. Y. Jin, X. B. Zhu, and H. R. Zhai, *J. Magn. Magn. Mater.* **140–144**, 581 (1995).
81. S. Visnovsky, M. Nyvlt, V. Prosser, J. Ferre, G. Penissard, D. Renard, and G. Sczigel, *J. Magn. Magn. Mater.* **128**, 179 (1993).
82. S. Uba, L. Uba, A. Ya. Perlov, A. N. Yaresko, V. N. Antonov, and R. Gontarz, *J. Phys.: Condens. Matter* **9**, 447 (1997).
83. R. Gontarz and T. Lucinski, *J. Magn. Magn. Mater.* **101**, 253 (1991).
84. Yu. A. Uspenskii and S. V. Khalilov, *Zh. Eksp. Teor. Fiz.* **95** 1022 (1989) [*Sov. Phys. JETP* **68**, 588 (1989)].
85. P. M. Oppeneer, T. Maurer, J. Sticht, and J. Kübler, *Phys. Rev.* **B45**, 10924 (1992).
86. P. M. Oppeneer, J. Sticht, T. Maurer, and J. Kübler, *Z. Phys.* **B88**, 309 (1992).
87. For a review on the field of magnetic multilayers, see *Ultrathin Magnetic Structures*, J. A. C. Bland and B. Heinrich (eds.), Springer-Verlag, Berlin (1994), Vols. I and II.
88. H. Brooks, *Phys. Rev.* **58**, 909 (1940); G. C. Fletcher, *Proc. Phys. Soc. (London)* **A67**, 505 (1954); N. Mori, *J. Phys. Soc. Jpn.* **27**, 307 (1969); E. I. Kondorskii and E. Staube, *Zh. Eksp. Teor. Fiz.* **63**, 356 (1972) [*Sov. Phys. JETP* **36**, 188 (1973)]; J. G. Gay and R. Richter, *Phys. Rev. Lett.* **56**, 2728 (1986); J. G. Gay and R. Richter, *J. Appl. Phys.* **61**, 3362 (1987).
89. P. Bruno, *Phys. Rev.* **B39**, 865 (1989).
90. G. van der Laan, *J. Phys.: Condens. Matter* **10**, 3239 (1998).
91. J. Trygg, B. Johansson, O. Eriksson, and J. M. Wills, *Phys. Rev. Lett.* **75**, 2871 (1995); S. V. Halilov, A. Ya. Perlov, P. M. Oppeneer, A. N. Yaresko, and V. N. Antonov, *Phys. Rev.* **B57**, 9557 (1998), and references therein.
92. P. M. Oppeneer and V. N. Antonov, in: *Spin-Orbit Influenced Spectroscopies of Magnetic Solids*, H. Ebert and G. Schütz (eds.), Springer, Berlin (1996), p. 29.
93. E. A. Ganshina, G. S. Krinchik, L. S. Mironova, and A. S. Tablin, *Zh. Eksp. Teor. Fiz.* **78**, 733 (1980).
94. R. M. Osgood III, K. T. Riggs, A. E. Johnson, J. E. Mattson, C. H. Sowers, and S. D. Bader, *Phys. Rev.* **B56**, 2627 (1997).
95. L. Uba, S. Uba, V. N. Antonov, A. N. Yaresko, T. Slezak and J. Korecki, *Phys. Rev.* **B62**, 13731 (2000).
96. N. Spiridis and J. Korecki, *Appl. Surf. Sci.* **141**, 313 (1999).
97. V. Blum, Ch. Rath, S. Müller, L. Hammer, K. Heinz, J. M. Garcia, J. E. Ortega, J. E. Prieto, O. S. Hernan, J. M. Gallego, A. L. Vazquez de Parga, and R. Miranda, *Phys. Rev.* **B59**, 15966 (1999).
98. K. Takanashi, S. Mitani, M. Sano, H. Fujimori, H. Nakajima, and A. Osawa, *Appl. Phys. Lett.* **67**, 1016 (1995); S. Mitani, K. Takanashi, H. Nakajima, K. Sato, R. Schreiber, P. Grünberg, and H. Fujimori, *J. Magn. Magn. Mater.* **156**, 7 (1996).
99. T. Slezak, W. Karas, M. Kubik, M. Mohsen, M. Przybylski, N. Spiridis, and J. Korecki, *Hyperfine Interact.* **C3**, 409 (1998); J. Korecki, M. Kubik, N. Spiridis, and T. Slezak, *Acta Phys. Pol.* **A97**, 129 (2000).
100. K. Takanashi, S. Mitani, H. Fujimori, M. Sato, and Y. Suzuki, *J. Magn. Magn. Mater.* **177–181**, 1199 (1998).
101. K. Sato, E. Takeda, M. Akita, M. Yamaguchi, K. Takanashi, S. Mitani, H. Fujimori, and Y. Suzuki, *J. Appl. Phys.* **86**, 4985 (1999).
102. Y. Suzuki, T. Katayama, S. Yoshida, K. Tanaka, and K. Sato, *Phys. Rev. Lett.* **68**, 3355 (1992); W. Geerts, Y. Suzuki, T. Katayama, K. Tanaka, K. Ando, and S. Yoshida, *Phys. Rev.* **B50**, 12581 (1994).
103. Y. Suzuki, T. Katayama, P. Bruno, S. Yuasa, and E. Tamura, *Phys. Rev. Lett.* **80**, 5200 (1998).
104. J. Zak, E. R. Moog, C. Liu, and S. D. Bader, *J. Magn. Magn. Mater.* **89**, 107 (1990); J. Zak, E. R. Moog, C. Liu, and S. D. Bader, *Phys. Rev.* **B43**, 6423 (1991).
105. K. Takanashi, S. Mitani, K. Himi, and H. Fujimori, *Appl. Phys. Lett.* **72**, 737 (1998).
106. L. Uba, S. Uba, V. N. Antonov, A. N. Yaresko, A. Ya. Perlov, T. Ślezak, and J. Korecki, *Solid State Commun.* **114**, 441 (2000).

107. K. A. Mills, R. F. Davis, S. D. Kevan, G. Thornton, and D. A. Shirley, *Phys. Rev.* **B22**, 581 (1980).

108. E. E. Krasovskii, A. N. Yaresko, and V. N. Antonov, *J. Electr. Spectros.* **68** 157 (1994).

109. V. I. Anisimov, J. Zaanen, and O. K. Andersen, *Phys. Rev.* **B44**, 943 (1991).

110. V. I. Anisimov, F. Aryasetiawan, and A. I. Liechtenstein, *J. Phys.: Condens. Matter* **9**, 767 (1997).

111. V. N. Antonov, A. N. Yaresko, A. Ya. Perlov, P. Thalmeier, P. Fulde, P. M. Oppeneer, and H. Eschrig, *Phys. Rev.* **B58**, 9752 (1998).

112. L. Uba, S. Uba, A. N. Yaresko, and V. N. Antonov, unpublished.

113. H. Okamoto, T. B. Massalski, L. J. Swartzendruber, and P. A. Beck, *Bull. Alloy Phase Diagrams* **5** (6) (1984).

114. C. J. Pastor, C. Limones, J. J. Hinarejos, J. M. Garcia, R. Miranda, J. Gomez-Goni, J. E. Ortega, and H. D. Abruna, *Surf. Sci.* **364**, L505 (1996).

115. D. Weller, J. Stöhr, R. Nakajima, A. Carl, M. G. Samant, C. Chappert, R. Megy, P. Beauvillain, P. Veillet, and G. A. Held, *Phys. Rev. Lett.* **75**, 3752 (1995).

116. J. Stöhr and H. König, *Phys. Rev. Lett.* **75**, 3748 (1995).

117. J. H. van Vleck, *Electric and Magnetic Susceptibilities*, Oxford University Press, Oxford (1932).

118. H. S. Bennet and E. A. Stern, *Phys. Rev.* **137**, A448 (1965).

119. P. M. Oppeneer, V. N. Antonov, T. Kraf, H. Eschrig, A. N. Yaresko, and A. Ya. Perlov, *J. Phys. Condens. Matter* **8**, 5769 (1996).